

**Effects of Peptide Sequence in Controlling the Assembly Propensity and Structural
Morphology of Helical Gold Nanoparticle Superstructures**

by

Sydney Christine Brooks

B.S. Chemistry, West Virginia University, 2018

Submitted to the Graduate Faculty of the

Dietrich School of Arts and Sciences

of the requirements for the degree of

Doctor of Philosophy

University of Pittsburgh

2023

UNIVERSITY OF PITTSBURGH

DIETRICH SCHOOL OF ARTS AND SCIENCES

This dissertation was presented

by

Sydney Christine Brooks

It was defended on

March 2, 2023

and approved by

Committee Member: Ipsita Banerjee, Ph.D., Department of Chemical and Petroleum Engineering
and Department of Bioengineering

Committee Member: Jennifer Laaser, Ph.D., Department of Chemistry

Committee Member: Jill E. Millstone, Ph.D., Department of Chemistry

Dissertation Director: Nathaniel L. Rosi, Ph.D., Department of Chemistry and Department of
Chemical and Petroleum Engineering

Copyright © by Sydney Christine Brooks

2023

Effects of Peptide Sequence in Controlling the Assembly Propensity and Structural Morphology of Helical Gold Nanoparticle Superstructures

Sydney Christine Brooks, Ph.D.

University of Pittsburgh, 2023

Peptide-based materials incorporate the hierarchical structure of proteins: amino acids on the molecular scale dictate the secondary structure, which in turn affects the overall protein folding and function. Similarly, peptides and proteins can promote the growth of inorganic minerals with extreme precision, creating the composite substances that make up skeletons, shells, and other hard biological materials. The ability to synthetically harness this capability and use it to make equally precise materials in a laboratory could lead to the synthesis of new materials with applications in optics, sensing, and nanotechnology. By studying biomineralization, scientists have learned some of the design rules to synthesizing functional hybrid nanomaterials.

The Rosi group has spent over a decade developing a peptide-based assembly system for inorganic nanoparticles (NPs). Starting with a peptide amphiphile designed to bind gold

nanoparticles (Au NP) and assemble into fibers, we have developed a suite of design rules to synthesize a variety of nanostructures as well as dictate their structural morphology and function.

This dissertation describes several research projects aimed at understanding the effect of molecular changes to the peptide conjugate within an Au NP assembly system and leveraging them as tunable handles that we can use to control structural parameters of the resultant Au NP superstructures. In Chapter 1, a general discussion of peptide amphiphiles and peptide biomineralization is followed by an introduction of the group's work on nanoparticle assembly. In Chapter 2, the assembly module (organic tail and peptide N-terminal amino acids) of the peptide conjugate was examined, and a method to tune fiber and Au NP assembly propensity by increasing the β -sheet contribution of the peptide sequence was developed. In Chapter 3, the role of the particle binding module (C-terminal amino acids) in superstructural differentiation is investigated. By introducing a series of modifications with decreasing Au-binding affinity, it was determined that Au NP-peptide contact dictated the structure from aggregates (high) to single helices (moderate) to discrete Au NPs (low). Finally, I investigated the effect of electrostatic contributions to the particle binding module, and explore cooperative peptide conjugate assembly by leveraging attractive interactions in Chapter 4.

Table of Contents

Preface.....	xxix
1.0 Introduction.....	1
1.1 Nanoparticle Assembly	1
1.2 Programming Peptide Assembly	3
1.3 Peptide-Directed Biomineralization of Inorganic Materials	7
1.4 Peptide-Based Assembly of Gold Nanoparticles.....	9
1.4.1 Molecular Chirality Informs Nanoscale Chirality	12
1.4.2 Nanoscale Architecture Transformation from Double to Single Helices.....	14
1.4.3 Controlling Single Helix Morphology and Assembly by Modifying Length of Aliphatic Tail	19
1.5 Key Gaps in Knowledge and Objectives of this Dissertation	22
2.0 Leveraging Peptide Sequence Modifications to Promote Assembly of Chiral Helical Gold Nanoparticle Superstructures	25
2.1 Introduction	26
2.2 Results and Discussion	28

2.3 Conclusions	37
2.4 Experimental Methods.....	37
2.4.1 General Methods and Materials	37
2.4.2 Synthesis.....	38
2.4.2.1 Peptide Synthesis	38
2.4.2.2 Peptide Conjugate Synthesis.....	39
2.4.3 Assembly Conditions.....	40
2.4.3.1 Peptide Conjugate Assembly	40
2.4.3.2 Au NP Single Helices Assembly	40
2.4.3.3 Au NP Double Helices Assembly	40
2.4.4 Characterization and Sample Preparation.....	41
2.4.4.1 Circular Dichroism Spectroscopy	41
2.4.4.2 Attenuated Total Reflectance Fourier Transform Infrared Spectroscopy.....	41
2.4.4.3 Atomic Force Microscopy	41
2.4.4.4 Transmission Electron Microscopy.....	42

3.0 Single Amino Acid Modifications for Controlling the Helicity of Peptide-Based Chiral Gold Nanoparticle Superstructures	43
3.1 Introduction	44
3.2 Results and Discussion	47
3.3 Conclusions	57
3.4 Experimental Methods.....	57
3.4.1 General Methods and Materials	57
3.4.2 Synthesis.....	58
3.4.2.1 Peptide Synthesis	58
3.4.2.2 Peptide Conjugate Synthesis.....	59
3.4.3 Assembly Protocols	60
3.4.3.1 Peptide Conjugate Assembly	60
3.4.3.2 NP Superstructure Assembly.....	60
3.4.4 Characterization and Sample Preparation.....	61
3.4.4.1 Atomic Force Microscopy (AFM)	61
3.4.4.2 Circular Dichroism (CD) Spectroscopy.....	61

3.4.4.3 Attenuated Total Reflectance Fourier Transform Infrared Spectroscopy (ATR-FTIR).....	61
3.4.4.4 Transmission Electron Microscopy (TEM).....	62
3.4.5 Molecular Simulations.....	62
3.4.5.1 Replica Exchange with Solute Tempering Molecular Dynamics (REST-MD) Simulations.....	62
3.4.5.2 Clustering Analysis.....	63
3.4.5.3 Residue contact analysis.....	64
3.4.5.4 Steered MD and umbrella sampling calculations.....	64
4.0 Cooperative Assembly of Nanoparticle Superstructures through Designed Electrostatic Interactions	66
4.1 Introduction	67
4.2 Results and Discussion	69
4.3 Conclusion.....	78
4.4 Experimental Methods.....	79
4.4.1 General Methods and Materials	79
4.4.2 Synthesis.....	79

4.4.2.1 Peptide Synthesis	79
4.4.2.2 Peptide Conjugate Synthesis.....	81
4.4.3 Assembly Conditions.....	81
4.4.3.1 Peptide Conjugate Assembly	81
4.4.3.2 Nanoparticle Superstructure Assembly.....	81
4.4.4 Characterization and Sample Preparation.....	82
4.4.4.1 Circular Dichroism (CD) Spectroscopy.....	82
4.4.4.2 Fluorescence Plate Reader	82
4.4.4.3 Atomic Force Microscopy (AFM)	82
4.4.4.4 Transmission Electron Microscopy (TEM).....	83
5.0 Broader Implications and Future Directions	84
Appendix A Supporting Information for Chapter 2: “Leveraging Peptide Sequence Modifications to Promote Assembly of Chiral Helical Gold Nanoparticle Superstructures”	87
Appendix B Supporting Information for Chapter 3: “Single Amino Acid Modifications for Controlling the Helicity of Peptide-Based Chiral Gold Nanoparticle Superstructures”	100

Appendix B.1 Peptide Conjugate Synthesis and Characterization.....	101
Appendix B.2 Peptide Conjugate Assembly Studies	103
Appendix B.3 Synthesis of Amine-Terminated Peptide Variants and NP Synthesis Studies.....	106
Appendix B.4 Nanoparticle Assembly Studies.....	108
Appendix B.5 Representative Structures of Peptide Variants on Au(111) Surface ...	112
Appendix B.6 9T Peptide Conjugate Synthesis and NP Assembly Studies.....	116
Appendix B.7 Computational Methodology and Supporting Data.....	119
Appendix B.7.1 General Simulation Set-up.....	119
Appendix B.7.2 Replica Exchange with Solute Tempering MD simulations	120
Appendix B.7.3 Clustering Analysis.....	120
Appendix B.7.4 Residue contact analysis.....	121
Appendix B.7.5 Steered MD and umbrella sampling calculations	123
Appendix C Supporting Information for Chapter 4: “Cooperative Assembly of Nanoparticle Superstructures through Designed Electrostatic Interactions”	129
Appendix C.1 Peptide and Peptide Conjugate Synthesis.....	130
Appendix C.2 Single Component Fiber and Nanoparticle Assembly Studies	133

Appendix C.3 Multi-Component Fiber and Au NP Assembly Studies.....	137
References	140

List of Tables

Appendix Table 1. Particle length and width of Au NPs synthesized by amine-terminated peptide variants.....	107
Appendix Table 2. Reference sites and cut-off values for each residue used to determine residue-surface contact.....	122
Appendix Table 3. Amino acid binding free energies in kJ mol^{-1} (as reported in Palafox-Hernandez <i>et al.</i>, <i>Chem. Mater.</i> 2014, 26, 4960-4969). Values for CtBu, M^{ox} and $\text{C}^{\text{ox}}\text{tBu}$ were obtained in current work.....	124
Appendix Table 4. Residue surface contact (“Contact”) expressed as a fraction between 0 and 1, and residue binding score (“Bind Sc.”, kJ mol^{-1}) defined as the contact fraction multiplied by the residue binding free energy (Table S3), for the C, M and CtBu peptide variants. Blue highlighting indicates the 9th residue.....	125
Appendix Table 5. Residue surface contact (“Contact”) expressed as a fraction between 0 and 1, and residue binding score (“Bind Sc.”, kJ mol^{-1}) defined as the contact fraction multiplied by the residue binding free energy (Table S3), for M^{ox}, S, and T peptide variants. Blue highlighting indicates the 9th residue.....	126
Appendix Table 6. Residue surface contact (“Contact”) expressed as a fraction between 0 and 1, and residue binding score (“Bind Sc.”, kJ mol^{-1}) defined as the contact	

fraction multiplied by the residue binding free energy (Table S3), for A and C^{ox}tBu peptide variants. Blue highlighting indicates the 9th residue. 127

Appendix Table 7. Particle dimensions for Au NPs synthesized from 37.5 nM and 75 nM peptide conjugates..... 137

Appendix Table 8. Particle Dimensions for mixed Au NP assemblies. 139

List of Figures

- Figure 1-1. Chiral biomolecules can be used to assembly achiral NPs into superstructures, and the molecular level chirality can dictate the nanoscale chiral properties. Adapted permission from ref. ¹² Copyright 2017 Wiley..... 2**
- Figure 1-2. Hierarchical assembly of proteins. Reprinted with permission from ref.¹⁴ Copyright 2021 American Chemical Society..... 3**
- Figure 1-3. Peptide secondary structures (a) right-handed α -helix, (b) left-handed PPII, and (c) three β -strands forming a β -sheet. Reprinted with permission from ref.¹⁵ Copyright 2017 Springer Nature..... 4**
- Figure 1-4. Summary of phage display methodology for identifying metal-binding peptides. Reprinted with permission from ref.²¹ Copyright 2017 American Chemical Society. 7**
- Figure 1-5. Calculated absorption free energies at aqueous Ag and Au interfaces for the twenty naturally occurring amino acids. Reprinted with permission from ref.²⁸ Copyright 2014 American Chemical Society..... 8**
- Figure 1-6. The first peptide conjugate designed by the Rosi lab consisted of an hydrophobic organic tail attached to the gold-binding peptide PEP_{Au}..... 10**
- Figure 1-7. C₁₂-PEP_{Au} assembly and double-helical Au NP superstructures.³⁶ 10**

Figure 1-8. Mirror-image double helical Au NP assemblies; the handedness of the helices is controlled by the chirality of the constituent amino acids.⁴⁹ 13

Figure 1-9. Design of ‘multivalent’ conjugates..... 15

Figure 1-10. Oxidation of the peptide methionine residues to methionine sulfoxide caused a structural transformation from Au NP double helices to single helices. 16

Figure 1-11. Assembly of the single helix system showing (a) parallel β -strand alignment with two different inter-strand spacing, (b) component modules and (c) how they assemble into a Au NP scaffold..... 18

Figure 1-12. Aliphatic tail length of divalent conjugates controlled helical pitch length, Au NP size, and chiroptical signal.⁵⁷ 20

Figure 1-13. Discrete Au NPs produced in the presence of $C_{14}-(PEP_{Au}^{M-ox})_2$ 21

Figure 2-1. Peptide conjugate design and β -sheet modification strategy for $C_{14}-(PEP_{Au}^{M-ox})_2$. (a) The peptide conjugates contain a C_{14} aliphatic tail attached to the N-terminus of the peptide, which has a β -sheet-forming region and an inorganic particle binding region (PPII section). (b) The fourth amino acid in the sequence will be replaced with increasingly hydrophobic amino acids, which are expected to increase the assembly propensity of the peptide conjugate and thereby promote the assembly of Au NP superstructures. 30

Figure 2-2. Negatively-stained TEM images of (a) C_{14} -(PEP_{Au}^{M-ox})₂^T and (b) C_{14} -(PEP_{Au}^{M-ox})₂^F assemblies. (c) CD and (d) FTIR spectra of C_{14} -(PEP_{Au}^{M-ox})₂^X assemblies. (e) Low and (f) high magnification AFM images of C_{14} -(PEP_{Au}^{M-ox})₂^F fibers..... 31

Figure 2-3. Au NP assemblies formed using backbone modified peptide conjugates: (a) C_{14} -(PEP_{Au}^{M-ox})₂^T results in discrete unassembled Au NPs; (b,c) C_{14} -(PEP_{Au}^{M-ox})₂^F directs the assembly of Au NP single helices. (d) Helical pitch distribution of single helices derived from C_{14} -(PEP_{Au}^{M-ox})₂^F..... 32

Figure 2-4. Particle dimensions of Au NPs in single helices prepared using C_{14} -(AYSFGAPPM^{ox}PPF)₂.\ 33

Figure 2-5. CD spectrum of single helices prepared using C_{14} -(AYSFGAPPM^{ox}PPF)₂ showing the plasmonic chiroptical signal at ~565 nm. 33

Figure 2-6. (a) Negatively-stained TEM image of C_{10} -PEP_{Au}^F fibers. (b) FT-IR and (c) CD spectroscopy of C_{10} -PEP_{Au}^X assemblies. (d) AFM of C_{10} -PEP_{Au}^F fibers. (e) TEM image of Au NP superstructure assembly formed using C_{10} -PEP_{Au}^F and (f) helical pitch distribution of C_{10} -PEP_{Au}^F-based superstructures..... 36

Figure 3-1. (a) Illustration of the different ‘modules’ within the peptide conjugate: the assembly module contains the hydrophobic tail and β-strands at the peptide N-terminus; the C-terminus is the NP binding module and adopts PPII secondary structure. (b) Peptide conjugates can assemble into 1-D helical fibers with the NP

binding module exposed to the aqueous environment and the assembly module sequestered in the interior of the fiber..... 45

Figure 3-2. Structures formed from high surface contact peptide sequences form double-helical superstructures (top left), while low surface contact sequences yield Au NP single helices (top right). Scale bars 100 nm. Schematic illustration of proposed NP transformation with decreasing peptide-Au surface contact (bottom)..... 48

Figure 3-3. Family of amino acid modifications at the peptide 9th position, organized left to right from highest to lowest Au affinity..... 49

Figure 3-4. (a) Au NP aggregates produced using C₁₆-(AYSSGAPPCPPF)₂; (b) Double-helical superstructures produced using C₁₆-(AYSSGAPPMPPF)₂; (c) C₁₆-(AYSSGAPPCtBuPPF)₂ yields a blend of single- and double-helical assemblies; single helices produced using (d) C₁₆-(AYSSGAPPM^{ox}PPF)₂, (e) C₁₆-(AYSSGAPPSPPF)₂, and (f) C₁₆-(AYSSGAPPAPPF)₂; (g) Discrete Au NPs formed using C₁₆-(AYSSGAPPC^{ox}tBuPPF)₂. Scale bars 50 nm. (h) Table of NP dimensions and helix pitch (where applicable). (i) CD spectra for the three categories of superstructures: aggregated NPs, double helices, and single helices free energy data, along with the resultant binding scores, are provided in the Supporting Information (Tables S3-S6)..... 52

Figure 3-5. Binding scores for the original PEP_{Au} sequence (residue M at position 9) and the six sequence variants. (a) Sum of residue-surface binding scores for the N-terminal half (residues 1-6) and C-terminal half (residues 7-12). (b) Residue-surface

binding score for the residue at the ninth position in the sequence. Representative structures of (c) 9C and (d) 9C^{ox}tBu peptides adsorbed on Au(111) surface according to REST-MD simulations, corresponding to highest and lowest binding scores, respectively. C and C^{ox}tBu are highlighted with color: C, dark grey; H, light grey; N, blue; O, dark red; S, orange..... 54

Figure 3-6. Single helices produced using C₁₆-(AYSSGAPPTPPF)₂..... 56

Figure 4-1. Introducing multiple components increases potential structures and functions. 68

Figure 4-2. (a) Amino acid sequence and proposed assembly model of C₁₈-(PEP_{Au}^{E,9})₂. (b) AFM of fibers and (c) discrete/aggregated Au NPs produced with C₁₈-(PEP_{Au}^{E,9})₂. 72

Figure 4-3. Inducing cooperative assembly by mixing precisely designed conjugates. 73

Figure 4-4. Single-component assembly data for peptide conjugate series. (a) Illustration of PPII regions of each conjugate with electrostatics highlighted. (b) Fluorescence kinetics spectra from 0-14 hours and (c) CD spectra of single-component soft assemblies, confirming low fiber concentration from C₁₈-(PEP_{Au}^{E,9})₂ and C₁₈-(PEP_{Au}^{K,9})₂ and high concentration from C₁₈-(PEP_{Au}^{G,9})₂ and C₁₈-(PEP_{Au}^{N,9})₂. 75

Figure 4-5. Assemblies produced by mixed conjugates. (a) Illustration of electrostatic interactions in each combination. Spectroscopic visualization of co-assembly secondary structures using (b) fluorescence kinetic spectra and (c) CD spectra. AFM images of fibers formed from (d) 9G+9E, (f) 9N+9E, and (f) 9K+9E. Au NP single

helices produced by (g) 9G+9E and (h) 9N+9E. (i) Linear superstructures produced from 9K+9E..... 77

Appendix Figure 1. (a) Representative molecular structure of $N_3\text{-PEP}_{\text{Au}}^{\text{Mox,X}}$. LC-MS mass assignment of (b) $N_3\text{-(AYSTGAPPM}^{\text{ox}}\text{PPF)}$, $m/z = 1375 \text{ Da (M-H}^+)$; $710 \text{ Da (M-2H}^++ \text{HCOO}^-)/2$; $687 \text{ Da (M-2H}^+)/2$; and (c) $N_3\text{-(AYSFGAPPM}^{\text{ox}}\text{PPF)}$, $m/z = 1421 \text{ Da (M-H}^+)$; $710 \text{ Da (M-2H}^+)/2$ 88

Appendix Figure 2. (a) Representative molecular structure of $C_{14}\text{-(PEP}_{\text{Au}}^{\text{Mox,X}})_2$. LC-MS mass assignment of (b) $C_{14}\text{-(AYSTGAPPM}^{\text{ox}}\text{PPF)}_2$, $m/z = 1044 \text{ Da (M-3H}^+)/3$; $784 \text{ Da (M-4H}^+)/4$; and (c) $C_{14}\text{-(AYSFGAPPM}^{\text{ox}}\text{PPF)}_2$, $m/z = 1613 \text{ Da (M-2H}^+)/2$; $1075 \text{ Da (M-3H}^+)/3$; $807 \text{ Da (M-4H}^+)/4$ 89

Appendix Figure 3. Negatively-stained TEM image of $C_{14}\text{-(AYSSGAPPM}^{\text{ox}}\text{PPF)}_2$ after assembly experiment in 0.1 M HEPES. Fiber assemblies are not observed..... 90

Appendix Figure 4. Additional AFM images of (a, b) $C_{14}\text{-(AYSFGAPPM}^{\text{ox}}\text{PPF)}_2$, with labeled segments corresponding to (c, d) height traces. 91

Appendix Figure 5. AFM measurements of $C_{14}\text{-(AYSFGAPPM}^{\text{ox}}\text{PPF)}_2$. (a) Ribbon pitch distribution and (b) ribbon width distribution. 92

Appendix Figure 6. TEM image of discrete Au NPs synthesized using $C_{14}\text{-(AYSSGAPPM}^{\text{ox}}\text{PPF)}_2$ 92

Appendix Figure 7. Additional TEM images of single helices prepared using C₁₄-(AYSFGAPPM^{ox}PPF)₂. 93

Appendix Figure 10. (a) Representative molecular structure of NH₂-PEP_{Au}^X. LC-MS mass assignment of (a) NH₂-AYSSGAPPMPPF, m/z = 1220 Da (M-H⁺); 633 Da (M-H⁺+ HCOO⁻)/2; 609 Da (M-2H⁺)/2; (b) NH₂-AYSTGAPPMPPF, m/z = 1234 Da (M-H⁺); 641 Da (M-H⁺+ HCOO⁻)/2; 617 Da (M-2H⁺)/2; and (c) NH₂-AYSFGAPPMPPF, m/z = 1280 Da (M-H⁺); 663 Da (M-H⁺+ HCOO⁻)/2; 639 Da (M-2H⁺)/2..... 94

Appendix Figure 11. (a) Representative molecular structure of C₁₀-PEP_{Au}^X. LC-MS mass assignment of (b) C₁₀-AYSSGAPPMPPF, m/z = 1374 Da (M-H⁺); 711 Da (M-H⁺+ HCOO⁻)/2; 687 Da (M-2H⁺)/2; (c) C₁₀-AYSTGAPPMPPF, m/z = 1388 Da (M-H⁺); 717 Da (M-H⁺+ HCOO⁻)/2; 693 Da (M-2H⁺)/2; and (d) C₁₀-AYSFGAPPMPPF, m/z = 1434 Da (M-H⁺); 741 Da (M-H⁺+ HCOO⁻)/2; 717 Da (M-2H⁺)/2..... 95

Appendix Figure 12. Negatively-stained TEM image of (a) C₁₀-AYSSGAPPMPPF and (b) C₁₀-AYSTGAPPMPPF after assembly experiments in 0.1 M HEPES. Fiber assemblies are not observed. 96

Appendix Figure 13. Additional AFM image of C₁₀-AYSFGAPPMPPF fibers. Height trace does not indicate well-defined helicity..... 97

Appendix Figure 14. TEM images of discrete Au NPs/Au NP aggregates formed using (a) C₁₀-AYSSGAPPMPPF and (b) C₁₀-AYSTGAPPMPPF..... 98

Appendix Figure 15. (a-c) Additional TEM images of Au NP assemblies formed using C₁₀-AYSGAPPMPPF. High magnification images highlight the helical nature of the superstructures..... 98

Appendix Figure 16. Particle dimensions of Au NPs within double helices formed using C₁₀-AYSGAPPMPPF. 99

Appendix Figure 17. (a) Representative molecular structure of N₃-AYSSGAPPXPPF. LC-MS mass assignment of (b) N₃-AYSSGAPPCPPF, m/z = 1318 Da (M-H⁺); 682 Da (M-2H⁺+ HCOO⁻)/2; 658 Da (M-2H⁺)/2; (c) N₃-AYSSGAPPMPPF, m/z = 1347 Da (M-H⁺); 696 Da (M-2H⁺+ HCOO⁻)/2; 672 Da (M-2H⁺)/2; (d) N₃-AYSSGAPPCtBuPPF, m/z = 1374 Da (M-H⁺); 710 Da (M-2H⁺+ HCOO⁻)/2; 686 Da (M-2H⁺)/2; (e) N₃-AYSSGAPPM^{ox}PPF, m/z = 1363 Da (M-H⁺); 704 Da (M-2H⁺+ HCOO⁻)/2; 680 Da (M-2H⁺)/2; (f) N₃-AYSSGAPPSPPF, m/z = 1302 Da (M-H⁺); 674 Da (M-2H⁺+ HCOO⁻)/2; 650 Da (M-2H⁺)/2; (g) N₃-AYSSGAPPAPPF, m/z = 1286 Da (M-H⁺); 666 Da (M-2H⁺+ HCOO⁻)/2; 642 Da (M-2H⁺)/2; (h) N₃-AYSSGAPPC^{ox}tBuPPF, m/z = 1390 Da (M-H⁺); 718 Da (M-2H⁺+ HCOO⁻)/2; 694 Da (M-2H⁺)/2. 101

Appendix Figure 18. (a) Representative molecular structure of C₁₆-(AYSSGAPPXPPF)₂. LC-MS mass assignment of (b) C₁₆-(AYSSGAPPCPPF)₂, m/z 1520 Da (M-2H⁺)/2; (c) C₁₆-(AYSSGAPPMPPF)₂, m/z 1548 Da (M-2H⁺)/2; (d) C₁₆-(AYSSGAPPCtBuPPF)₂, m/z 1576 Da (M-2H⁺)/2; (e) C₁₆-(AYSSGAPPM^{ox}PPF)₂, m/z 1565 Da (M-2H⁺)/2; (f) C₁₆-(AYSSGAPPSPPF)₂, m/z 1504 Da (M-2H⁺)/2; (g)

C₁₆-(AYSSGAPPAPPF)₂, m/z 1488 Da (M-2H⁺)/2; (h) C₁₆-(AYSSGAPPC^{ox}tBuPPF)₂, m/z 1592 Da (M-2H⁺)/2..... 102

Appendix Figure 19. TEM images of peptide conjugate fibers assembled from (a) C₁₆-(AYSSGAPPCPPF)₂, (b) C₁₆-(AYSSGAPPMPPF)₂, (c) C₁₆-(AYSSGAPPCtBuPPF)₂, (d) C₁₆-(AYSSGAPPM^{ox}PPF)₂, (e) C₁₆-(AYSSGAPPSPPF)₂, (f) C₁₆-(AYSSGAPPAPPF)₂, and (g) C₁₆-(AYSSGAPPC^{ox}tBuPPF)₂. Scale bars 200 nm.. 104

Appendix Figure 20. ATR-FTIR spectra of peptide conjugate fibers showing (a) the full wavelength range and (b) expanded view of the amine region..... 104

Appendix Figure 21. CD spectra of the peptide conjugate fibers..... 105

Appendix Figure 22. (a) Representative molecular structure of NH₂-AYSSGAPPXPPF.

LC-MS mass assignment of (b) NH₂-AYSSGAPPCPPF, m/z = 1193 Da (M-H⁺); 619 Da (M-2H⁺+ HCOO⁻)/2; 596 Da (M-2H⁺)/2; (c) NH₂-AYSSGAPPMPPF, m/z = 1221 Da (M-H⁺); 633 Da (M-2H⁺+ HCOO⁻)/2; 610 Da (M-2H⁺)/2; (d) NH₂-AYSSGAPPCtBuPPF, m/z = 1249 Da (M-H⁺); 647 Da (M-2H⁺+ HCOO⁻)/2; 623 Da (M-2H⁺)/2; (e) NH₂-AYSSGAPPM^{ox}PPF, m/z = 1237 Da (M-H⁺); 641 Da (M-2H⁺+ HCOO⁻)/2; 618 Da (M-2H⁺)/2; (f) NH₂-AYSSGAPPSPPF, m/z = 1177 Da (M-H⁺); 611 Da (M-2H⁺+ HCOO⁻)/2; 588 Da (M-2H⁺)/2; (g) NH₂-AYSSGAPPAPPF, m/z = 1161 Da (M-H⁺); 603 Da (M-2H⁺+ HCOO⁻)/2; 580 Da (M-2H⁺)/2; (h) NH₂-AYSSGAPPC^{ox}tBuPPF, m/z = 1265 Da (M-H⁺); 655 Da (M-2H⁺+ HCOO⁻)/2; 632 Da (M-2H⁺)/2. 106

Appendix Figure 23. Au NPs produced from of NH₂-AYSSGAPPXPPF, where X = (a) C, (b) M, (c) CtBu, (d) M^{ox}, (e) S, (f) A, and (g) C^{ox}tBu. Scale bars are 50 nm. 107

Appendix Figure 24. Additional TEM images of Au NP assemblies produced by C₁₆-(AYSSGAPPCPPF)₂. 108

Appendix Figure 25. Additional TEM images of Au NP assemblies produced by C₁₆-(AYSSGAPPMPPF)₂. 108

Appendix Figure 26. Additional TEM images of Au NP assemblies produced by C₁₆-(AYSSGAPPCtBuPPF)₂. 109

Appendix Figure 27. Additional TEM images of Au NP assemblies produced by C₁₆-(AYSSGAPPM^{ox}PPF)₂. 109

Appendix Figure 28. Additional TEM images of Au NP assemblies produced by C₁₆-(AYSSGAPPSPPF)₂. 110

Appendix Figure 29. Additional TEM images of Au NP assemblies produced by C₁₆-(AYSSGAPPAPPF)₂. 110

Appendix Figure 30. Additional TEM images of Au NP assemblies produced by C₁₆-(AYSSGAPPC^{ox}tBuPPF)₂. 111

Appendix Figure 31. Representative structure of 9C peptide adsorbed on Au(111) surface according to REST-MD simulations (C, dark grey; H, light grey; N, blue; O, dark red; S, orange). 112

Appendix Figure 32. Representative structure of 9C^{ox}tBu peptide adsorbed on Au(111) surface according to REST-MD simulations (C, dark grey; H, light grey; N, blue; O, dark red; S, orange)..... 112

Appendix Figure 33. Representative structure of 9M peptide adsorbed on Au(111) surface according to REST-MD simulations (C, dark grey; H, light grey; N, blue; O, dark red; S, orange). In a), all atoms are colored, while in b) only the atoms of the 9th amino acid are colored for emphasis..... 113

Appendix Figure 34. Representative structure of 9CtBu peptide adsorbed on Au(111) surface according to REST-MD simulations (C, dark grey; H, light grey; N, blue; O, dark red; S, orange). In a), all atoms are colored, while in b) only the atoms of the 9th amino acid are colored for emphasis. 113

Appendix Figure 35. Representative structure of 9M^{ox} peptide adsorbed on Au(111) surface according to EST-MD simulations (C, dark grey; H, light grey; N, blue; O, dark red; S, orange). In a), all atoms are colored, while in b) only the atoms of the 9th amino acid are colored for emphasis..... 114

Appendix Figure 36. Representative structure of 9S peptide adsorbed on Au(111) surface according to REST-MD simulations(C, dark grey; H, light grey; N, blue; O, dark red). In a), all atoms are colored, while in b) only the atoms of the 9th amino acid are colored for emphasis. 114

Appendix Figure 37. Representative structure of 9T peptide adsorbed on Au(111) surface according to REST-MD simulations (C, dark grey; H, light grey; N, blue; O, dark red). In a), all atoms are colored, while in b) only the atoms of the 9th amino acid are colored for emphasis. 115

Appendix Figure 38. (a) Molecular structure and (b) LC-MS mass assignment of N₃-AYSSGAPPTPPF, m/z = 1316 Da (M-H⁺); 681 Da (M-2H⁺+ HCOO⁻)/2; 657 Da (M-2H⁺)/2. 116

Appendix Figure 39. (a) Molecular structure and (b) LC-MS mass assignment of C₁₆-(AYSSGAPPTPPF)₂, m/z 1518 Da (M-2H⁺)/2. 117

Appendix Figure 40. Additional TEM images of Au NP assemblies produced by C₁₆-(AYSSGAPPTPPF)₂. 118

Appendix Figure 41. Results from cross-cluster comparison of cluster centroid of the top 5 clusters of the original (“wild type”) peptide and those of the peptide variants. Light colored squares indicate conformational matches and the blue squares indicate near-matched structures. 128

Appendix Figure 42. Negatively stained TEM images of peptide conjugate fibers produced from (a,b) C₁₈-(AYSSGAPPEPPF)₂. 133

Appendix Figure 43. AFM images of peptide conjugate fibers produced from (a) C₁₈-(AYSSGAPPGPPF)₂, (b) C₁₈-(AYSSGAPPNPPF)₂, and (c) C₁₈-(AYSSGAPPKPPF)₂. 133

Appendix Figure 44. Negatively stained TEM images of peptide conjugate fibers produced from (a) C₁₈-(AYSSGAPPGPPF)₂, (b) C₁₈-(AYSSGAPPNPPF)₂, and(c) C₁₈-(AYSSGAPPKPPF)₂. 134

Appendix Figure 45. Additional TEM images of Au NP assemblies formed from 75 nM C₁₈-(AYSSGAPPGPPF)₂. 134

Appendix Figure 46. Additional TEM images of Au NP assemblies formed from 75 nM C₁₈-(AYSSGAPPNPPF)₂. 135

Appendix Figure 47. Additional TEM images of Au NP assemblies formed from 75 nM C₁₈-(AYSSGAPPKPPF)₂. 135

Appendix Figure 48. Additional TEM images of Au NP assemblies formed from 37.5 nM C₁₈-(AYSSGAPPEPPF)₂. 135

Appendix Figure 49. Additional TEM images of Au NP assemblies formed from 37.5 nM C₁₈-(AYSSGAPPGPPF)₂. 136

Appendix Figure 50. Additional TEM images of Au NP assemblies formed from 37.5 nM C₁₈-(AYSSGAPPNPPF)₂. 136

Appendix Figure 51. Additional TEM images of Au NP assemblies formed from 37.5 nM C₁₈-(AYSSGAPPKPPF)₂. 136

Appendix Figure 52. Additional TEM images of Au NP assemblies formed from 1:1 mixture of C₁₈-(AYSSGAPPEPPF)₂ and C₁₈-(AYSSGAPPGPPF)₂. 137

Appendix Figure 53. Additional TEM images of Au NP assemblies formed from 1:1 mixture of C₁₈-(AYSSGAPPEPPF)₂ and C₁₈-(AYSSGAPPNPPF)₂..... 138

Appendix Figure 54. Additional TEM images of Au NP assemblies formed from 1:1 mixture of C₁₈-(AYSSGAPPEPPF)₂ and C₁₈-(AYSSGAPPKPPF)₂..... 139

Preface

I'd like to start by thanking Prof. Nathaniel Rosi for his mentorship and guidance through my graduate career. A big part of the reason I was successful was I had an advisor who believed in me. I was extremely quiet as a first year, and he encouraged me to speak up and take my own ideas seriously. He probably regrets this now, and I hope he will enjoy some peace and quiet when I'm gone. I'm especially thankful he allowed me to spend time on teaching and outreach, without that freedom I wouldn't have found the career path that I am genuinely excited about.

I would also like to thank my dissertation committee, Prof. Jenny Laaser, Prof. Ipsita Banerjee, and Prof. Jill Millstone, for their challenging questions and valuable feedback. I'd like to thank my collaborators Prof. Tiffany Walsh and Ruitao Jin, whose contributions to my second project really elevated it to the next level.

I've been lucky to have worked with good people from start to finish. I really enjoyed working with all my former group members, and I'm thankful for their mentorship throughout. I'd like to thank Dr. Soumitra Mokashi Punekar for teaching me everything he knew; I would not be here without a strong foundation. I'd like to thank Dr. Yicheng Zhou for his friendship and mentorship. He was endlessly patient with me and I was lucky to have such a smart and hard-working role model in the lab. I'd also like to thank Mattheus De Souza for making the lab fun, and Dr. Zach Schulte for always keeping us out of chaos. In particular, I want to thank Dr. Prasenjit Das for persistently checking in on me when I needed it most.

I'd also like to thank the current group members: my favorite neighbor Yiwen He and my NP partner in crime Yuyu Zhang. Victoria Zerbach wins undergraduate of the year and I would not be graduating without her help. Zoe Soilis, Noah Garrett, Gefan He, Steven Yannucci, and Ryan Racioppo are all doing great work and I wish everyone the best of luck (but I don't think you need it). None of my work would be possible without the Department of Chemistry staff members, and I'd like to particularly thank Tom Harper, Joel Gillespie, and Mary Beth Conroy for graciously helping me out with pretty much everything at one point or another.

I couldn't have gotten by without a little help from my friends. First, Zoe Simon: while we never quite collaborated on research, we basically were together for everything else and I couldn't have picked a better person to go through the past five years with. Somehow all five of my best friends from college are/are going to be doctors, so Dr. Jaime Schussler, Dr. Kristyn Johnson, Dr. Brittany McWatters, and (soon to be) Dr. Emily Brezler, thank you all for being my home and the people who make me laugh the hardest. I'd also like to thank Akshay Kesari for always having my back.

Without the support of my mom, my sisters, my brother, and the rest of my family I wouldn't be at this point. Thank you for believing in me, especially when I did not believe in myself. Will, thank you for holding me together through hard times and still bringing me so much joy. I can't wait for the future.

This dissertation is dedicated to my dad. I'd like to think that somewhere you will read the title and maybe a line or two of the abstract, shake your head, and say that actually you don't need to read it to know it's great.

1.0 Introduction

1.1 Nanoparticle Assembly

Nanoparticles (NPs) are a topic of interest because they can exhibit vastly different properties than their bulk material. Not only do discrete NPs exhibit their own set of chemical and physical properties, but organizing discrete NPs can result in unique collective properties.^{1,2} For example, noble metal NPs can exhibit a plasmonic signal generated from the oscillation of delocalized electrons. However, when they are arranged into a chiral structure (*e.g.*, a helix) the collective oscillation across the assembly results in an intense chiroptical plasmonic signal.³ Additionally, modifications to the NP size, shape, or assembly structure can be used to tune these optical responses.⁴⁻⁶ Control over these properties could prove useful in many applications, from optics to sensing;^{7,8} however, accessing the level of control necessary is an ongoing challenge which requires a fundamental understanding of the connections between structure and properties/function.^{6,8,9}

Biology has the most intricate examples of self-assembly, with molecular interactions and bonding controlling the structure and function of the macromolecules that are the basis to life. Even the simplest biomolecules and assembly methods can be utilized in NP assembly: in a 2016 report from Zhou and coworkers, chiral assembly of cadmium telluride (CdTe) NPs was directed by enantiomers of cysteine,¹⁰ while a known amyloid-forming protein could template the chiral assembly of gold nanorods.¹¹ A significant amount of work has been done to understand and

manipulate the assembly mechanisms of these molecules in a biological context, and that knowledge can be applied and adapted to NP assembly to design biomolecule-based scaffolds for NP assembly. The same modifications that can turn a functional protein into an aggregated structure associated with neurodegenerative diseases could be used to turn discrete NPs into an organized helical assembly. The focus of this dissertation will be peptide-based assembly; in biological systems, this involves linking specific amino acids into a peptide chain, and the molecular structure of this peptide informs its self-assembly into secondary structures like β -sheets or α -helices that assemble into a functional protein.¹²

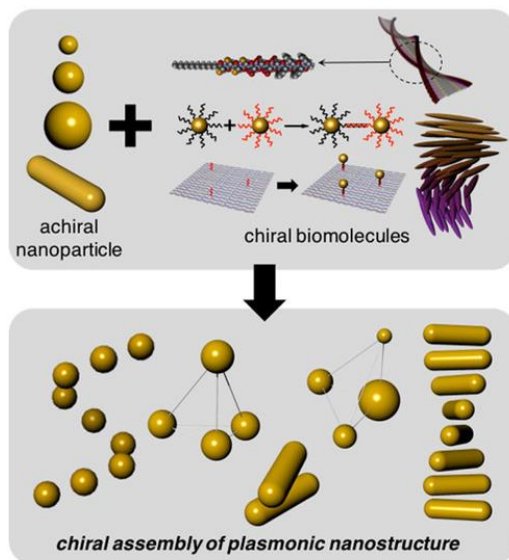


Figure 1-1. Chiral biomolecules can be used to assemble achiral NPs into superstructures, and the molecular level chirality can dictate the nanoscale chiral properties. Adapted with permission from ref. ¹³ Copyright 2017 Wiley.

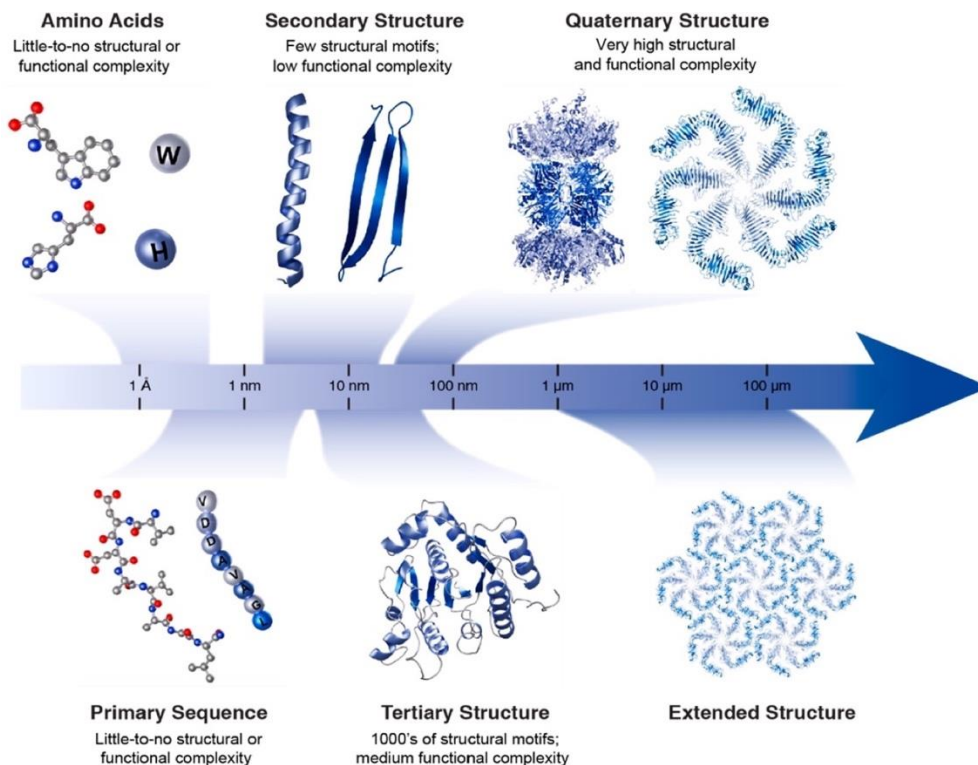


Figure 1-2. Hierarchical assembly of proteins. Reprinted with permission from ref.¹⁴ Copyright 2021 American Chemical Society.

1.2 Programming Peptide Assembly

By sequencing and studying known proteins, scientists can begin to understand and utilize this guidebook for precise structural assembly (Figure 1-2). The first level of assembly is the folding of peptide chains into the secondary structure: energetically favored arrangements that allow for maximum stabilization through hydrogen bonding and other intermolecular interactions. The most common secondary structure motifs are the α -helix and β -sheet, and in recent years the polyproline (PP) helices are included in this category.¹⁵

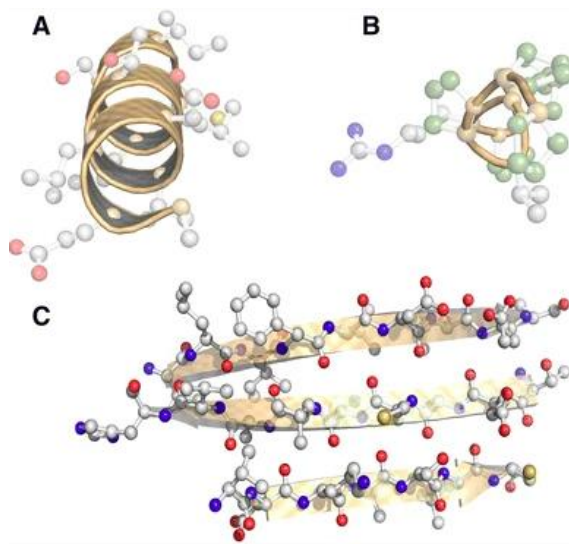


Figure 1-3. Peptide secondary structures (a) right-handed α -helix, (b) left-handed PPII, and (c) three β -strands forming a β -sheet. Reprinted with permission from ref.¹⁵ Copyright 2017 Springer Nature.

α -Helices typically form a right-handed coil consisting of at least four amino acid residues; β -sheet structures are formed from favorable interactions between peptide backbones. Interestingly, individual amino acids' propensities to form α -helices are relatively consistent regardless of sequence or environment, while β -sheet forming propensities are highly context dependent.¹⁶ Still, it is well-established that β -sheet formation is driven by hydrophobic aggregation and hydrogen bonding. β -strand sequences commonly have alternating hydrophobic and hydrophilic residues, resulting in two interfaces with favorable attractions.¹⁷ While the two types of PP helices (I and II) were typically associated with proline-rich sequences, these secondary structures have been observed in areas with low proline content as well (Figure 1-3).¹⁵

While most naturally-occurring proteins are made up of hundreds or even thousands of amino acids, designed shorter sequences could also self-assemble. These peptides assembled into

secondary structures and often could access more complicated hierarchical structures. A study published by Aggeli and coworkers observed the assembly of an eleven-residue sequence designed to form beta-sheet secondary structures.¹⁸ The assembly of the monomers was concentration dependent, and increasing the peptide concentration produced structures from simple helical tapes to self-supporting nematic gels. Slight chemical modifications to the amino acid sequence can often result in a drastic structural change and understanding the root of these changes is an important step towards being able to synthetically control them.

Synthetic design of peptide sequences with self-assembling propensities commonly involves amphiphilic peptide sequences or lipidated peptides. Amphiphilic molecules are ubiquitous in nature, and their assembly into vesicles or bilayers in aqueous solutions is straightforward: a hydrophobic region is sequestered, with the hydrophilic region facing the environment. The amphiphile molecular structures could be quite simple: for example, Yamada and coworkers reported bilayer formation from a lipid tail attached to a peptide headgroup of multiple glutamic acid residues.¹⁹ Peptide amphiphile-based soft materials are promising components of a wide variety of applications from tissue engineering to drug delivery.²⁰ An early muse of peptide assembly was collagen fibrils, which are composed of a triple-helical arrangement of peptide strands with a polyproline II helical secondary structure and serve as the scaffold for bone tissue.^{15,21-23} Attempts to synthetically design a collagen-like assembly typically utilized other organic substrates or reconstituted collagen protein.²⁴⁻²⁶

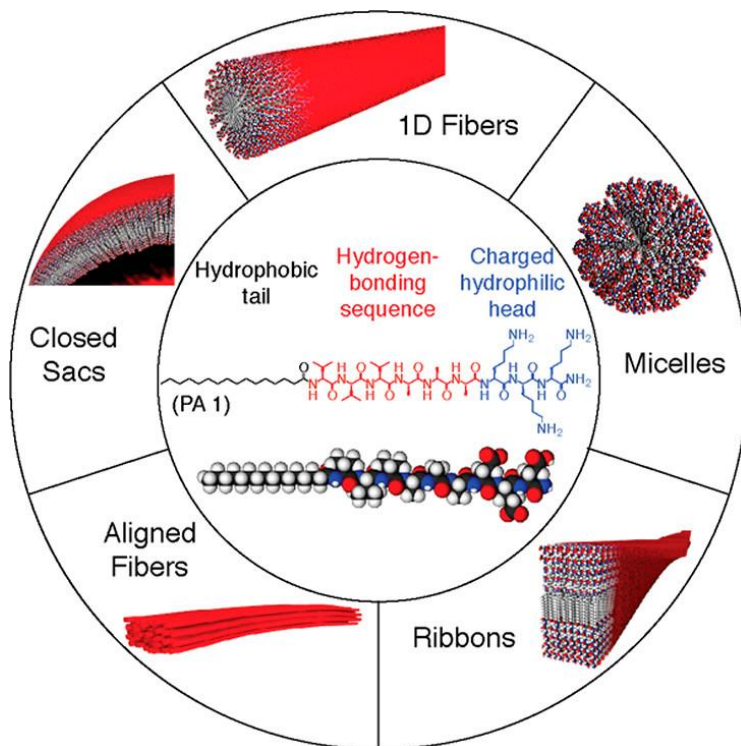


Figure 1-4. General design of a peptide amphiphile and potential nanoarchitectures. Reprinted with permission from ref.²⁷ Copyright 2017 American Chemical Society.

A landmark 2001 study published by the Stupp group was similarly inspired by bone tissue, but instead of mimicking collagen itself, they used knowledge about the mechanism of collagen structure to design a self-assembling peptide amphiphile driven by hydrophobic collapse, beta-sheet secondary structure formation, and covalent capture.²⁸ A significant body of work focusing on peptide amphiphiles has produced a wide variety of architectures and properties (Figure 1-4). The general peptide amphiphile can be modified with bioactive epitopes in order to create functional materials for applications including bone regeneration²⁹ and neural stem cell differentiation.³⁰

1.3 Peptide-Directed Biomineralization of Inorganic Materials

A significant amount of research has been done to understand peptide assembly in the context of NP synthesis and assembly. In addition to biomimetic materials, peptides with affinities for non-biologically relevant inorganic materials can be isolated using selection techniques such as phage display coupled with *in vitro* evolution.³¹ Phage display is useful for finding peptide sequences that match a target inorganic material, often involving a peptide binding to metal.³² This process reveals specific sequences with high affinities for the target, providing a starting point for endless syntheses (Figure 1-5).

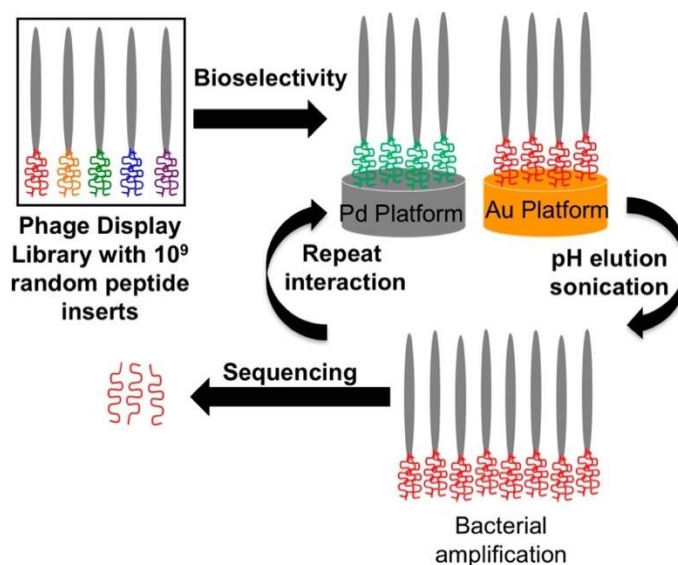


Figure 1-5. Summary of phage display methodology for identifying metal-binding peptides. Reprinted with permission from ref.³³ Copyright 2017 American Chemical Society.

By 2010, peptides with binding affinities for silver, gold, copper, nickel NPs were published, as well as other alloyed particles such a cobalt platinum and metal oxides like

titanium dioxide.^{32,34–38} Each of these peptides could be further investigated by studying the effects of solution conditions (*i.e.* pH and ionic character), amino acid sequence modifications, and peptide modifications (lipidation or other functionalization). The ease of the selection techniques generated a vast library of sequences with affinities for inorganic materials, while less work had focused on the relationship between molecular structure and NP interactions as these selection methods did not reveal any information about materials specificity. Palafox-Hernandez and coworkers published one of the first investigations into material-specific peptide binding, focusing on Ag and Au surfaces. Because these elements form structurally and chemically similar interfaces, multiple peptide sequences were known to have a binding affinity for both. Interestingly, peptides interact predominantly with the metallic surface on Au while solvent-mediated interactions dominate for Ag. The authors also analyzed the free energy of adsorption of all 20 naturally occurring amino acids at Au and Ag interfaces (Figure 1-6), concluding that adsorption preferences of peptides cannot be inferred from the amino acid preferences within the sequence.^{39,40}

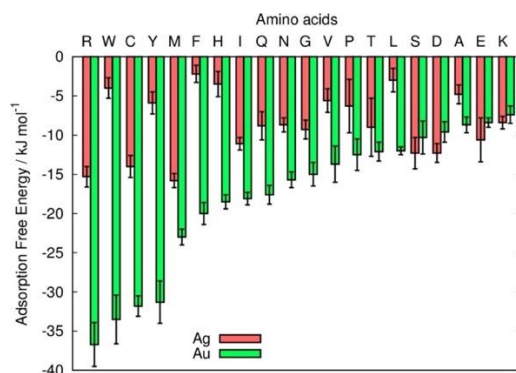


Figure 1-6. Calculated adsorption free energies at aqueous Ag and Au interfaces for the twenty naturally occurring amino acids. Reprinted with permission from ref.⁴⁰ Copyright 2014 American Chemical Society.

Another work from this ongoing collaboration between the Walsh and Knecht groups studied sequence modifications to common Au-binding peptides, establishing that single amino acid mutations can dramatically alter the peptide-Au surface interaction.⁴¹ Even atomic-level sequence modifications could change the way an entire peptide interacted with a surface,⁴² highlighting the sensitivity and inherent challenges to the methodology. While it proved difficult to engineer a peptide sequence designed to bind a specific material, studying the interaction of specific amino acids and peptide chains with inorganic surfaces did produce a few design rules: thiol and sulfur-containing moieties often had a high affinity, as did aromatic residues.^{33,39,40,43}

1.4 Peptide-Based Assembly of Gold Nanoparticles

By the mid-2000s, a general recipe for a peptide amphiphile that would self-assemble had been developed: some type of hydrophobic tail linked to a peptide that typically had two regions,^{44,45} at the peptide N-terminus were β -sheet forming amino acids to further encourage assembly, and the C-terminus amino acids would be hydrophilic (often acidic or basic residues) that could have a functional moiety or affinity for an inorganic material.⁴⁵ These design rules were adapted as the foundation of the work discussed in this dissertation. By lipidating a well-known gold-binding peptide sequence (A3),³⁸ Rosi and coworkers initiated a series of fundamental studies aimed at understanding and controlling peptide-based gold (Au) NP synthesis and assembly.

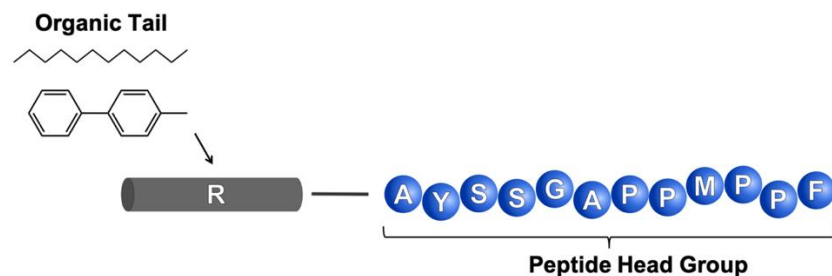


Figure 1-7. The first peptide conjugate designed by the Rosi lab consisted of an hydrophobic organic tail attached to the gold-binding peptide PEP_{Au} .

Rosi and coworkers began by preparing peptide amphiphiles by lipidating a Au-binding peptide sequence AYSSGAPPMPPF or A3^{37,38} (herein referred to as PEP_{Au}). PEP_{Au} was discovered through phage display methods for its ability to stabilize silver³⁷ and later Au NPs.³⁸ This sequence alone did not self-assemble, but the peptide could bind and stabilize metal ions in the presence of HEPES buffer.^{38,46,47} Attaching a C_{12} aliphatic tail to the N-terminus of PEP_{Au} results in formation of the $\text{C}_{12}\text{-PEP}_{\text{Au}}$ amphiphile, which assembles into 1-D twisted fibers in HEPES buffer.^{5,48} When gold ions are added to the assembly mixture, double-helical Au NP superstructures form (Figure 1-8).⁴⁹

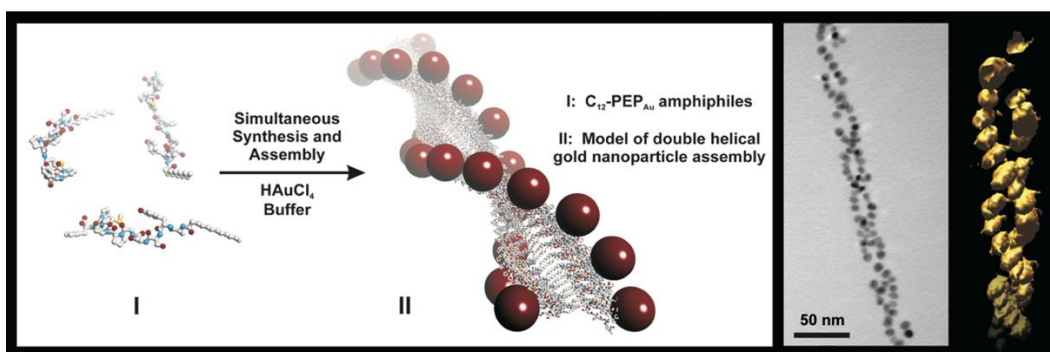


Figure 1-8. $\text{C}_{12}\text{-PEP}_{\text{Au}}$ assembly and double-helical Au NP superstructures.⁴⁹

With this seminal discovery, the stage was set for fundamental studies into the formation of these unique structures and diversification of the basic methodology. Spectroscopic studies of the peptide conjugate using circular dichroism (CD) spectroscopy and infrared (IR) spectroscopy showed evidence of β -sheet formation.⁵⁰⁻⁵² Early studies drew conclusions and produced rankings of the β -sheet forming propensity of the twenty natural amino acids, often studying their frequency in protein sequences known to form β -sheet secondary structures.⁵³⁻⁵⁵ In the C₁₂-PEP_{Au} assemblies, the N-terminal amino acids (AYSSGA) could be forming β -sheet structures, as Tyr is regularly reported as a high propensity residue while Ser, Ala, and Gly are ranked moderate to poor.^{53,54} While the current consensus is that a specific amino acids' likelihood of participating in β -sheets is highly context dependant,^{16,56} we can still use the individual propensities as a guide. Proline residues commonly form polyproline II secondary structures, so it was proposed PPMPPF formed PPII helices and interacted with the solution environment and/or Au NPs.⁴⁹ Initial assembly models described C₁₂-PEP_{Au} monomers assembled into a bilayer, with the aliphatic tails interacting at the core and the peptide C-terminus on the exterior. β -sheets twist in the right-handed direction to find the optimal geometry for the inter-strand hydrogen bonds,⁵⁷ resulting in a fiber with left-handed helicity. The fibers had a twisted ribbon morphology, a width of around 6 nm (corresponding to the length of two monomers) and a regular pitch of 84 nm. These distances also correlated with both the space between particles along the width of the fiber and the pitch of the Au NP double helices.

The method successfully coupled peptide self-assembly and NP nucleation and growth to produce a composite nanomaterial. It was noteworthy that the conjugate bearing the reverse

sequence (C₁₂-FPPMPPAGSSYA) did not yield fibers and no NP assemblies formed. At this point, a few things were clear: a hydrophobic tail and the specific sequence of the amino acids were integral to the production of superstructures, and this balance was relatively sensitive to perturbation. By building on this discovery, a diverse family of NP superstructures were produced using the basic components of an aliphatic tail and PEP_{Au}. Modifications to the peptide sequence had dramatic effects on the fiber and Au NP assembly, and could be used to precisely tune structure and morphology. Since the PEP_{Au} sequence is relatively hydrophilic and does not self-assemble in solution,^{38,49} the hydrophobic tail of the peptide conjugate molecule has an essential role in the superstructure assembly. Multiple studies explored this handle, generating different linear superstructures and size-controlled hollow sphere assemblies.⁵⁸⁻⁶¹ The synthetic method not only was ‘one-pot’ (*i.e.* consisting of a single reaction step), but the peptide conjugate assembly and NP growth needed to occur simultaneously.^{49,58,59}

1.4.1 Molecular Chirality Informs Nanoscale Chirality

Chirality plays a large role in biomolecule assembly: all amino acids are in the L form, peptides and proteins with D-amino acids are not compatible with living organisms. The helical structures thus far were produced with L-amino acids, and we reasoned that the chirality of the amino acids and the handedness of the superstructures were linked. To test this hypothesis, the conjugate was synthesized with D-amino acids, and indeed, C₁₂-D-PEP_{Au} produced mirror-image structures.⁶² The Au NP and superstructure dimensions were exactly the same between the left-handed and right-handed helices.^{49,62} Additionally, due to the plasmonic properties of Au NPs,

both structures displayed plasmonic chirality, visualized using circular dichroism (CD) spectroscopy (Figure 1-9).^{3,63,64} The signals were vertically mirrored at 562 nm, corresponding to the collective surface plasmon resonance of the assembled Au NPs, closely imitating the theoretical prediction.⁶²

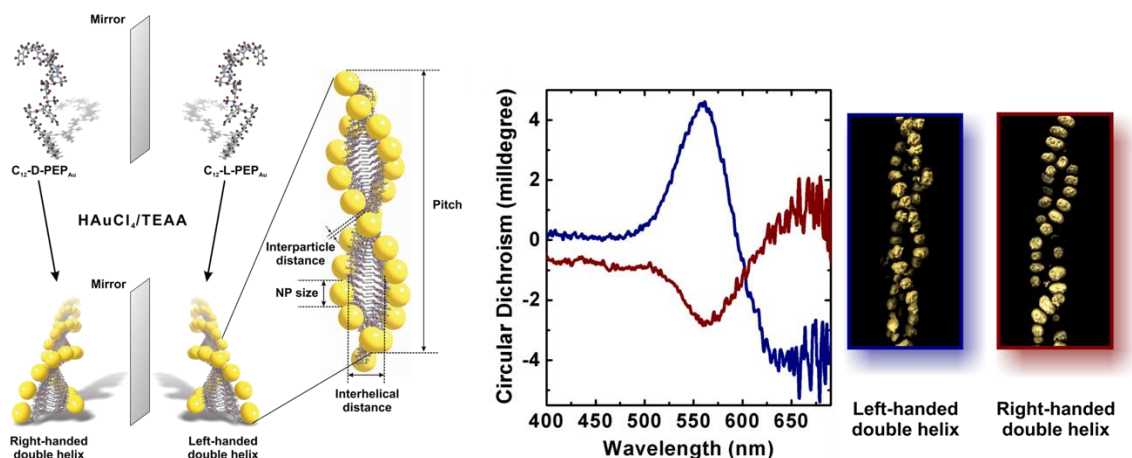


Figure 1-9. Mirror-image double helical Au NP assemblies; the handedness of the helices is controlled by the chirality of the constituent amino acids.⁶²

These CD signals could be modified through the interparticle gap and NP size; specifically, decreasing the distance between neighboring particles and increasing NP diameter resulted in a red shift of the plasmonic peak and an increase in magnitude.^{3,63,64} The optical signal of the helices theoretically could be blue-shifted by decreasing the Au NP size, though experimentally this was accompanied by a decrease in signal. To produce a blue-shifted response with consistent magnitude, the Au NPs were coated in a silver shell. Here, molecular chirality informed nanoscale chirality and the intensity and position of the chiroptical response could be selectively tuned. This work also introduced post-synthetic modifications, suggesting that more complex nanomaterials could be synthesized through shell-growth on the Au NPs.

The next project was a large, systematic study of the effect of the aliphatic chain length and peptide ‘valency’ (defined as the number of peptide chains attached to a single aliphatic tail).⁶¹ One can consider this as the prologue to a second era of projects, as the structures presented led directly to the discovery of a new type of superstructure and a new branch of research questions.

1.4.2 Nanoscale Architecture Transformation from Double to Single Helices

A body of work had been generated using the peptide conjugates for NP assembly, leading to a foundational understanding of the role of the organic tail and peptide sequence along with the observation that the helical nanoscale structure heavily influenced the materials’ optical properties.^{49,58,60,62,65} However, a continuous spectrum of modifications and their structural effects had not been established. In this project, the peptide conjugates newly defined as ‘monovalent’ (*i.e.*, one peptide chain attached to an aliphatic tail) were studied at tail lengths from twelve carbons to eighteen.⁶¹ Additionally, ‘divalent’ and ‘trivalent’ peptide conjugates were introduced, each with the series of tail lengths to study the effect of peptide steric requirements on the assembly (Figure 1-10).

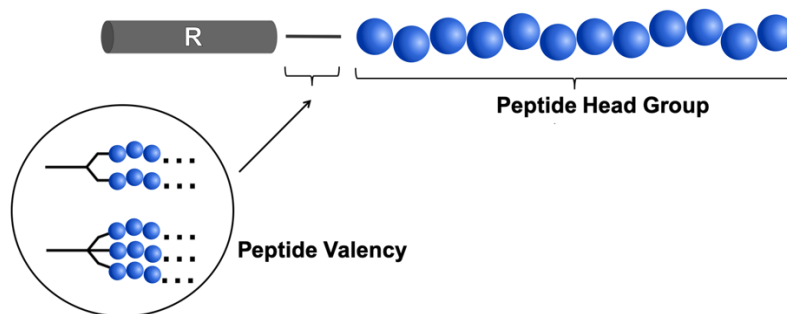


Figure 1-10. Design of ‘multivalent’ conjugates.

In order to synthesize a family of multivalent peptides with structural continuity, the basic molecular structure was slightly modified. Instead of using N-hydroxysuccinimide terminated aliphatic chains that would react with a terminal amine group, Cu(I)-catalyzed azide–alkyne cycloaddition click chemistry was used.^{66,67} The alkyne group(s) were installed on the aliphatic tail, and peptide synthesis was terminated with the coupling of an azide functional group; this coupling method would be used from this point on. The fiber and NP assemblies of the 12 new peptide conjugates were then studied. The monovalent and divalent conjugates were found to predominantly form fibers, while the trivalent conjugates formed spherical aggregates; fiber yield was generally observed to increase with the aliphatic tail length due to the increased hydrophobic:hydrophilic ratio, while adding peptide head groups increased the hydrophilic component, leading to spherical assemblies or soluble conjugates. In general, the fiber-forming conjugates directed the assembly of roughly double-helical gold nanoparticle superstructures.

In some cases, the divalent conjugate $C_{18}-(PEP_{Au})_2$ directed the formation of gold nanoparticle single helices rather than double helices. After extensive investigation into potential sources of this nanoscale structural heterogeneity, it was discovered that the conjugates

responsible for single helix assembly had a slightly higher mass, specifically 32 au more than $C_{18}-(PEP_{Au})_2$. This mass difference was determined to be the addition of two oxygen atoms via oxidation of the methionine residues to methionine sulfoxide.⁶⁸ When conjugates were prepared with the methionine residues intentionally oxidized, a pure product of Au NP single helices was observed (Figure 1-11). These left-handed helices were composed of oblong NPs rather than spherical and had a helical pitch of approximately 94 nm. Additionally, AFM images showed the formation of helical ribbons rather than twisted—at this point, it was surmised that twisted ribbon fibers preferably bound two NPs to the edges of the ribbon while only the exterior of the helical ribbons was decorated. Additionally, the structural transformation was accompanied by a significant increase in chiroptical signal.⁶⁸

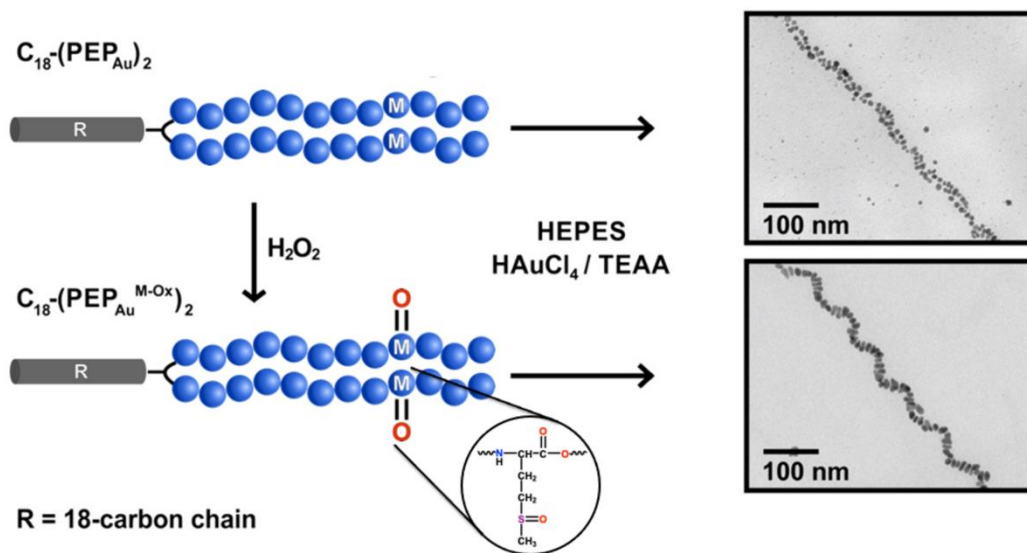


Figure 1-11. Oxidation of the peptide methionine residues to methionine sulfoxide caused a structural transformation from Au NP double helices to single helices.

The secondary structure of the peptide conjugate fibers was consistent with the unoxidized conjugate. The FTIR spectrum contained peaks attributed to parallel β -sheet secondary structure and ordered packing of the alkyl chain tails. The presence of β -sheets was confirmed in the CD spectrum; however, this peak was slightly blue-shifted, attributed to the superposition of peaks from the β -sheets and PPII secondary structures. New information about the conjugate molecular packing was determined using X-ray diffraction (XRD) and solid state nuclear magnetic resonance spectroscopy (ssNMR). Using XRD, the hydrogen-bonding distance between peptide backbones was calculated to be 4.6 Å and two different inter-sheet distances were also measured at 6.5 Å and 9 Å. Coupled with ssNMR spectra, we were able to define the locations of these distances. A single set of peaks characteristic of PPII secondary structures was observed for the C-terminal residues, indicating that the C-terminal amino acids of all molecules assembled into the same PPII secondary structure. Multiple sets of peaks attributed to Ala₁ indicated multiple structures at the N-terminus, with the two dominant peak sets characteristic of β -sheets, while the third set of peaks was attributed to peptide that was not incorporated into the ordered fibers.

Integration of these data led to a proposed assembly model for the peptide conjugates: the aliphatic tail aggregation induced parallel alignment of the peptides into a ‘class 3 steric zipper’, in which there are two different inter-sheet interfaces (corresponding to the two different d-spacings of 6.5 Å and 9 Å). The different inter-sheet spacings is due to the Tyr residue, as the bulky aromatic residue adopts a stacked ring structure and requires more space than Ala, Ser, and Gly (Figure 1-12a). The secondary structure transition occurs over a single residue, clearly

splitting the peptide into two distinct regions: β -sheet forming amino acids packed at the core of the amyloid fibril and PPII forming amino acids facing the solution environment.

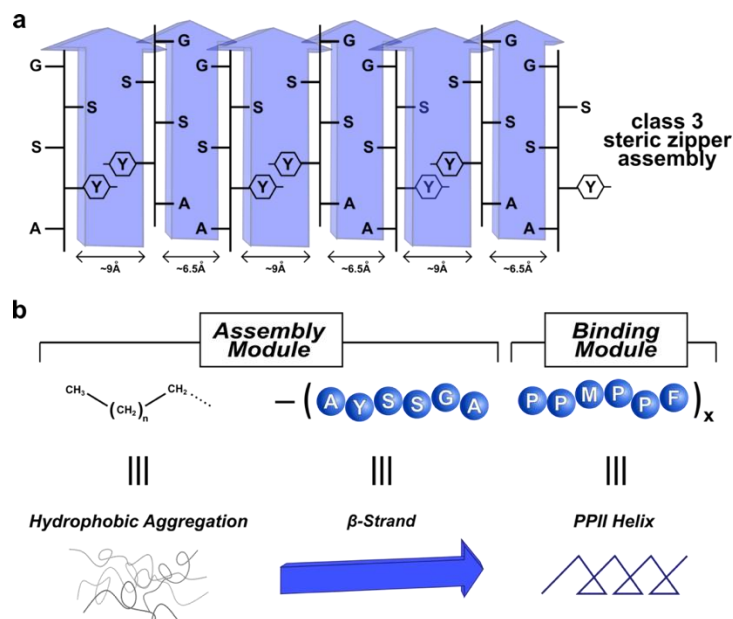


Figure 1-12. Assembly of the single helix system showing (a) parallel β -strand alignment with two different inter-strand spacing and (b) modules of the peptide conjugate.

This assembly model further differentiated the ‘modules’ within the peptide conjugate (Figure 1-12b). The N-terminal amino acids are part of the assembly module, since their β -sheet formation likely sterically blocks any Au NP association.^{68,69} The C-terminal amino acids molecular composition was important for Au NP-binding, but also influenced the fiber morphology and resultant superstructure morphology. The single helices provided a new platform for investigation, and the next phase of research focuses on understanding their origin and how to manipulate their structure and properties.

1.4.3 Controlling Single Helix Morphology and Assembly by Modifying Length of Aliphatic Tail

Since the effect of the aliphatic tail length on double-helical assemblies had recently been established,⁵⁸ a logical step forward was to examine the single helices in a similar manner. To this end, a family of $C_x-(PEP_{Au}^{M-ox})_2$ conjugates were synthesized, with $X = 14 - 22$.⁷⁰ Consistent with the double helix system, C_{14} did not form fibers in solution. C_{16-22} all formed helical ribbon fibers, with the ribbon width and helical pitch increasing with aliphatic tail length. The aliphatic tail length also had a systematic effect on the NP assemblies: as aliphatic tail increased the helical pitch increased and the particle size decreased (Figure 1-13). The aliphatic tail length directly dictated the conjugate assembly rate, and the conjugate assembly rate indirectly influenced the NP nucleation and growth. The conjugate with ‘optimal’ rate of assembly, C_{18} , produced the best superstructures because it incorporated the maximum amount of Au NP seeds during its assembly phase. The longer tail conjugates, C_{20} and C_{22} , assembled rapidly, limiting Au NP growth on the fibers and producing an excess of discrete Au NPs.

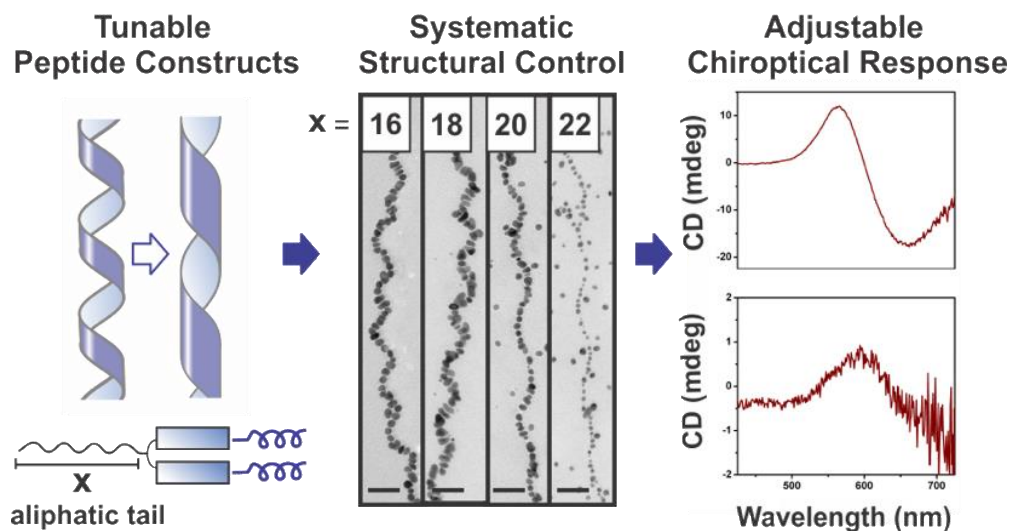


Figure 1-13. Aliphatic tail length of divalent conjugates controlled helical pitch length, Au NP size, and chiroptical signal.⁷⁰

Additionally, the structural changes across the C_{16-22} family of superstructures influenced the chiroptical properties of the helices. As the tail length increased, the chiroptical response decreased. One can reason that the signal could be further increased if the helical pitch was decreased (aliphatic tail length decreased as well); however, the C_{14} conjugate did not assemble into fibers and yielded only discrete Au NPs (Figure 1-14). This observation presented a challenge and an opportunity.^{58,60,65}

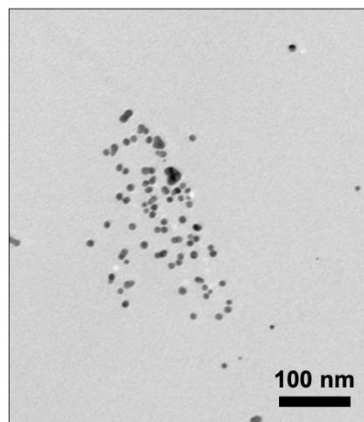


Figure 1-14. Discrete Au NPs produced in the presence of C_{14} -(PEP_{Au}^{M-ox})₂.

Previously, we had determined that modifications of repeat units or alanine residues were successful in increasing the β -sheet formation and assembly propensity of the peptide conjugates. Following the systematic study of aliphatic tail length on the Au NP single helices, it was clear that i) decreasing the aliphatic tail should theoretically yield a higher chiroptical response and ii) tails with less than C_{16} were no longer balanced for amphiphile assembly. In order to regain assembly and produce helices with an even more intense chiroptical signal, modifications to the β -sheet region were proposed.⁷¹ The conclusions from this study will be presented in Chapter 2.

In order to determine the mechanism of structural transformation from double to single helices generated by the oxidation of methionine, a family of peptide conjugates with C-terminal modifications was designed.⁴² Specifically, the oxidation state of methionine and its' position in the sequence were systematically varied. This work was accompanied by a computational investigation into the peptide-Au interactions. Experimentally, it was observed that larger particles were generally formed from methionine sulfoxide-containing conjugates than those

with methionine. Additionally, within the family of methionine sulfoxide conjugates, larger particles were formed when M-ox was at the peptide 11th position than at the 9th or 7th. In order to understand these results, theoretical modeling was used to predict the residue-surface contact for each residue within the peptide sequence. By analyzing the secondary structure conformational assembly, we could draw conclusions about the binding interactions of the peptide variants. In short, these results showed a significant decrease in Au-surface contact when methionine was oxidized to methionine sulfoxide.⁴² Due to its' sulfur-containing side chain, a Met residue would have a high affinity for gold surfaces, but when oxidized, the sulfur is sterically blocked from the Au NPs. At this point, one could link the formation of double versus single helices to the peptide gold binding propensity. This hypothesis is examined in detail in Chapter 3 of this dissertation.

1.5 Key Gaps in Knowledge and Objectives of this Dissertation

My research has focused on building understanding of the tunable handles inherent to the amino acid sequence of Au NP-assembling peptide conjugates, then leveraging this information to develop nanostructures with acute control over morphology and function. Previous to my work in the group, the effect of the hydrophobic tail and peptide conjugate valency on Au NP assemblies had been systematically studied, establishing a method to control the amphiphilic ratio of the conjugate. Next, following the discovery and characterization of the Au NP single helices, the pitch length and Au NP size were directly and indirectly, respectively, correlated to

the length of the divalent conjugates' aliphatic tail. My first project sought to understand the relationship between the length of the aliphatic tail and the conjugates' assembly propensity, ultimately developing an amino acid modification strategy to control the peptide conjugate fiber assembly propensity.

In Chapter 2, I studied the effect of hydrophobic modifications to the peptide's β -sheet forming amino acids. By substituting amino acids to the peptide 4th position, we can systematically increase the β -sheet and assembly of the peptide conjugate, producing Au NP superstructures with the shortest pitch yet. This modification strategy was generalizable and was used to encourage assembly in monovalent conjugates as well. Through this work, I further developed our knowledge of the N-terminal amino acids' role in the assembly of superstructures.

In Chapter 3, I aimed to determine the source of the double- to single-helical structural transformation studying peptide conjugates with modifications to incrementally decrease the Au-binding affinity of the 9th amino acid. Previously, we knew that the structural change was initiated by methionine oxidation, but the mechanistic source was not known. This work demonstrated that a moderate to low binding affinity was necessary to form well-defined Au NP single helices. A slight increase in affinity would produce double-helical assemblies and a further increase produced disordered aggregates. A decrease in affinity would result in discrete, unassembled Au NPs. These experimental observations were corroborated with a computational investigation into the 'binding scores' of the variant peptide sequences.

The work in Chapter 3 can be viewed as peptide modifications within the single helix methodology, while Chapter 4 moves beyond. Previously, we have not utilized charged amino

acids in our design system. While charged amino acids like glutamic acid were predicted to have an optimal binding score (and therefore synthesize Au NP single helices) fiber formation was disrupted by the increased charge density at the C-terminus. This project explored electrostatically-driven co-assembly strategies to introduce complexity and increase the capabilities of the assembly system, laying the groundwork for a new phase of research.

2.0 Leveraging Peptide Sequence Modifications to Promote Assembly of Chiral Helical Gold Nanoparticle Superstructures

This work written in collaboration with Soumitra Mokashi Punekar, Camera Hogan, and Nathaniel L. Rosi, is reprinted with permission from *Biochemistry* **2020**, *60*, 1044-1049. Copyright 2020, American Chemical Society. The supporting information is found in Appendix A.

2.1 Introduction

Plasmonic metal nanoparticles (NPs) are important building blocks for constructing a wide variety of materials whose properties depend not only on the size, shape, and composition of the component NPs but also their precise arrangement in 3-D space.^{72–75} Helical NP superstructures have drawn widespread interest because they exhibit strong plasmonic chiroptical activity^{63,76,77} which make them attractive for a range of potential applications.^{78,79} Their plasmonic chiroptical response derives from the intrinsic chiral 3-D arrangement of the component NPs, and the intensity of the response depends largely on metrics such as helical pitch length and NP dimensions, with the strongest chiroptical signal predicted to arise from helices with short pitch and large NPs.^{3,80} Rational construction and systematic structure and property optimization of helical NP superstructures, and NP superstructures in general, requires robust assembly platforms. To this end, we have developed a peptide-based platform for assembling NPs into structurally-complex architectures.^{49,58,81,59,82,83,65,61,84,85} Much of our research has focused on using this peptide platform to design and construct chiral, helical NP assemblies, in particular gold (Au) NP-based single^{42,84–86} and double helices.^{49,61,81,83}

Our assembly strategy is based on peptide conjugates, which are molecular agents consisting of an organic tail appended to a NP-binding peptide.⁴⁹ When a given peptide conjugate is dissolved in an aqueous assembly buffer along with appropriate inorganic salts and reducing agents, it directs the synthesis and assembly of inorganic NPs; NP nucleation/growth and assembly are coincident processes.^{49,59} Here, we restrict our discussion to Au-binding peptide conjugates of the general formulae $C_x-(PEP_{Au})_y$ ($PEP_{Au} = AYSSGAPPMPPF$; also

known as A3³⁸), which feature prominently in this study. An individual Au-binding peptide conjugate can be subdivided into multiple sections that each play a key role in the assembly process. First, each peptide conjugate has an aliphatic tail (C_x) appended to the N-terminus of PEP_{Au}. The aliphatic tail helps drive peptide conjugate aggregation in aqueous assembly media and plays a key role in dictating the morphology of the target assembly.^{49,58,87} Second, the six N-terminal amino acids of PEP_{Au}, AYSSGA, which are adjacent to the aliphatic tail, also play an important role in peptide conjugate assembly. Specifically, they engage in inter-peptide β -sheet formation, which helps direct the assembly of peptide conjugates into chiral fibers, including helical coils and twisted ribbons.^{49,84} The third and final section consists of the C-terminal amino acids, PPMPPF. This region of PEP_{Au} adopts a PPII conformation^{84,88} and experimental and computational studies indicate that this region strongly associates with Au NP surfaces.^{84,42,43}

In the context of building and optimizing the chiroptical properties of helical NP superstructures, we have successfully demonstrated that: i) the global molecular structure and composition of the peptide conjugates can be modified to direct formation of either single or double helices;^{49,61,65,83,84} ii) varying the amino acid sequence within the PPII region profoundly affects the dimensions of the component Au NPs in single-helical superstructures;⁴² and iii) small adjustment of the aliphatic tail length can lead to dramatic changes in the length of the helical pitch of these assemblies.^{61,86} For the latter, we specifically reported that C_x-(PEP_{Au}^{M-ox})₂ (x = 16-22 and M-ox = oxidized form of methionine) assembles into helical ribbon fibers in HEPES buffer, such that the ribbon width and helical pitch increase with increasing aliphatic tail length.⁸⁶ This effect translates to the final Au NP single helices: C₁₆₋₂₂-(PEP_{Au}^{M-ox})₂ direct the assembly of single-helical superstructures ranging in average pitch value from 80-120 nm.

Contrary to the observed trend, $C_{14}-(PEP_{Au}^{M-ox})_2$, when subjected to similar NP superstructure synthesis and assembly conditions, did not assemble into helical fibers and consequently yielded only free unassembled Au NPs.⁸⁶ We reason that $C_{14}-(PEP_{Au}^{M-ox})_2$ exhibits diminished assembly propensity owing to its shorter (less hydrophobic) aliphatic tail. In order to further decrease the pitch within this family of helices and ultimately increase the plasmonic chiroptical signal, we must identify an alternate strategy for promoting the assembly of peptide conjugates with aliphatic tails shorter than C_{16} . In this study, we examine for the first time whether modifications to the β -sheet forming region of PEP_{Au} affect peptide conjugate assembly, potentially providing yet another synthetic handle for tuning the metrics and properties of helical NP superstructures.

2.2 Results and Discussion

We designed a series of sequence modified $C_{14}-(PEP_{Au}^{M-ox})_2$ peptide conjugates having incrementally increasing relative hydrophobicity in their β -sheet forming region in order to promote fiber and superstructure assembly (Figure 2-1). Since the β -sheet forming residues (-AYSSGA) are not associated with gold-binding in the proposed assembly model,²⁰ we hypothesize that replacing the hydrophilic S residue with more hydrophobic amino acids will effectively increase the hydrophobic to hydrophilic ratio in $C_{14}-(PEP_{Au}^{M-ox})_2$ without detrimentally affecting NP binding. To test this hypothesis, we synthesized two new backbone modified peptide conjugates: $C_{14}-(AYSXGAPPM^{ox}PPF)_2$ where X = T or F (Appendix Figure 1, Appendix Figure 2). Hereafter, each peptide conjugate is referred to by its modified amino acid

residue: $C_{14}-(AYSFGAPP^{M-ox}PPF)_2 = C_{14}-(PEP_{Au}^{M-ox})_2^F$. Our established model for $C_{18}-(PEP_{Au}^{M-ox})_2$ assembly²⁰ guided our decision to substitute at the fourth position. According to this model, there are two different interfaces between the stacked β -sheets: an aromatic interface defined by the Y (position 2) and S (position 4) side chains (~ 9 Å distance between stacked β -sheets) and an interface defined by the A (position 1) and S (position 3) side chains (~ 6.5 Å distance between stacked β -sheets). Because the larger Y-S interface is dictated by the steric bulk of Y, we reasoned that replacing the S at the fourth position with larger, more hydrophobic residues (T or F) would not significantly disrupt β -sheet stacking. We note that similar peptide sequence modifications have been shown to significantly affect peptide assembly. Stupp *et al.* reported that the morphology of 1D fibers derived from a family of peptide conjugates can vary based on the relative position of hydrophilic and hydrophobic amino acids,⁸⁹ and Stevens *et al.* showed that minute backbone changes—such as S to T substitution—can alter peptide fiber morphology from twisted to planar ribbons.⁹⁰

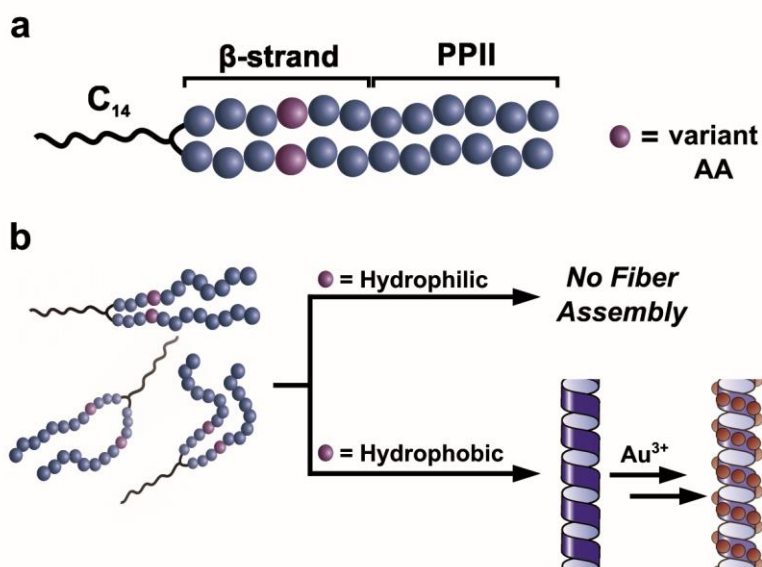


Figure 2-1. Peptide conjugate design and β -sheet modification strategy for C_{14} -(PEP_{Au}^{M-ox})₂. (a) The peptide conjugates contain a C_{14} aliphatic tail attached to the N-terminus of the peptide, which has a β -sheet-forming region and an inorganic particle binding region (PPII section). (b) The fourth amino acid in the sequence will be replaced with increasingly hydrophobic amino acids, which are expected to increase the assembly propensity of the peptide conjugate and thereby promote the assembly of Au NP superstructures.

We dissolved each conjugate in 0.1 M HEPES buffer (4-(2-hydroxyethyl)-1-piperazineethanesulfonic acid) buffer (pH =7.3) at room temperature and examined their resulting assemblies using transmission electron microscopy (TEM). Images of negatively stained samples revealed that only C_{14} -(PEP_{Au}^{M-ox})₂^F assembles into 1D fibers (Figure 2-2b), while C_{14} -(PEP_{Au}^{M-ox})₂^S and C_{14} -(PEP_{Au}^{M-ox})₂^T do not assemble into any well-defined structures (Figure 2-2a, Appendix Figure 3). Circular dichroism (CD) spectroscopy and Fourier transform infrared (FTIR) spectroscopy were used to determine peptide secondary structure.⁵⁰ CD spectra of C_{14} -(PEP_{Au}^{M-ox})₂^F display characteristic β -sheet signals at \sim 215-220 nm,^{84,86,50,91} while spectra of C_{14} -(PEP_{Au}^{M-ox})₂^T and C_{14} -(PEP_{Au}^{M-ox})₂^S reveal peaks at \sim 205 nm which is indicative of unassembled structures in solution (Figure 2-2c).^{84,86,92,93} Similarly, FTIR spectra of C_{14} -(PEP_{Au}^{M-ox})₂^F have distinct amide I peaks centered at \sim 1630 cm^{-1} indicative of β -sheet secondary structure,⁹⁴ while C_{14} -(PEP_{Au}^{M-ox})₂^T and C_{14} -(PEP_{Au}^{M-ox})₂^S display broad peaks centered around \sim 1645 cm^{-1} , characteristic of unordered structure (Figure 2-2d).^{84,86,94} Taken together, both microscopic and spectroscopic data are in good agreement and indicate that C_{14} -(PEP_{Au}^{M-ox})₂^F assembles into fibers. We examined the fiber morphology using atomic force microscopy (AFM), which revealed tightly coiled helical ribbons with an average ribbon width of \sim 28 nm and average helical pitch of \sim 65 nm (Figure 2-2e). We note that both the ribbon width and pitch

are significantly shorter than what we observed for $C_{16}-(PEP_{Au}^{M-ox})_2$ (~ 47 nm and ~ 82 nm, respectively).⁸⁶ Collectively, the microscopy and spectroscopy data indicate that modification of the β -sheet region of PEP_{Au} can significantly affect peptide conjugate assembly behavior.

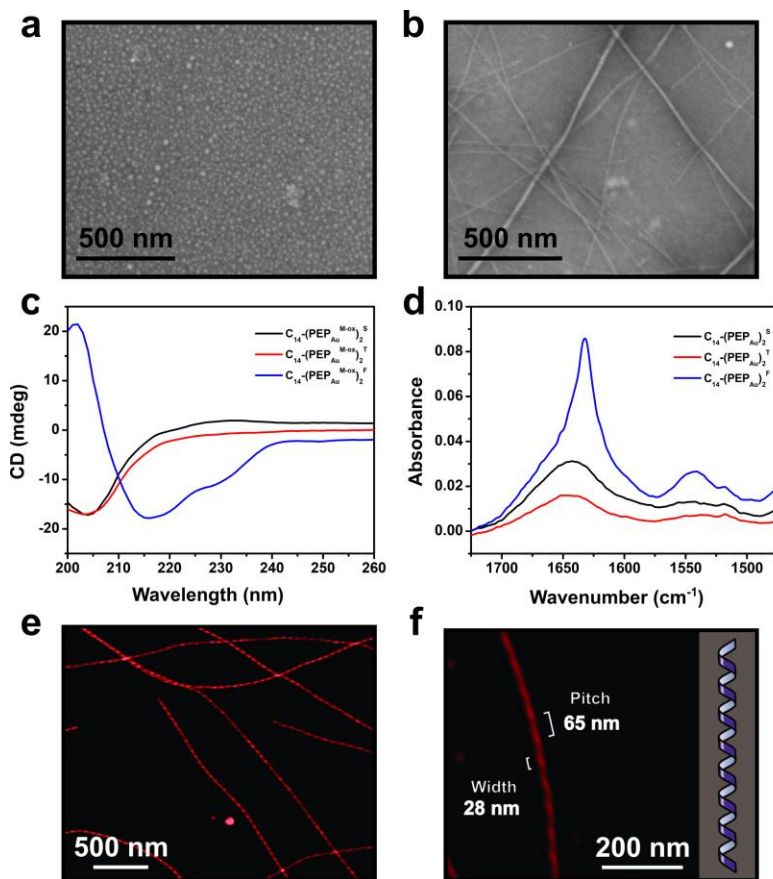


Figure 2-2. Negatively-stained TEM images of (a) $C_{14}-(PEP_{Au}^{M-ox})_2^T$ and (b) $C_{14}-(PEP_{Au}^{M-ox})_2^F$ assemblies. (c) CD and (d) FTIR spectra of $C_{14}-(PEP_{Au}^{M-ox})_2^X$ assemblies. (e) Low and (f) high magnification AFM images of $C_{14}-(PEP_{Au}^{M-ox})_2^F$ fibers.

To investigate whether trends in the assembly behavior of the modified peptide conjugates translated to similar patterns in NP assembly, we subjected each sequence-modified peptide conjugate to our established superstructure assembly conditions.⁸⁴ As previously

discussed, $C_{14}-(PEP_{Au}^{M-ox})_2^S$ yielded discrete Au NPs (Appendix Figure 6). $C_{14}-(PEP_{Au}^{M-ox})_2^T$ also yields discrete NPs, which is consistent with our observation that $C_{14}-(PEP_{Au}^{M-ox})_2^T$ does not assemble (Figure 2-3a). However, $C_{14}-(PEP_{Au}^{M-ox})_2^F$ yields well-defined Au NP single helices (Figure 2-3b, c). The average helical pitch is ~ 67 nm (Figure 2-3d), which is in agreement with the helical pitch observed for $C_{14}-(PEP_{Au}^{M-ox})_2^F$ helical fibers.

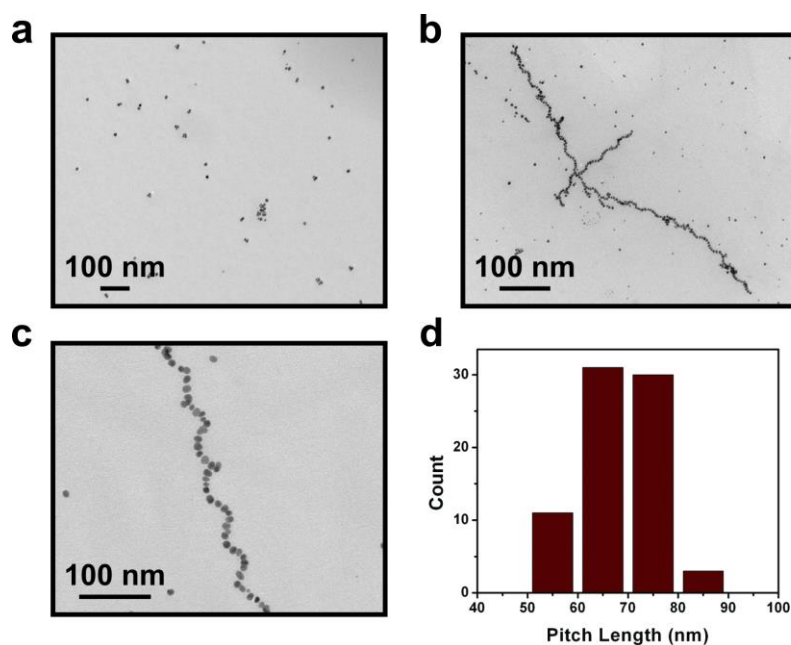


Figure 2-3. Au NP assemblies formed using backbone modified peptide conjugates: (a) $C_{14}-(PEP_{Au}^{M-ox})_2^T$ results in discrete unassembled Au NPs; (b,c) $C_{14}-(PEP_{Au}^{M-ox})_2^F$ directs the assembly of Au NP single helices. (d) Helical pitch distribution of single helices derived from $C_{14}-(PEP_{Au}^{M-ox})_2^F$.

The NPs comprising the single helices have an average length and width of 11.4 ± 2.1 nm and 7.2 ± 2.3 nm, respectively (Figure 2-4).

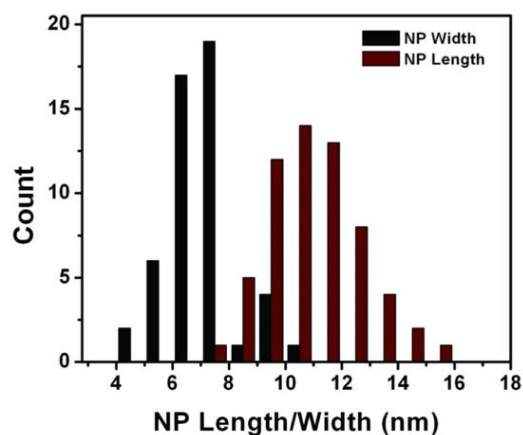


Figure 2-4. Particle dimensions of Au NPs in single helices prepared using C_{14} -(AYSFGAPPM^{ox}PPF)₂.

As described in our prior studies, the oblong shape of the Au NPs can be attributed to the oxidized methionine residue within the peptide sequence.⁴² Importantly, single helices derived from C_{14} -(PEP_{Au}^{M-ox})₂^F exhibit a distinct chiroptical response that is not observed for the products of the C_{14} -(PEP_{Au}^{M-ox})₂^S and C_{14} -(PEP_{Au}^{M-ox})₂^T-based reactions (Figure 2-5).

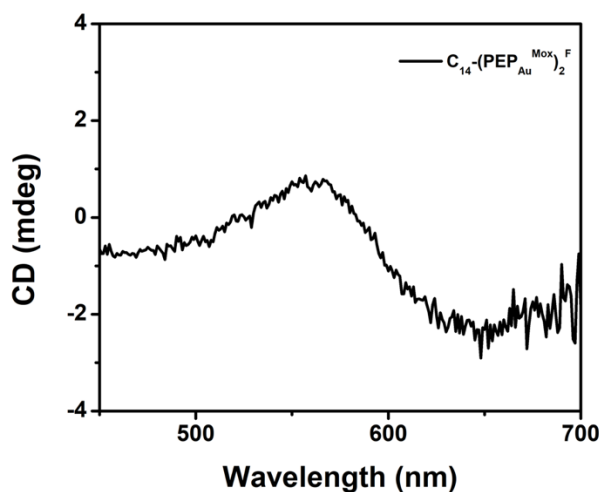


Figure 2-5. CD spectrum of single helices prepared using C_{14} -(AYSFGAPPM^{ox}PPF)₂ showing the plasmonic chiroptical signal at ~565 nm.

We note, however, that the chiroptical signal intensity may be further optimized by improving product yield. Nevertheless, these results represent a significant advance in this methodology: acute molecular modifications to the β -sheet region of the peptide conjugates manifest on the nanoscale in the assembly of helical superstructures.

Encouraged by these results, we turned our attention to a family of double-helical superstructures prepared using C_x -PEP_{Au} conjugates.^{49,81,83} We previously reported that C_{12} -PEP_{Au} assembles into twisted fibers and directs the assembly of Au NP double helices exhibiting a regular pitch of ~ 85 nm.⁴⁹ Attempts to decrease the pitch by shortening the aliphatic tail were unsuccessful, because C_{10} -PEP_{Au}, like C_{14} -(PEP_{Au}^{M-ox})₂, does not assemble into fibers in the aqueous HEPES buffer. We predicted that the β -sheet modification strategy again could be leveraged to produce new peptide conjugates that would form fibers and subsequently direct the assembly of Au NP double helices. To test this prediction, a similar series of peptide conjugates were synthesized: C_{10} -AYSXGAPPMPPF, where X = T or F (C_{10} -PEP_{Au}^T and C_{10} -PEP_{Au}^F; Appendix Figure 8, 9). When dissolved in 0.1 M HEPES, only the most hydrophobic peptide conjugate, C_{10} -PEP_{Au}^F, assembles into fibers (Figure 2-6a) as determined via TEM imaging. A negative band at ~ 220 nm in the CD spectrum and an amide I peak at ~ 1630 cm⁻¹ in the FTIR spectrum of the assembled fibers (Figure 2-6b, c) is attributed to the presence of β -sheet secondary structure, which is consistent with our previous studies.⁴⁹ In contrast, CD and FTIR spectra of C_{10} -PEP_{Au}^S and C_{10} -PEP_{Au}^T show no evidence of β -sheet structure. C_{12} -PEP_{Au} assembles into fibers that resemble twisted ribbons,⁴⁹ and we predicted that C_{10} -PEP_{Au}^F fibers

would adopt a similar morphology. However, AFM imaging of the C_{10} -PEP_{Au}^F fibers does not reveal a discernable morphology (Figure 2-6d, Appendix Figure 11).

We proceeded to investigate whether these modified peptide conjugates could direct the assembly of Au NP superstructures. C_{10} -PEP_{Au}^S and C_{10} -PEP_{Au}^T yield Au NP particles and aggregates, as predicted based on the fact that neither assembled into fibers (Appendix Figure 12). C_{10} -PEP_{Au}^F, however, directs the assembly of 1D NP assemblies (Figure 2-6e, Appendix Figure 13). Although the superstructures are not as well-defined as the pristine double helices produced using C_{12} -PEP_{Au},^{49,81,83} they do contain distinct double-helical regions, from which an average pitch of 68.5 ± 13.8 nm was determined. The particles within the superstructures have an average length and width of 8.6 ± 1.5 nm and 9.4 ± 1.8 nm, respectively (Appendix Figure 14). These particles are more spherical than those in the single helices, because in this case, the methionine is not oxidized.⁴²

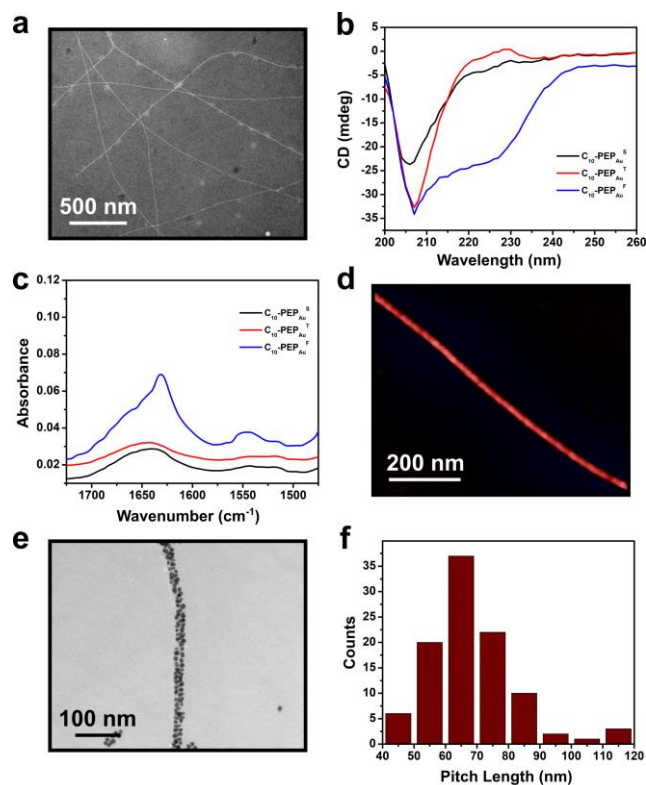


Figure 2-6. (a) Negatively-stained TEM image of C_{10} -PEP $_{Au}^F$ fibers. (b) FT-IR and (c) CD spectroscopy of C_{10} -PEP $_{Au}^x$ assemblies. (d) AFM of C_{10} -PEP $_{Au}^F$ fibers. (e) TEM image of Au NP superstructure assembly formed using C_{10} -PEP $_{Au}^F$ and (f) helical pitch distribution of C_{10} -PEP $_{Au}^F$ -based superstructures.

These results successfully demonstrate that an identical set of amino acid modifications can be applied to construct two different chiral architectures: Au NP single helices and Au NP double helices. In both cases, the assembly propensity of peptide conjugates with shorter aliphatic tails can be increased by substituting hydrophilic S with hydrophobic F. Therefore, this amino acid substitution strategy is a powerful and generalizable approach to program the assembly of chiral Au NP superstructures.

2.3 Conclusions

In this report, we demonstrate that single amino acid modifications can promote the assembly of two different peptide conjugates into fibers of varying morphologies. We then use these designed peptide conjugate variants to construct chiral superstructures, including Au NP single helices that exhibit a distinct chiroptical response. In order to fully realize the promise of these new materials, future synthetic optimization is necessary to increase superstructure yield and maximize chiroptical signal. More generally, our studies show that synthetically modifying the β -sheet region of these gold-binding peptide conjugates allows for further increased control over NP assembly and that molecular chemistry can be used to dramatically influence nanomaterial design. In the future, we intend to further investigate this relationship through expanded studies that specifically examine the effects of amino acid steric bulk and charge.

2.4 Experimental Methods

2.4.1 General Methods and Materials

All chemicals were obtained from commercial sources and used without further purification. All peptides were synthesized using established microwave assisted solid phase peptide synthesis protocols on a CEM Mars microwave. NanoPure water (18.1 m Ω) from Barnstead Diamond water purification system was used to prepare all aqueous solutions.

Peptides were purified by reverse-phase high-performance liquid chromatography (HPLC) on Agilent 1200 liquid chromatographic system equipped with diode array and multiple wavelength detectors using a Zorbax-300SB C₁₈ column. Peptide masses were confirmed by liquid chromatography-mass spectrometry (LC-MS) data using Shimadzu LC-MS 2020. UV-vis spectra were collected using an Agilent 8453 UV-Vis spectrometer with a quartz cuvette (10 mm path length). All microscopy measurements were made using Image J software.

2.4.2 Synthesis

2.4.2.1 Peptide Synthesis

The peptides used in this work were synthesized via established microwave assisted solid phase peptide synthesis protocol. In summary, 138.8 mg (0.25 mmol) of Fmoc-Phe-Novasyn® TGA resin (Millipore catalogue number: 8560340001) was swelled in N,N-dimethylformamide (DMF) for 15 minutes. The Fmoc-Phe-Novasyn® TGA resin was deprotected by adding 2 mL of 20% 4-methylpiperidine in DMF to the resin, then heating the mixture to 75 °C in 1 minute and maintaining that temperature for an additional 2 minutes. A filtration manifold was used to drain excess reagent, and the resin was then washed with (5 mL x 3) of DMF. For the coupling step, 0.1 M solution of HCTU in NMP (5 eq., 1.25 mL) and DIEA (7 eq., 0.175 mmol, 30.4 µL) were added to Fmoc-protected amino acid (4 eq., 0.125 mmol). The solution was then thoroughly vortexed and centrifuged to dissolve the amino acid. The resulting solution was added to the washed resin, and the mixture was heated to 75 °C over the course of 1 minute and held at that temperature for 5 minutes. After the coupling step, the excess reagent was drained and the resin

was washed with (5 mL x 3) of DMF. This cycle was then repeated for every amino acid. Double coupling of proline and adjacent amino acids was used to ensure the complete reaction of the secondary amide group. For divalent peptide conjugates, the N-terminus was completed by a 5-azido pentanoic acid cap using the same coupling steps described above. For the monovalent peptide conjugates, the final amino acid was deprotected to yield an N-terminus amino group using previously described deprotection protocol. To produce peptides with the oxidized methionine residue, N₂-PEP_{Au} was dissolved in a 1:1 solution of NanoPure water and acetonitrile. Concentrated hydrogen peroxide (H₂O₂) solution was added until the final H₂O₂ concentration was 100 mM. This solution was left undisturbed overnight and the resulting oxidized product was purified via HPLC.

2.4.2.2 Peptide Conjugate Synthesis

The divalent peptide conjugate was synthesized using established protocols.^{19,20} C₁₄-dialkyne was attached to each azido peptide sequence via Cu-catalyzed click chemistry described previously.^{61,84} The monovalent peptide conjugate was synthesized by following previously reported protocols: coupling succinimide-activated decanoic acid (C₁₀-NHS) to the free N-terminus of the peptide sequence.⁴⁹

2.4.3 Assembly Conditions

2.4.3.1 Peptide Conjugate Assembly

To the lyophilized peptide conjugate (18.725 nmol for single helical peptide conjugates and 74.9 nmol for double helical peptide conjugates) 250 μ L of 0.1 M HEPES buffer was added. The solution was sonicated for 5 minutes, then left undisturbed at room temperature for approximately 16 hours before TEM sample preparation.

2.4.3.2 Au NP Single Helices Assembly

18.725 nmol of $C_{14}-(PEP_{Au}^{M-ox})_2^X$, (X= S, T, and F) was dissolved in 250 μ L of 0.1 M HEPES buffer, sonicated for 5 minutes and then left undisturbed for 25 minutes. Next, 2 μ L of 1:1 mixture of aqueous 0.1 M HAuCl₄ in 1 M TEAA buffer was added to the peptide conjugate solution. Approximately 2-3 seconds after addition of gold precursor solution, a black precipitate appeared. The vial was vortexed immediately after appearance of the precipitate.

2.4.3.3 Au NP Double Helices Assembly

74.9 nmol of $C_{10}-PEP_{Au}^X$, (X= S, T, and F) was dissolved in 250 μ L of 0.1 M HEPES buffer and allowed to sit undisturbed for 30 minutes. A solution of 0.1 M HAuCl₄ in 0.1 M TEAA buffer was prepared and allowed to sit for 10 minutes, then a 100 μ L aliquot was transferred to a new vial and centrifuged for 10 minutes at 10 rpm. 2 μ L of this solution was added to the peptide conjugate solution. Upon appearance of a black precipitate, the vial was immediately vortexed.

2.4.4 Characterization and Sample Preparation

2.4.4.1 Circular Dichroism Spectroscopy

CD measurements were collected with Olis DSM 17 CD spectrometer with a quartz cuvette (0.1 cm path length) at 25 °C with 8 nm/min scan rate. Solutions in 10 mM HEPES buffer for C_{14} -(PEP_{Au}^{Mox})₂^X (75 μM) or C_{10} -PEP_{Au}^X (300 μM) were prepared for each CD measurement.

2.4.4.2 Attenuated Total Reflectance Fourier Transform Infrared Spectroscopy

ATR-FTIR measurements were collected with a PerkinElmer Spectrum 100 FTIR instrument equipped with an ATR accessory and recorded with PerkinElmer Spectrum Express software. C_{14} -(PEP_{Au}^{Mox})₂^X (75 μM) or C_{10} -PEP_{Au}^X (300 μM) in 0.1 M HEPES buffer was prepared and left undisturbed on the bench top for ~24 h. The solution was then dialyzed against NanoPure water using d-tube dialyzers (Millipore catalog number: 71505-3). After dialysis, the peptide conjugate solution was concentrated via evaporation and was drop cast onto the ATR substrate prior to data collection.

2.4.4.3 Atomic Force Microscopy

AFM measurements were collected in tapping mode using the Asylum MFP-3D atomic force microscope and ultrasharp AFM tips (NanoandMore SHR-150). 0.1% APTES (3-aminopropyl-triethoxy-silane) solution was drop casted onto a freshly cut mica surface, then the surface was rinsed with NanoPure water. 50 μL of C_{14} -(PEP_{Au}^{Mox})₂^X (75 μM) or C_{10} -PEP_{Au}^X

(300 μM) in 0.1 M HEPES was then drop cast and rinsed with water after 1 minute and allowed to dry in the desiccator overnight.

2.4.4.4 Transmission Electron Microscopy

TEM was conducted on a FEI Morgagni 268 operated at 80 kV and equipped with an AMT side mount CCD camera system. 6 μL of $\text{C}_{14}\text{-(PEP}_{\text{Au}}^{\text{Mox}})_2^{\text{X}}$ (75 μM) or $\text{C}_{10}\text{-PEP}_{\text{Au}}^{\text{X}}$ (300 μM) in 0.1 M HEPES was drop casted onto a 3 mm-diameter copper grid with formvar coating. After 5 minutes, excess solution was wicked away and the grid air-dried for 2 minutes. For studying peptide conjugate assembly, 6 μL of phosphotungtic acid (pH = 7) was drop cast onto the grid and allowed to sit for 30 seconds. For studying NP assemblies, 6 μL of NanoPure water was drop cast onto the grid and allowed to sit for 30 seconds. Excess solution was wicked away and the grid was air-dried for 5 minutes.

3.0 Single Amino Acid Modifications for Controlling the Helicity of Peptide-Based Chiral Gold Nanoparticle Superstructures

This work is completed with collaboration with Ruitao Jin, Victoria Zerbach, Yuyu Zhang, Tiffany R. Walsh, and Nathaniel L. Rosi. The manuscript is accepted for publication in JACS. The supporting information is found in Appendix C.

3.1 Introduction

The compositions and structures of molecules are the foundation of complexity and diversity. This is particularly apparent in biology, where small differences in nucleic acid sequence (genotype), can dramatically influence observable characteristics (phenotype). Equally striking is how the inversion of a single chiral center within a small molecule can result in different properties and functions. Harnessing the precision of molecular structure and translating it across length scales to the ‘nano’ regime can enable molecular-level coding of nanoscale structure and properties and nano-architecting approaches that rely on well-established methods for finely controlling molecular structure.⁹⁵⁻⁹⁷

We and others investigate how peptides can be used as programmable molecular species for controlling the synthesis and structure of metal nanoparticles (NPs)^{36,38,43,88,98} as well as their assembly into well-defined NP superstructures.^{32,49,77,99} Short peptide (~8-12 amino acids) NP capping ligands, comprising both natural and non-natural amino acids, provide a vast sequence space that can be leveraged to control NP size, shape, and properties. In our own work, we use amphiphilic peptide conjugate molecules to assemble Au NP superstructures.^{49,58,61} We have developed robust peptide conjugate assembly models that serve as the foundation for building connections between the molecular composition, structure, and properties of NP superstructures.^{42,71,84,86} In general, the peptide conjugates contain a hydrophobic organic tail appended to the N-terminus of one or more Au-binding peptides (AYSSGAPPMPFF; initially reported as A3,³⁸ herein referred to as PEP_{Au}). In the context of Au NP assemblies, these conjugates contain both an assembly module and a NP binding module (Figure 3-1).

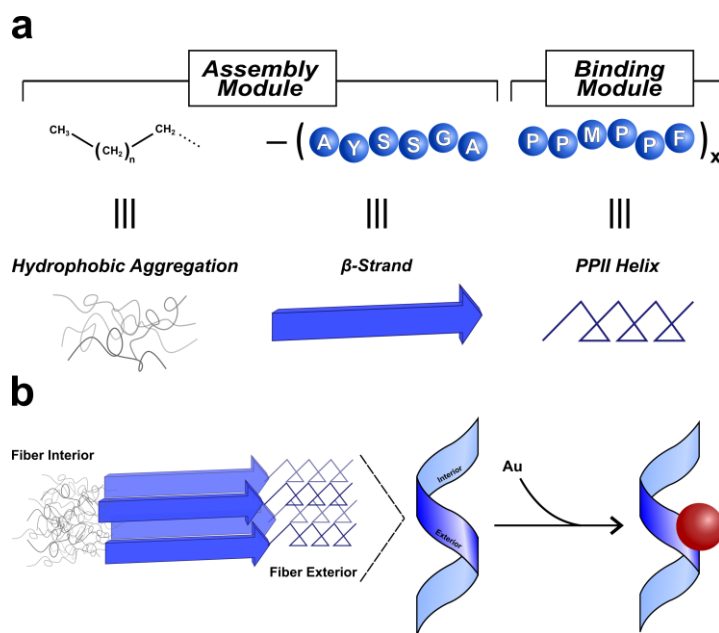


Figure 3-1. (a) Illustration of the different ‘modules’ within the peptide conjugate: the assembly module contains the hydrophobic tail and β -strands at the peptide N-terminus; the C-terminus is the NP binding module and adopts PPII secondary structure. (b) Peptide conjugates can assemble into 1-D helical fibers with the NP binding module exposed to the aqueous environment and the assembly module sequestered in the interior of the fiber.

The assembly module (Figure 3-1a) consists of the N-terminal amino acids (AYSSGA) and the hydrophobic organic tail; a combination of parallel β -sheet secondary structure formation and hydrophobic aggregation promotes assembly in aqueous media (Figure 3-1b). The C-terminus (PPMPPF) is the NP-binding module (Figure 3-1a). Together, the composition of these modules is a molecular code that we can manipulate to design and program diverse collections of NP superstructures (Figure 3-1b). Substantial variation of the code can result in entirely different structural outcomes. For example, $\text{C}_6\text{-A}_2\text{-PEP}_{\text{Au}}$ directs assembly of spherical NP superstructures^{58,100} while $\text{C}_{12}\text{-PEP}_{\text{Au}}$ yields Au NP double helices.⁴⁹ Fine-tuning the assembly architecture can be accomplished by making more subtle changes: adjusting the aliphatic tail

length by 2 methylene units enables incremental tuning of helical pitch,^{61,86} use of either *L* or *D* amino acids yields for left- or right-handed NP helices, respectively,⁶² and altering the sequence of amino acids in the NP binding module allows control over NP dimensions.⁴² Accompanying each of these molecularly-programmed structural modifications are measurable differences in collective plasmonic properties.^{42,62,86}

At an even finer level, we found that atomic-level changes to the NP-binding module can also influence superstructure morphology. In 2015, we reported a family of divalent peptide conjugates ($C_x-(PEP_{Au})_2$, $x = 16-18$) that direct the formation of double-helical Au NP assemblies.⁶¹ Later, we discovered that these conjugates yield single-helical superstructures with oblong NPs when their methionine residues are oxidized from the thioether to the sulfoxide (*i.e.*, $C_x-(PEP_{Au}^{M-ox})_2$).⁸⁴ The dramatic shift in structure upon oxidation of the methionine residues led to a strong plasmonic chiroptical response, indicating that small atomic modifications to the peptide conjugate molecular code could trigger significant property changes/enhancement.

Collectively, these observations prompted studies to uncover the origin of this structural phenomenon with the aims of: i) understanding how and why the NP binding module affects NP superstructure morphology; ii) identifying new peptide sequences that would exclusively direct formation of single-helical superstructures; and iii) developing new insights into atomic/molecular factors that could influence the structure and properties of NP superstructures fabricated using our peptide-based methodology.

3.2 Results and Discussion

In a previous study, we determined that methionine oxidation leads to a decrease in the peptide-Au surface contact in the NP binding module.⁴² This decrease in surface contact correlates with a transition from double-helical assemblies of spherical Au NPs to single-helical assemblies of oblong Au NPs. Our results also showed that PEP_{Au} yielded spherical Au NPs whereas PEP_{Au}^{M-ox} yielded larger, nonspherical Au NPs, suggesting that a decrease in surface contact compromises the binding ability of the peptide capping ligand and leads to formation of the oblong Au NPs.⁴² However, that study did not yield any insight into the origin of the transition from double- to single-helical assemblies. Notably, the fibers formed from C₁₆-(PEP_{Au})₂ and C₁₆-(PEP_{Au}^{M-ox})₂ appear similar when imaged with transmission electron microscopy (TEM), and atomic force microscopy (AFM) images suggest both form helical ribbons (Appendix Figure 17). While C₁₆-(PEP_{Au}^{M-ox})₂ fibers appear more tightly coiled than C₁₆-(PEP_{Au})₂ fibers (Appendix Figure 17c, d) the observed difference in NP assembly structure cannot solely be correlated to the observed differences in the fiber morphology, especially because the NP size and shape also change. Based on these observations, we hypothesize that the transition from double to single helices correlates with a decrease in the NP binding module's Au surface contact. Specifically, we postulate that the double-helical superstructures may derive from the binding of two spherical NPs to the face of a helical ribbon fiber template (Figure 3-2). If the NP binding ability of the peptide decreases, particle growth would be less limited, resulting in formation of larger oblong NPs across the face of the helical ribbon. Consequently, the NP superstructure would now be single-helical.

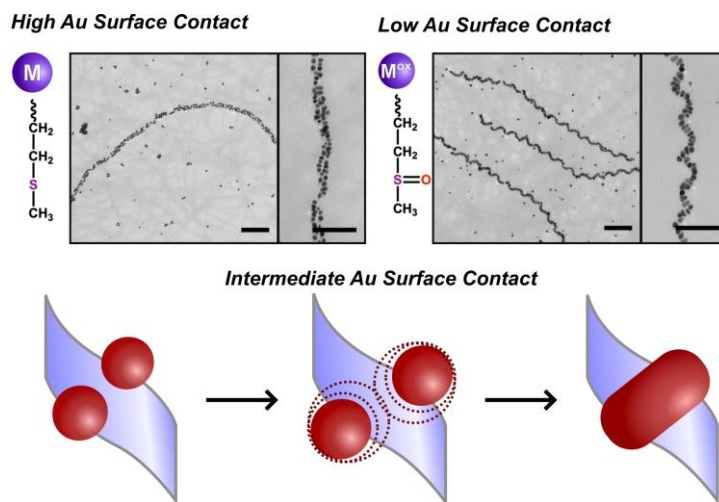


Figure 3-2. Structures formed from high surface contact peptide sequences form double-helical superstructures (top left), while low surface contact sequences yield Au NP single helices (top right). Scale bars 100 nm. Schematic illustration of proposed NP transformation with decreasing peptide-Au surface contact (bottom).

To examine this possibility, we present here a family of divalent peptide conjugates in which we modify the sequence of the NP binding module to control its degree of contact with the Au surface. Studies have identified Y₂, M₉, and F₁₂ as the primary anchoring residues in PEP_{Au}, which allow it to serve as a NP non-covalent capping ligand.¹⁰¹ Based on our fiber assembly model, Y₂ engages in β -sheet formation near the core of the assembled fibers and likely does not play a major role in binding NPs.^{42,61,84} M₉ and F₁₂ are in the particle binding module and play an integral role in anchoring NPs to the fibers. Because M₉ oxidation results in a transition from double to single helices and decreases the NP surface contact of the NP binding module, we synthesized a series of peptide conjugates with different amino acids at the 9th position: C₁₆-(AYSSGAPPXPPF)₂, where X = cysteine C, methionine M, tertbutyl cysteine CtBu, alanine A, serine S, methionine sulfoxide M^{ox}, and tertbutyl cysteine sulfoxide C^{ox}tBu (Figure 3-3, Appendix Figure 15, 16). Sulfur-containing ligands, especially thiol functional groups, have

strong associations with Au NPs on the level of covalent bonds,^{102–104} for the residues containing a sulfur atom, we gradually increased the steric bulk of the adjacent groups to inhibit binding. A and S were included because they have comparatively moderate-weak contact with Au surfaces.⁴⁰ We reasoned that the NP binding affinity would decrease thusly: C > M > CtBu > M^{ox} \cong A \cong S > C^{ox}tBu.

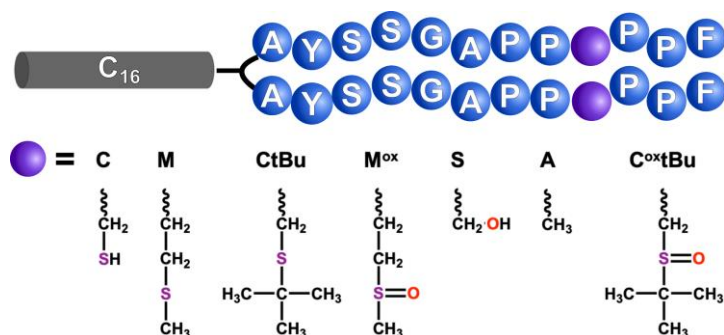


Figure 3-3. Family of amino acid modifications at the peptide 9th position, organized left to right from highest to lowest Au affinity.

Based on our assembly model for this class of peptide conjugates, we predicted that all variants would readily form fibers in aqueous buffer, which was confirmed using TEM imaging (Appendix Figure 18). Fourier transform infrared (FTIR) and circular dichroism (CD) spectroscopy revealed some similarities in the molecular structure of the conjugates within this series of fibers. Each fiber sample displayed an amide I band of similar intensity at $\sim 1630\text{ cm}^{-1}$ in the FTIR spectrum, which is indicative of β -sheet secondary structure.^{49,94} In addition, a sharp symmetric (CH₂) band at $\sim 2850\text{ cm}^{-1}$ was observed for all samples, indicating ordered packing of the aliphatic tails (Appendix Figure 19).^{49,105} The CD spectra across the series were less homogeneous, and each spectrum likely reflects contributions from more than one type of

secondary structure, as we have reported in previous studies of analogous conjugates.^{68,70} The S and A variants display a strong and broad negative feature from ~210-220 nm which is consistent with β -sheet secondary structure (Appendix Figure 20a).^{50,91} In the case of the A variant, a shift in this feature to lower wavelength could be attributed to strong contributions from PPII secondary structure.^{93,106} The C, M, and M^{ox} variants display a negative feature at ~205 nm which can be assigned to PPII secondary structure, and the broadening of this primary peak is likely due to contributions from β -sheet secondary structure (Appendix Figure 20b), which is supported by the FTIR data discussed above. We cannot definitively interpret the CD spectra for the CtBu and C^{ox}tBu variants (Appendix Figure 20c), yet from FTIR data we know that these variants form fibers that have some β -sheet character. The significant steric bulk introduced by the tertbutyl group could significantly disrupt secondary structure formation at the C-terminus, resulting in more ambiguous CD spectra. In summary, we can conclude that all variants exhibit β -sheet secondary structure, while varying the 9th position can affect the C-terminal structure.

Prior to NP assembly experiments, we first verified that discrete Au NPs could be formed using each of the amine-terminated peptide variants as the capping ligand (Appendix Figure 21, Appendix Table 1). We next subjected the family of conjugates to our established Au NP synthesis and single helix assembly conditions.^{42,71,84,86} The C variant was predicted to have the strongest contact with the Au NPs, and it yielded aggregates of spherical NPs bearing some apparent underlying structure which is too irregular to assign (Figure 3-4a, Appendix Figure 22). M was expected to have a lower NP affinity than C, and this variant produced linear

superstructures of spherical NPs with some double-helical character, as we reported previously (Figure 3-4b, Appendix Figure 23).^{61,84} Protecting the cysteine thiol with a tertbutyl group should decrease its Au surface contact significantly, and the NP superstructures formed using the CtBu variant are best described as a blend of double and single helices (Figure 4c, Appendix Figure 24). The M^{ox}, A, and S variants are considered ‘moderate’ Au binders, and each yielded NP single helices composed of oblong NPs (Figure 3-4d-f, Appendix Figure 25-27). Lastly, oxidizing the tertbutyl-protected cysteine residue introduces significant steric bulk at the C-terminus, and while this variant does form fibers in aqueous assembly buffer, the extra bulk apparently inhibits attachment of NP to the fibers (Figure 3-4g, Appendix Figure 28). Across this series from ‘strong binding’ to ‘weak binding’, the aspect ratio of the assembled NP generally increased (Figure 3-4h), and the superstructures transitioned from NP aggregates to double helices and then to single helices; in the case of the C^{ox}tBu variant, the NPs were spherical yet not assembled onto fibers. Accompanying this transition in structure is the appearance of a plasmonic chiroptical signal going from the aggregates to the single-helical assemblies, illustrating how adjustments to molecular structure can lead to emergence of unique collective plasmonic properties (Figure 3-4i). Such properties are relevant to a variety of applications from sensing to optics.^{107,3,108,109,11}

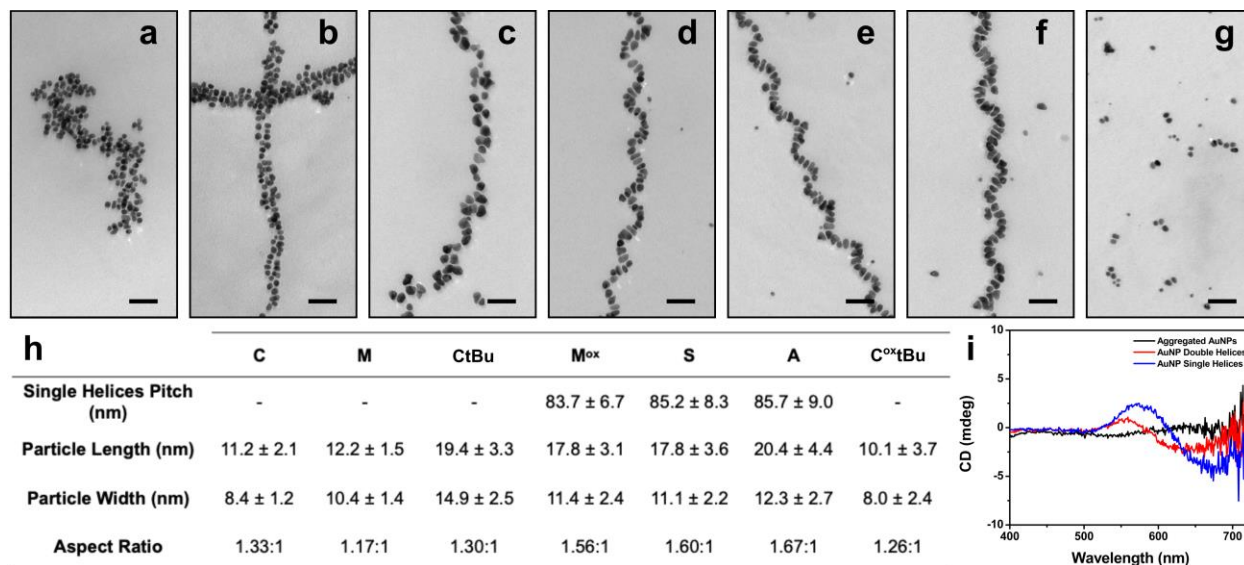


Figure 3-4. (a) Au NP aggregates produced using C_{16} -(AYSSGAPPCPPF)₂; (b) Double-helical superstructures produced using C_{16} -(AYSSGAPPMPPF)₂; (c) C_{16} -(AYSSGAPPCtBuPPF)₂ yields a blend of single- and double-helical assemblies; single helices produced using (d) C_{16} -(AYSSGAPPM^{ox}PPF)₂, (e) C_{16} -(AYSSGAPPSPPF)₂, and (f) C_{16} -(AYSSGAPPAPPF)₂; (g) Discrete Au NPs formed using C_{16} -(AYSSGAPPC^{ox}tBuPPF)₂. Scale bars 50 nm. (h) Table of NP dimensions and helix pitch (where applicable). (i) CD spectra for the three categories of superstructures: aggregated NPs, double helices, and single helices free energy data, along with the resultant binding scores, are provided in the Supporting Information (Tables S3-S6).

Replica exchange with solute tempering molecular dynamics (REST-MD) simulations were used to explore our proposed connection between peptide binding strength and the ability to support either single or double helix assemblies. These simulations predict the likely conformational ensemble of each peptide in the surface-adsorbed state at the aqueous Au interface. Based on these simulation data, the degree of binding between the residues of the PEP_{Au} peptide and its six variants with the aqueous Au interface was evaluated, with particular emphasis on the residues in the C-terminal ‘particle binding’ module. To do this, we computed a

binding score for each residue in each peptide, where the score was defined as the fraction of the trajectory for which each residue was deemed in contact with the Au surface (denoted the contact fraction, expressed as number between 0 and 1) and the Au-binding free energy of the counterpart amino acid for that particular residue. Most of these free energy amino acid data have been published previously but were not available for the amino acid analogues M^{ox}, CtBu and C^{ox}tBu. These new data were generated as part of the current work using umbrella sampling simulations; the full set of contact fraction data and amino acid binding

The binding scores for each residue can be summed over a given range of the peptide sequence to determine a cumulative binding score. As anticipated, the binding score summed over the N-terminal half of the sequence (Figure 3-5a) did not show any correlation with the propensity to form single-, double-, or no-helix assemblies. However, the sum over the C-terminal half (residues 7-12, the particle binding module) revealed a trend in binding score (Figure 3-5a) that was approximately consistent with the experimentally observed propensity to form double-, single- or no-helix-based assemblies. Following the hypothesis proposed in earlier work regarding the contribution of the residue at position 9 in the sequence,^{40,42} the binding score exclusively for the residue at position 9 (Figure 3-5b) was considered, revealing a strong correlation with the structural traits of the associated assembly.

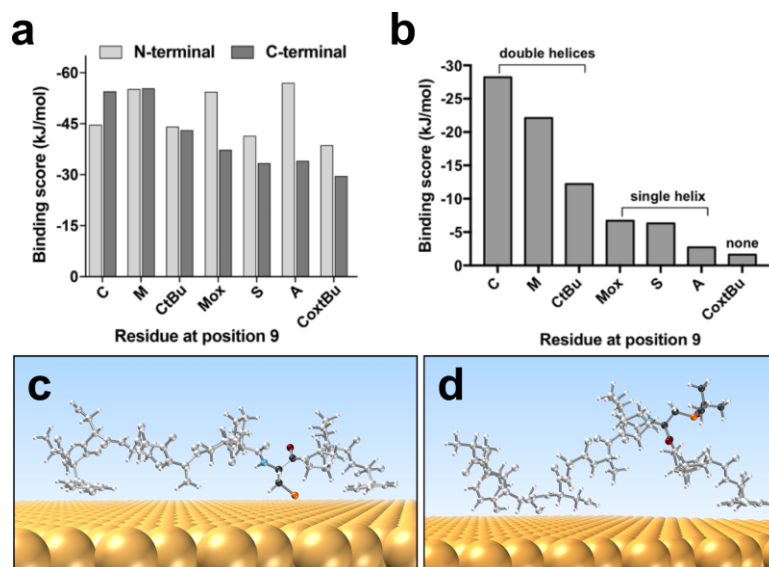


Figure 3-5. Binding scores for the original PEP_{Au} sequence (residue M at position 9) and the six sequence variants. (a) Sum of residue-surface binding scores for the N-terminal half (residues 1-6) and C-terminal half (residues 7-12). (b) Residue-surface binding score for the residue at the ninth position in the sequence. Representative structures of (c) 9C and (d) 9C^{ox}tBu peptides adsorbed on Au(111) surface according to REST-MD simulations, corresponding to highest and lowest binding scores, respectively. C and C^{ox}tBu are highlighted with color: C, dark grey; H, light grey; N, blue; O, dark red; S, orange.

A possible explanation for this clear trend in surface binding strength at position 9 of the sequence as a function of variant can be attributed to the conformational recalcitrance of the C-terminal region of the peptide with respect to variation of the residue at position 9. In other words, each of the variants was found to maintain at least some conformational similarity with respect to the original sequence. To quantify this, the conformational ensemble of each variant adsorbed at the aqueous Au interface was characterized using a clustering analysis. In brief, in this analysis conformations that are sampled by the REST-MD simulation are grouped together (into clusters) on the basis of similarity in the peptide backbone structure. These simulation data

can also be used to determine the most common secondary structure(s) of each peptide in relation to the Au(111) surface. The structures of 9C and 9C^{ox}tBu (highest and lowest scores, respectively) are shown in Figure 3-5c and Figure 3-5d, respectively. The 9th position amino acid is colored for clarity, showing how the cysteine residue of 9C closely associates to the Au(111) surface while C^{ox}tBu is directed away from the surface with no apparent contact (images for the remaining peptide sequences except 9A can be found in Appendix Figure 30-36). The clustering analysis yields the number of clusters and the population of each cluster. Typically, the top five most populated clusters capture the majority of the ensemble. The cluster centroid is the structure that best represents each cluster conformation; on that basis, the cluster centroids were compared for the top five clusters between the original PEP_{Au} peptide and the six variants. This comparison (data in Appendix Figure 40) revealed the structural similarity of each variant with PEP_{Au} in the surface-adsorbed state. These data suggest that the success of the substitution strategy at position 9 is due in part to the fact that variation in the ninth residue does not result in a substantial departure from the surface-bound conformational ensemble of PEP_{Au}.

Previously-published data regarding the binding free energies of amino acids at the aqueous Au interface⁴⁰ suggest a range of residues for substitution at position 9 that might be able to support a residue binding score in the single-helix range (-1 to -10 kJ mol⁻¹): proline, threonine, leucine, aspartic acid, glutamic acid and lysine. A substitution of methionine with a charged residue (*i.e.*, aspartic acid, glutamic acid, or lysine) may produce a strong conformational change of the peptide, thereby potentially disrupting the conformational recalcitrance proposed above; proline was excluded due to the abundance of proline already present in the C-terminal half of the sequence. We elected to test the threonine variant (9T)

because it is structurally similar to serine. This variant was computationally modeled using REST-MD simulations. The binding score analysis determined a binding score of -4.5 kJ mol^{-1} for 9T, which falls between the 9A and 9S (Figure 3-5. Binding scores for the original PEP_{Au} sequence (residue M at position 9) and the six sequence variants. (a) Sum of residue-surface binding scores for the N-terminal half (residues 1-6) and C-terminal half (residues 7-12). (b) Residue-surface binding score for the residue at the ninth position in the sequence. Representative structures of (c) 9C and (d) $9\text{C}^{\text{ox}}\text{tBu}$ peptides adsorbed on Au(111) surface according to REST-MD simulations, corresponding to highest and lowest binding scores, respectively. C and $\text{C}^{\text{ox}}\text{tBu}$ are highlighted with color: C, dark grey; H, light grey; N, blue; O, dark red; S, orange. b). Based on this evidence, we prepared the 9T variant (Appendix Figure 37, 38) and conducted Au NP synthesis and assembly experiments. In line with our prediction, it yielded well-defined single helices (Figure 3-6, Appendix Figure 39).

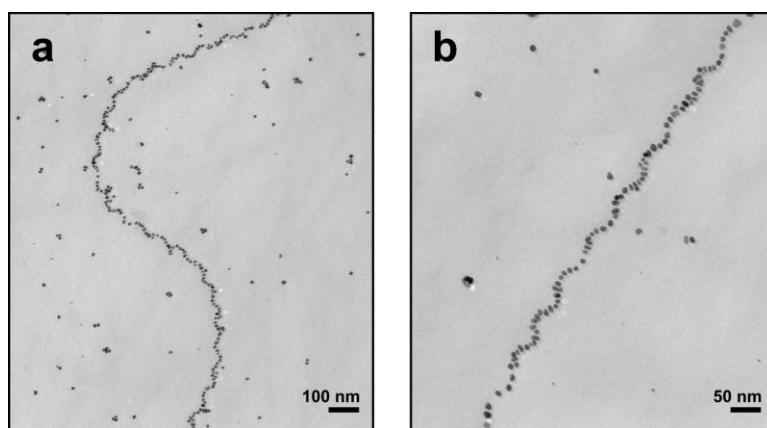


Figure 3-6. Single helices produced using $\text{C}_{16}\text{-(AYSSGAPPTPPF)}_2$.

3.3 Conclusions

Variation of the 9th amino acid within the Au NP binding module of C₁₆-(PEP_{Au})₂ yielded a family of peptide conjugates with differential Au NP binding affinities which were used to prepare a series of NP assemblies that represent snapshots of the transition from double- to single-helical Au NP superstructures. Our experimental observations coupled with simulations that predict a ‘binding score’ for each peptide variant provide compelling evidence that relative Au NP binding affinity of the peptides significantly influences the helical morphology of the superstructure and governs the double- to single-helical structural transformation. Accompanying this structural transition is the emergence of observable plasmonic chiroptical behavior for the single helices. These results and insights demonstrate that single amino acid modifications to the NP binding module of the PEP_{Au} sequence can result in dramatic changes to the structure and properties of helical NP assemblies. A significant implication of these results is that molecular chemistry can be advantageously used to precisely control the nano- and micro-scale structure and collective properties of NP superstructures.

3.4 Experimental Methods

3.4.1 General Methods and Materials

All chemicals were purchased from commercial sources and used without further purification. Peptides were synthesized using established microwave-assisted solid-phase peptide

synthesis procedures using a CEM Mars microwave. For all aqueous solutions, NanoPure water (18.1 m Ω) from a Barnstead Diamond purification system was used. The peptides and peptide conjugates were purified using reverse phase high-performance liquid chromatography (HPLC) on an Agilent 1200 liquid chromatographic system equipped with diode array, multiple-wavelength detectors, and a Zorbax-300SB C₁₈ column. Peptide and peptide conjugate masses were determined using liquid chromatography mass spectrometry (LC-MS) on a Shimadzu LC-MS 2020 instrument. Ultraviolet-visible (UV-vis) spectra were collected using an Agilent 8453 UV-vis spectrometer with a quartz cuvette (10 mm path length).

3.4.2 Synthesis

3.4.2.1 Peptide Synthesis

All peptides were synthesized using established microwave-assisted solid-phase peptide synthesis protocols. Briefly, 138.8 mg (0.25 mmol) of Fmoc-Phe-Novasyn TGA resin (Millipore catalog no. 8560340001) was transferred to a filtration manifold and swelled in N,N'-dimethylformamide (DMF) for about 30 minutes. To remove the Fmoc protecting group from the resin, 2 mL of 20% 4-methylpiperidine in DMF solution was added, and the vessel was microwaved with agitation. The deprotection method on the microwave consisted of a one minute temperature ramp to 75 °C, followed by a 2 minute hold. The deprotection solution was removed by filtration and the resin was rinsed with approximately 3 mL DMF for 30 seconds (3X). The solid Fmoc-protected amino acids (4 equiv, 0.125 mmol) were activated in a 0.1 M solution of O-(1H-6-Chlorobenzotriazole-1-yl)-1,1,3,3-tetramethyluronium hexafluorophosphate

(HCTU) in 1-methyl-2-pyrrolidinone (NMP) (5 equiv, 1.25 mL) and N,N-diisopropylethylamine (DIEA) (7 equiv, 0.175 mmol, 30.4 μ L); they were vortexed to dissolve and then allowed to sit on the benchtop for at least 5 minutes. The activated amino acid solution was added to the resin vessel and microwaved with agitation using the following coupling method: 1 minute temperature ramp to 75 °C followed by a 5 minute hold. The excess solution was drained, and the resin was again washed with DMF. This procedure was repeated for each subsequent amino acid. Every proline and proline-adjacent amino acid was double-coupled (*i.e.*, coupling steps of two equivalents per amino acid were performed in sequence). The final step was either a deprotection to produce amine-terminated peptides, or deprotection and coupling of a 5-azido pentanoic acid cap, using the previously described coupling protocol.^{61,84} The completed sequence was cleaved from the resin with a mixture of 90% trifluoroacetic acid, 5% diisopropylsilane, and 5% NanoPure water. The product peptide was isolated by precipitation with cold diethyl ether, then lyophilized and purified via HPLC. For the sequences that contained an oxidized residue (M^{ox} and $C^{ox}tBu$), the lyophilized peptide was dissolved in 1 mL 1:1 acetonitrile (ACN) and NanoPure water with 8 μ L of 50% hydrogen peroxide in NanoPure water. The solution was left undisturbed on the benchtop overnight, then the oxidized peptide was collected via HPLC.

3.4.2.2 Peptide Conjugate Synthesis

The azide-terminated peptides were coupled to C_{14} -dialkyne using established protocols described previously.^{61,84}

3.4.3 Assembly Protocols

All assembly experiments were performed at room temperature.

3.4.3.1 Peptide Conjugate Assembly

The lyophilized peptide conjugate (18.725 nmol) was dissolved in 250 μL of 0.1 M HEPES buffer. The solution was sonicated for 5 minutes, then 2.5 μL of 0.1 M calcium chloride (CaCl_2) was added to promote fiber assembly.

3.4.3.2 NP Superstructure Assembly

Lyophilized peptide conjugate (18.725 nmol) was dissolved in 250 μL of 0.1 M HEPES buffer. The solution was sonicated for 5 minutes, then 2.5 μL of 0.1 M calcium chloride (CaCl_2) was added and the solution was incubated on the benchtop for 25 minutes. Next, 2 μL of a 1:1 mixture of 0.1 M chloroauric acid (HAuCl_4) in NanoPure water and 0.1 M triethylammonium buffer was added to the solution. When a black precipitate was observed, the solution was vortexed until the precipitate dissolved. The solution was incubated on the benchtop for ~16 hours to allow for complete superstructure growth.

3.4.4 Characterization and Sample Preparation

3.4.4.1 Atomic Force Microscopy (AFM)

AFM images were collected on a Veeco MultiMode AFM with NanoScope V Controller in tapping mode. 0.1% APTES (3-aminopropyl-triethoxy-silane) solution was drop casted onto a freshly cut mica surface, rinsed with NanoPure water and allowed to dry in a desiccator overnight. 50 μL of peptide conjugate in 0.1 M HEPES (75 μM) was then drop cast and rinsed with water after 10 min and allowed to dry.

3.4.4.2 Circular Dichroism (CD) Spectroscopy

Lyophilized peptide conjugate (18.725 nmol) was dissolved in 250 μL of 0.01 M HEPES buffer with 2.5 μL CaCl_2 and allowed to incubate overnight. CD measurements were collected using an Olis DSM 17 CD spectrometer with a quartz cuvette (0.1 cm path length) at 25 $^\circ\text{C}$ with a scan rate of 8 nm/min. For CD spectra of the Au NP assemblies, structures were prepared according to synthetic protocol and spectra were collected using the same instrument settings.

3.4.4.3 Attenuated Total Reflectance Fourier Transform Infrared Spectroscopy (ATR-FTIR)

Spectra were recorded on a PerkinElmer Spectrum 100 FTIR instrument equipped with an ATR accessory using PerkinElmer Spectrum Express software. Lyophilized peptide conjugate (18.725 nmol) was dissolved in 250 μL of 0.1 M HEPES buffer with 2.5 μL CaCl_2 and incubated at room temperature overnight. 175 μL of the solution was dialyzed against NanoPure water

using d-tube dialyzers (Millipore catalog no. 71505-3) and then concentrated by evaporation. 1 μ L of the concentrated solution was drop-cast onto the ATR surface and allowed to dry before spectra were recorded.

3.4.4.4 Transmission Electron Microscopy (TEM)

Low magnification TEM images were collected on a FEI Morgagni 268 instrument operated at 80 kV and equipped with an AMT side mount CCD camera system and high magnification TEM images were collected on Hitachi H-9500 microscope operating at 100 kV (for peptide conjugate fibers) or 300 kV (for Au NP assemblies). TEM samples were prepared on a 3 mm-diameter copper grid with Formvar coating according to the previously described protocol.^{61,84} Images were analyzed using ImageJ software.

3.4.5 Molecular Simulations

3.4.5.1 Replica Exchange with Solute Tempering Molecular Dynamics (REST-MD)

Simulations

All simulations were performed using GROMACS software package (version 2021).¹¹⁰ The simulation system comprised one Au(111) slab placed in an orthorhombic periodic simulation cell of dimensions 5.8 nm \times 6.1 nm \times 6.8 nm, with the z-axis perpendicular to the Au(111) plane. All simulations were performed in the Canonical (*NVT*) ensemble at 300 K, using the Nose-Hoover thermostat.^{111,112} The CHARMM22* force field^{113,114} was used to provide parameters for the peptides, the modified TIP3P model¹¹⁵ was used for water, and the GolP-

CHARMM force-field¹⁰ used for the Au-peptide interactions. Full details are provided in Appendix B.

REST-MD simulations for each of the six peptides ($\text{PEP}_{\text{Au}}^{\text{A},9}$, $\text{PEP}_{\text{Au}}^{\text{S},9}$, $\text{PEP}_{\text{Au}}^{\text{C},9}$, $\text{PEP}_{\text{Au}}^{\text{T},9}$, $\text{PEP}_{\text{Au}}^{\text{C(tBu),9}}$, $\text{PEP}_{\text{Au}}^{\text{Cox(tBu),9}}$) were run in the adsorbed state at the aqueous Au(111) interface. Sixteen replicas were used with the ‘effective temperature’ window of 300-430 K with Terakawa implementation.¹¹⁶ Before production REST-MD simulation, the sixteen initial configurations were energy minimized and then equilibrated at their target potential for 0.5 ns, with no exchange moves attempted during this period. REST-MD trajectories were of 15 ns duration (amounting to $16 \times 15 \text{ ns} = 0.24 \mu\text{s}$ of nominal total simulation time). The initial peptide backbone structures of the 16 replicas were taken from our previous run.⁴² The 16 values of lambda used to scale our force-field were: $\lambda_i = 0.000, 0.057, 0.114, 0.177, 0.240, 0.310, 0.382, 0.458, 0.528, 0.597, 0.692, 0.750, 0.803, 0.855, 0.930, 1.000$.

3.4.5.2 Clustering Analysis

Clustering of all 15001 frames of each REST-MD simulation was performed over all backbone atoms using the Daura algorithm¹¹⁷ using the gmx-cluster utility with cut-off of 2.0 Å in the root mean squared deviation (RMSD) of backbone atomic positions. Cross-cluster similarity was evaluated based on the RMSD of the backbone atoms of the relevant cluster centroid structures. A matched pair of clusters had a RMSD value 2.0 Å or less and a near matched pair had a RMSD less than 2.5 Å.

3.4.5.3 Residue contact analysis

To quantify the residue-surface contact for each residue in each peptide as predicted from the REST-MD simulations, the distance between the topmost Au layer and each residue was calculated. The residue was considered as in contact with Au surface if the measured distance is equal to or less than the cut-off values which have been published elsewhere,¹⁰¹ along with the corresponding reference site for each residue. For non-standard residues, we used the sulfur atom as the reference site and a cut-off value of 4.5 Å for determining the surface contact. The summary of reference sites and cut-off values is provided in Appendix Table 2.

3.4.5.4 Steered MD and umbrella sampling calculations

The umbrella sampling approach was used to evaluate the potential of mean force profiles for the amino acid analogues of the M^{ox}, CtBu and C^{ox}tBu residues, binding at the aqueous Au(111) interface. The amino acid binding energy profiles were calculated using a methodology similar to that published previously.¹¹⁸ Both the N- and C-termini of the amino acids were capped. Steered pulling simulations were conducted to obtain configurations as a function of vertical distance from the surface in the z-direction. These were done with a constant speed, with a harmonic force constant for the steered MD (and for the subsequent umbrella sampling simulations) was 3000 kJ mol⁻¹ nm⁻², with a pulling rate of 0.05 nm ns⁻¹. The spatial interval between adjacent umbrella sampling windows was 0.05 nm along the z-axis, and each umbrella sampling window was centered at each value of the reaction coordinate. For each window, an *NVT* simulation under the applied force constant was run for 100 ns. The resultant

PMF profiles with estimated errors were obtained using the WHAM using “traj” bootstrapping method with 200 bootstraps and a default tolerance of 10^{-6} in gmx-wham program.¹¹⁹

4.0 Cooperative Assembly of Nanoparticle Superstructures through Designed Electrostatic Interactions

This work is completed with collaboration with Victoria Zerbach and Nathaniel L. Rosi. A manuscript is in the final stages of preparation.

4.1 Introduction

The organized assembly of components into a more complex structure is essential to every level of biological function: phospholipids assemble into cell membranes, differentiated cells assemble into organs, organ systems form organisms. The structure of the assembly is precisely controlled by the makeup of its components, and this structure also determines function. Monomeric peptides composed of sequences of amino acids can be programmed to self-assemble into functional proteins—this hierarchy of structures is controlled by inter- and intra-molecular forces like hydrophobic interaction and electrostatic repulsion or attraction.^{120,121} In the synthetic space, researchers can use the same forces of interaction to assemble precisely designed structures.^{9,122,123} A particularly successful assembly strategy employs peptide amphiphiles, a class of molecules that consist of a short peptide sequence covalently attached to a hydrophobic molecule.^{28,49,84} In aqueous media, self-assembly is driven through hydrophobic aggregation of the tail region and favorable solution interactions with the polar or charged amino acids of the head region. This design strategy alone has produced a wide variety of peptide-based nanostructures,^{122,124–127} and these molecules can also be incorporated into hybrid materials.<sup>128–
¹³⁰</sup> Peptides and single amino acids can have an affinity for inorganic materials and promote the formation of crystalline structures, similar to biomineralization processes.^{28,38,88,40} Additionally, the hydrophobic tail can serve more than just one purpose: for example, including a photoactive moiety such as azobenzene can produce a light-responsive nanomaterial.¹³¹

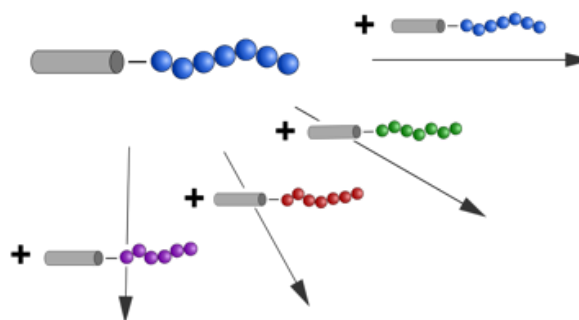


Figure 4-1. Introducing multiple components increases potential structures and functions.

The Rosi lab has developed a nanoparticle assembly strategy based on peptide amphiphiles, specifically the peptide sequence AYSSGAPPMPF (PEP_{Au} or A3³⁸) attached to an aliphatic or aromatic tail. As discussed in the previous chapters, there are two modules: an assembly module in which the hydrophobic tail and β -sheet forming N-terminus amino acids drive aggregation/fibril formation, and a particle binding module at the peptide C-terminus anchors Au NPs to the fiber.^{61,84} The basic structure of the modules contained many opportunities for investigation and a body of work has been developed exploring the tunability of the respective modules and their effect on the superstructure. Modified conjugates have been used to produce Au NP double helices,⁴⁹ hollow spheres with tunable diameter,⁶⁰ and single helices with tunable pitch length and particle size.^{42,70,71,84} To date, all published structures are single-component, and the work is restricted by the limits of maintaining the peptide conjugates' balance of assembly and particle binding propensity. The research presented here demonstrates the co-assembly of structurally and functionally different conjugates to produce unique superstructures (Figure 4-1). Instead of a single conjugate designed to have optimal Au NP

binding affinity and assembly propensity and fiber structure, variants chosen for a specific property or function could be mixed.

To increase complexity and functionality we explored co-assembly between peptide conjugates by leveraging electrostatic interactions, a well-established strategy in peptide amphiphile assembly.^{132,133,124,9} While the Au NP binding affinities can be computationally estimated for individual conjugate variants, interactions between the amino acid side chains affected the fiber structure and Au NP binding to yield new and unexpected structures. Notably, we were able to synthesize organized Au NP superstructures from mixtures of conjugates which, individually, did not yield structures. This strategy allows for greater flexibility in the assembly system, potentially unlocking new static and dynamic NP assemblies through incorporation of multiple different peptide conjugate molecules that each serve a different purpose.

4.2 Results and Discussion

This work focuses on a family of peptide conjugates that produce Au NP single helices, consisting of two identical PEP_{Au} sequences attached to a 16-22 carbon aliphatic tail and referred to as C₁₆₋₂₂-(PEP_{Au})₂.^{70,84} Previously, we have shown that the length of the aliphatic tail affects pitch length,⁷⁰ the sequence of amino acids in the assembly module effect fiber and superstructure formation,⁷¹ and the sequence of the particle binding module controls Au NP contact and therefore NP shape, size, and arrangement.⁴² When studying the binding module in the work discussed in Chapter 3, we chose amino acid modifications that were predicted to alter

the gold-binding affinity without significantly altering the fiber morphology. This work also revealed a unique feature of the peptide C-terminus sequence: due to the multiple proline residues, the modifications at the ninth position did not dramatically alter the peptide secondary structure, allowing for substitutions to be made without significant changes to the underlying fiber structure. Computationally we were able to correlate the superstructure to the peptide 'binding score' determining a mid-range binding score was optimal for single helix formation. A binding score could be calculated for any peptide sequence, so we were able to select new sequences that would most likely form single helices. One of the potential sequences identified computationally contained a glutamic acid (E) residue at the C-terminus (Figure 4-2a). At neutral pH, this acidic amino acid would be deprotonated, increasing the peptides' negative net charge. However, C₁₈-(AYSSGAPPEPPF)₂, abbreviated as C₁₈-(PEP_{Au}^{E,9})₂ (Appendix Figure 41), did not readily assemble into fibers in aqueous solution and produced irregular aggregated Au NPs mixed with discrete particles (Figure 4-2b, c).

In order to learn more about this unexpected peptide conjugate assembly, we used fluorescence spectroscopy to visualize the fiber assembly path and circular dichroism (CD) spectroscopy to investigate the peptide secondary structure. Thioflavin T (ThT) is a dye molecule that binds to β -sheets; when ThT molecules are immobilized between sheets, a strong fluorescence is observed.¹³⁴ Fluorescence associated with ThT dye and β -sheet interactions was observed for C₁₈-(PEP_{Au}^{E,9})₂, but the signal was minimal (Figure 4-2d). The CD spectra was in agreement, as the dominant peak associated with secondary structure formation was low intensity and centered around 205 nm, indicating a random coil configuration (Figure 4-2d).^{50,70,84,88,91,93} When the fiber morphology was imaged using atomic force microscopy (AFM) the few fibers

detected were roughly helical ribbons (Figure 4-2b). From these data, we conclude that the electrostatic repulsion between the charged side chains inhibits β -sheet formation and hydrophobic aggregation, preventing the formation fibers and therefore Au NP single helices. This was confirmed in the NP assembly studies, where discrete Au NPs and small aggregates were the main product.

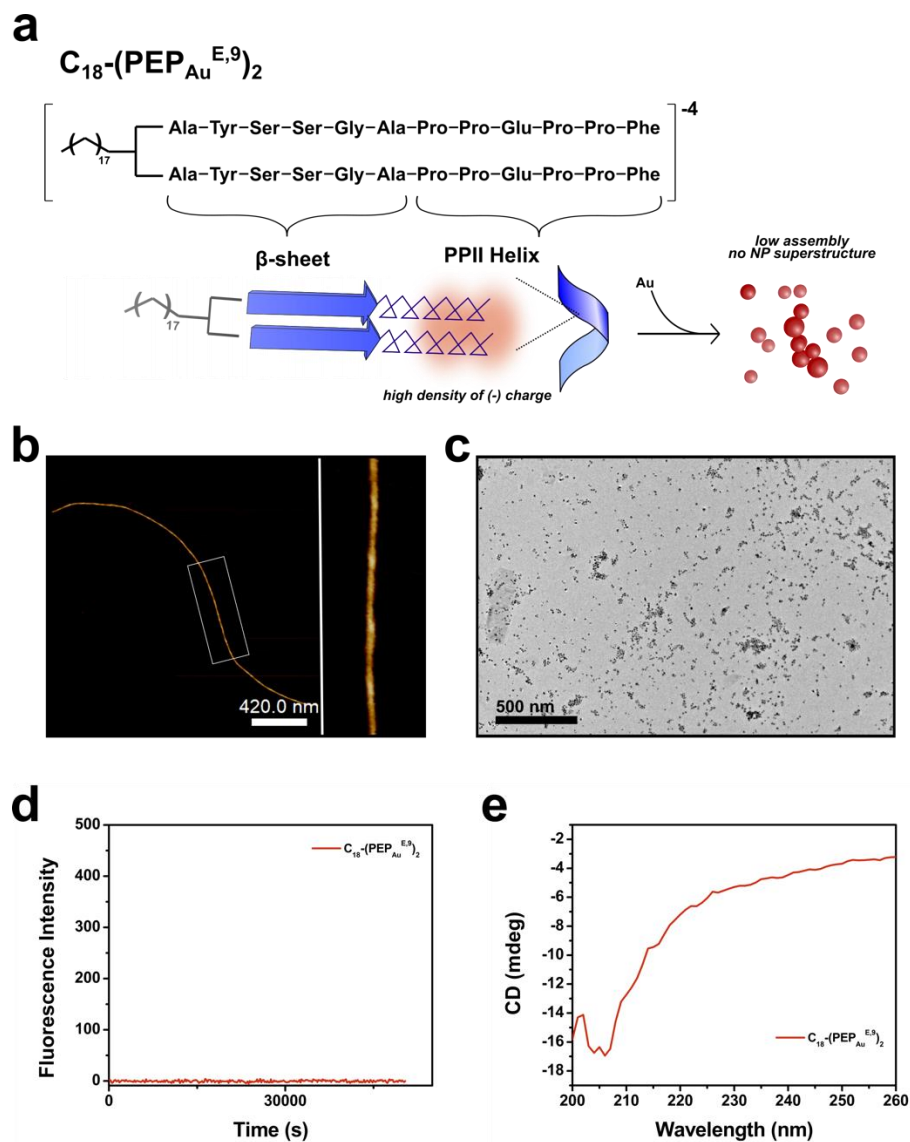


Figure 4-2. (a) Amino acid sequence and proposed assembly model of $C_{18}-(PEP_{Au^{E,9}})_2$. (b) AFM of fibers and (c) discrete/aggregated Au NPs produced with $C_{18}-(PEP_{Au^{E,9}})_2$. (d) Fluorescence kinetics spectrum from 0-14 hours and (e) CD spectrum of $C_{18}-(PEP_{Au^{E,9}})_2$.

Thus, we had found the limit of our binding score analysis; however, an opportunity that arises from these results as well. We predicted that while electrostatic repulsion was working against helix formation in this example, electrostatic attraction could add a new dimension and

functionality to the assembly system. To study cooperative assembly in a family of C_{18} -(PEP_{Au})₂ conjugates, we synthesized three new conjugates with 9th position amino acid substitutions selected to have increasing electrostatic attraction to the negative glutamate residue. The variants contained glycine (G), asparagine (N), or lysine (K) substitutions (C_{18} -(PEP_{Au}^{X,9})₂ where X = G, N, K) (Figure 4-3, Appendix Figure 42, Appendix Figure 43). When mixed with C_{18} -(PEP_{Au}^{E,9})₂, we predicted we would observe an increase in electrostatically-driven cooperative assembly across the series from C_{18} -(PEP_{Au}^{G,9})₂ to C_{18} -(PEP_{Au}^{K,9})₂. Additionally, depending on the critical aggregation concentration of each conjugate, there could be a positive assembly effect due to simply increasing the concentration of like species.

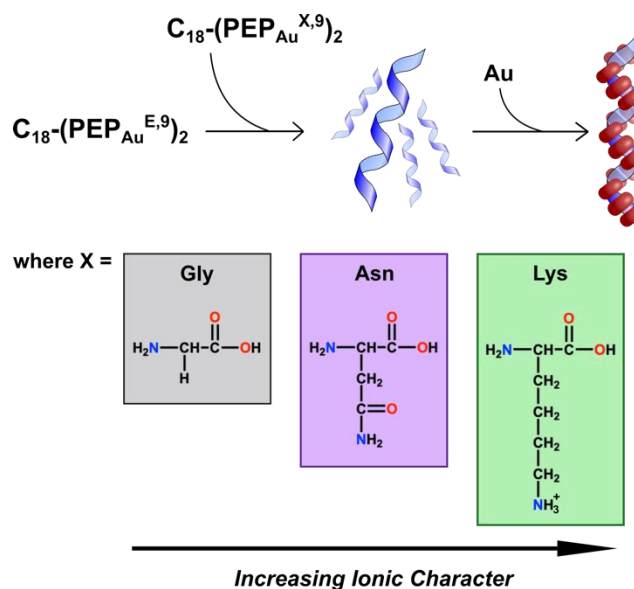


Figure 4-3. Inducing cooperative assembly by mixing precisely designed conjugates.

To begin, we studied the single component assembly of the variants at their *individual* concentrations within the mixtures (37.5 nM or 0.5X, so the two-component co-assembly studies had a total peptide conjugate concentration of 75 nM or 1X). The concentration of the peptide

conjugates can affect the fiber formation if it is below the critical aggregation concentration of any of the conjugates, which would in turn effect the Au NP superstructures. Based on our binding score analysis, $C_{18}-(PEP_{Au}^{G,9})_2$ and $C_{18}-(PEP_{Au}^{K,9})_2$ were predicted to form single helices while $C_{18}-(PEP_{Au}^{N,9})_2$ would not. When subjected to soft assembly conditions at 0.5X concentration, $C_{18}-(PEP_{Au}^{G,9})_2$ and $C_{18}-(PEP_{Au}^{N,9})_2$ formed β -sheets while $C_{18}-(PEP_{Au}^{K,9})_2$ showed very little secondary structure character in both fluorescence and CD spectroscopy (Figure 4-4b, c). $C_{18}-(PEP_{Au}^{G,9})_2$ has the steepest fluorescence growth profile and thus assembles the fastest, while $C_{18}-(PEP_{Au}^{N,9})_2$ assembles slower but reaches the same signal intensity (Figure 4-4b). $C_{18}-(PEP_{Au}^{K,9})_2$ displayed significantly less fluorescence and $C_{18}-(PEP_{Au}^{E,9})_2$ displayed none (Figure 4-4b). $C_{18}-(PEP_{Au}^{G,9})_2$ and $C_{18}-(PEP_{Au}^{N,9})_2$ both have intense but broad peaks centered around 205 nm in the CD spectra indicating the dominant secondary structures is PPII helices, and the higher wavelength shoulder of these peaks indicate β -sheets are present as well (Figure 4-4c).^{50,70,84,88,91,93} $C_{18}-(PEP_{Au}^{E,9})_2$ showed a weak, broad peak centered at 205 nm while no CD signal was detected for $C_{18}-(PEP_{Au}^{K,9})_2$ (Figure 4-4c). These spectroscopic results are consistent with our initial observations: side chains with charged residues interrupt fiber formation due to the repulsion of like-charges. When assembly reactions were conducted with 75 nM $C_{18}-(PEP_{Au}^{K,9})_2$, a small yield of fibers was observed, indicating the critical aggregation concentration for that particular conjugate was between the 0.5X and 1X concentrations.

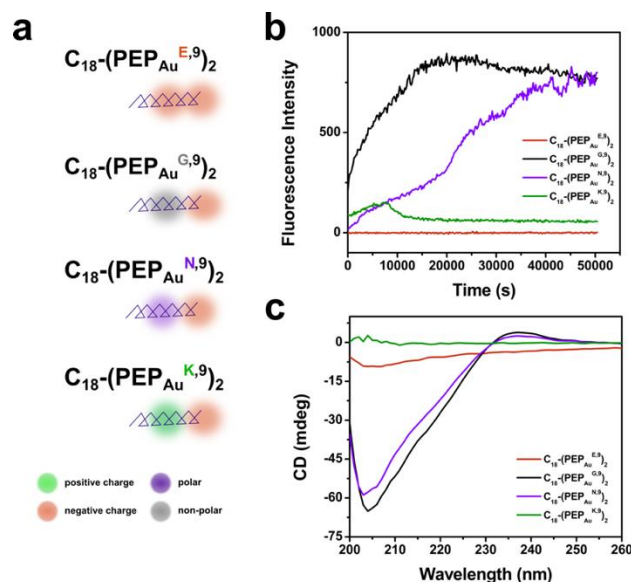


Figure 4-4. Single-component assembly data for peptide conjugate series. (a) Illustration of PPII regions of each conjugate with electrostatics highlighted. (b) Fluorescence kinetics spectra from 0-14 hours and (c) CD spectra of single-component soft assemblies, confirming low fiber concentration from $C_{18}-(PEP_{Au}^{E,9})_2$ and $C_{18}-(PEP_{Au}^{K,9})_2$ and high concentration from $C_{18}-(PEP_{Au}^{G,9})_2$ and $C_{18}-(PEP_{Au}^{N,9})_2$.

In order to examine the fiber morphology, 75 nM solutions of the conjugates were imaged using atomic force microscopy (AFM). $C_{18}-(PEP_{Au}^{G,9})_2$ and $C_{18}-(PEP_{Au}^{N,9})_2$ formed a high yield of helical ribbon fibers and $C_{18}-(PEP_{Au}^{K,9})_2$ formed a significantly lower yield of fibers that were either cylindrical fibers or helical ribbons with inconsistent pitch (Appendix Figure 45). We attributed this again to electrostatic repulsion between the protonated lysine residues; any assembly is perhaps due to a small amount of charge stabilization between the positive lysine side chains and the deprotonated peptide C-terminus. When subjected to Au NP assembly conditions at 0.5X and 1X concentrations, $C_{18}-(PEP_{Au}^{G,9})_2$ formed single helices consistent with previous studies^{68,70} (Appendix Figure 47, Appendix Figure 51). $C_{18}-(PEP_{Au}^{N,9})_2$ formed small aggregates and discrete Au NPs—this result correlates to the binding score-based

prediction, as the free peptide does not have the optimal degree of Au surface contact for superstructure formation (Appendix Figure 48, Appendix Figure 53). $C_{18}-(PEP_{Au}^{K,9})_2$ did not form organized structures, mostly producing discrete Au NPs with a small yield of disordered linear aggregates (Appendix Figure 49, Appendix Figure 53).

Next, we analyzed the fiber assemblies of 1:1 mixture of the three pairs of peptide conjugates ($C_{18}-(PEP_{Au}^{E,9})_2 + C_{18}-(PEP_{Au}^{X,9})_2$ where $X = G, N, K$, and total peptide conjugate concentration was 75 nM). The G,9 + E,9 sample displayed the spectroscopic signatures of β -sheet assembly, although it was initially unclear if the sample was co-assembling or $C_{18}-(PEP_{Au}^{G,9})_2$ was assembling alone. When the CD spectrum and fluorescence growth profile for G,9 + E,9 was compared to the assembly studies of $C_{18}-(PEP_{Au}^{G,9})_2$ at 0.5X concentration, the spectroscopic signals did not increase despite the peptide conjugate concentration doubling. This indicates that the same amount of β sheets are present in solutions of 0.5X $C_{18}-(PEP_{Au}^{G,9})_2$ and 1X G,9 + E,9. The fiber morphology was slightly different, with AFM analysis showing an increase in fibers with variable pitch (Figure 4-5b, c, d). Together, these results show that the $C_{18}-(PEP_{Au}^{E,9})_2$ conjugates still do not assemble readily in the presence of $C_{18}-(PEP_{Au}^{G,9})_2$ due to the lack of electrostatic attraction in the binding module between glycine and glutamic acid. The spectroscopic results for 37.5 nM $C_{18}-(PEP_{Au}^{N,9})_2$ and N,9 + E,9 had subtle differences; the CD spectrum contained a broader primary peak, indicating a higher β -sheet concentration (Figure 4-5b), and the fluorescence growth profile was significantly steeper, indicating a more rapid elongation phase (Figure 4-5c). The pitch of these fibers was fairly consistent although cylindrical fibers with no helical character were also observed (Figure 4-5e). The assembly

profile of K,9 + E,9 showed the most significant difference from the single component assemblies, as the two conjugates together display an immediate intense fluorescence and the CD spectrum has a broad peak indicating significant β -sheet formation (Figure 4-5b, c). K,9 + E,9 produces a high yield of helical fibers with consistent pitch and generally shorter length than any of the other samples, which is an observed characteristic of rapidly assembling conjugates (Figure 4-5f).

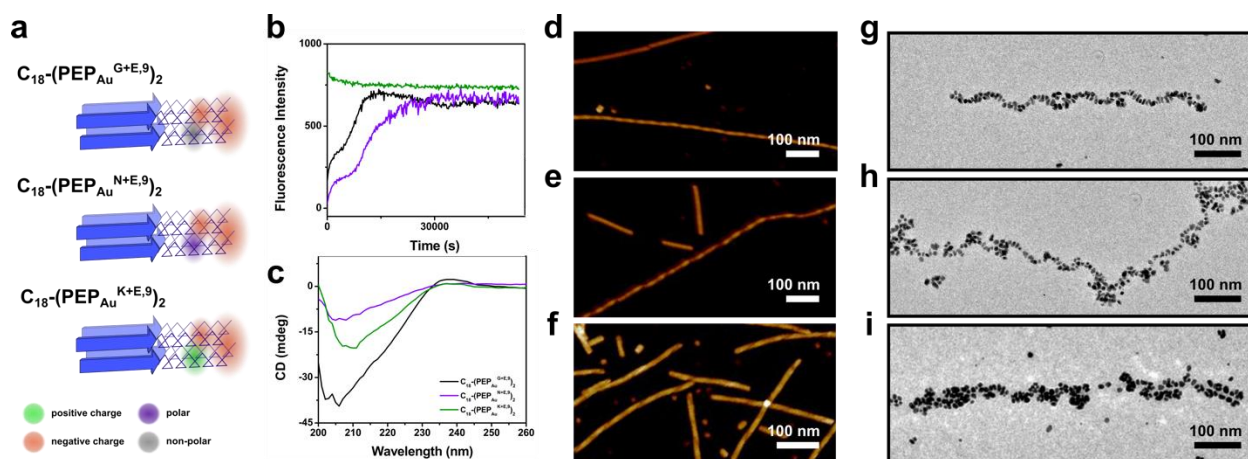


Figure 4-5. Assemblies produced by mixed conjugates. (a) Illustration of electrostatic interactions in each combination. Spectroscopic visualization of co-assembly secondary structures using (b) fluorescence kinetic spectra and (c) CD spectra. AFM images of fibers formed from (d) G,9 + E,9, (f) N,9 + E,9, and (f) K,9 + E,9. Au NP single helices produced by (g) G,9 + E,9 and (h) N,9 + E,9. (i) Linear superstructures produced from K,9 + E,9.

When subjected to Au NP assembly conditions, single helices were observed in the G,9 + E,9 mixtures, suggesting that either these superstructures were assembled on fibers with majority $C_{18}-(PEPAu^{G,9})_2$ conjugates, or the small degree of co-assembly does not affect the Au NP superstructures (Figure 4-5g). Interestingly, the N,9 + E,9 mixture produced single helices (Figure 4-5h). While the superstructures were slightly less organized than previously observed,⁶⁸

combining the electrostatic stabilization of the asparagine conjugate with $C_{18}-(PEP_{Au}^{E,9})_2$ increased the assembly propensity and collectively produced a binding score roughly optimal for single helix formation. The structures formed from the oppositely charged conjugates were linear, often resembling a blend of single and double helices (Figure 4-5i). Based on our previous study, this indicates that the binding score of the two combined would be slightly too high to synthesize pure single helices. However, the efficacy of a cooperative assembly approach for this class of Au NP superstructures is clearly demonstrated—electrostatic repulsion can be integrated for decreased assembly propensity, and vice versa, that attraction can be leveraged to produce structures. Additionally, the arrangement of Au NPs on a fiber depends on both conjugates, as mixing $C_{18}-(PEP_{Au}^{N,9})_2$ (low binding affinity) with $C_{18}-(PEP_{Au}^{E,9})_2$ (moderate to high binding affinity) produces fibers with a moderate binding affinity required to direct the synthesis of Au NP single helical superstructures.

4.3 Conclusion

In order to design more complex nanomaterials, the scaffolds upon which they are built must also become more complex. In this work, we explore the use of cooperative assembly through electrostatic interactions, demonstrating that rationally designed conjugates can assemble and direct NP superstructures. This research lays the groundwork for multi-functional and dynamic superstructures achieved by mixing peptide conjugates designed with different functionalities.

4.4 Experimental Methods

4.4.1 General Methods and Materials

All chemicals were purchased from commercial sources and used without further purification. The peptides were synthesized using established microwave-assisted solid-phase peptide synthesis procedures using as CEM Mars microwave. For all aqueous solutions, NanoPure water (18.1 m Ω) from a Barnstead Diamond purification system was used. The peptides and peptide conjugates were purified using reverse phase high-performance liquid chromatography (HPLC) on an Agilent 1200 liquid chromatographic system equipped with diode array and multiple-wavelength detectors, equipped with a Zorbax-300SB C₁₈ column. Peptide and peptide conjugate masses were confirmed via liquid chromatography mass spectrometry (LC-MS) on a Shimadzu LC-MS 2020 instrument. Ultraviolet-visible (UV-vis) spectra were collected using an Agilent 8453 UV-vis spectrometer with a quartz cuvette (10 mm path length). All microscopy image measurements were collected using ImageJ.

4.4.2 Synthesis

4.4.2.1 Peptide Synthesis

All peptides were synthesized using established microwave-assisted solid-phase peptide synthesis protocols. Briefly, 138.8 mg (0.25 mmol) of Fmoc-Phe-Novasyn TGA resin (Millipore catalog no. 8560340001) was transferred to a filtration manifold and swelled in N, N'-dimethylformamide (DMF) for about 30 minutes. To remove the Fmoc protecting group from the

resin, 2 mL of 20% 4-methylpiperidine in DMF solution was added, and the vessel was microwaved with agitation. The deprotection method on the microwave consisted of a 1 minute temperature ramp to 75 °C, followed by a 2 minute hold. The deprotection solution was removed by filtration and the resin was rinsed with approximately 3 mL DMF for 30 seconds and 3 repetitions. The solid Fmoc-protected amino acids (4 equiv, 0.125 mmol) were activated with 0.1 M solution of O-(1H-6-chlorobenzotriazole-1-yl)-1,1,3,3-tetramethyluronium hexafluorophosphate (HCTU) in 1-methyl-2-pyrrolidinone (NMP) (5 equiv, 1.25 mL) and N,N-diisopropylethylamine (DIEA) (7 equiv, 0.175 mmol, 30.4 µL), vortexed to dissolve and centrifuged, then allowed to sit on the benchtop for at least 5 minutes. The activated amino acid solution was added to the resin vessel and microwaved with agitation using the coupling method, a 1-minute temperature ramp to 75 °C followed by a 5 minute hold. The excess solution was drained, and the resin was again washed with DMF. This procedure was repeated for each subsequent amino acid. Every proline and proline-adjacent amino acid was double-coupled (*i.e.* coupling steps of two equivalents per amino acid were carried out in sequence). The final step was the deprotection of the N-terminal alanine residue and coupling of 5-azido pentanoic acid, using the previously discussed coupling protocol. The completed sequence was cleaved from the resin with a cocktail of 90% trifluoroacetic acid, 5% diisopropylsilane, and 5% NanoPure water. The product peptide was precipitated with cold diethyl ether and collected, then lyophilized and purified via HPLC.

4.4.2.2 Peptide Conjugate Synthesis

The azide-terminated peptides were coupled to C₁₈-dialkyne using established protocols using a copper-catalyzed click reaction described previously.^{61,84}

4.4.3 Assembly Conditions

4.4.3.1 Peptide Conjugate Assembly

The lyophilized peptide conjugate (9 nmol for single component (37.5 nM) studies and 18 nmol (75 nM) total for co-assembly studies) was dissolved in 250 μ L of 0.1 M HEPES buffer and left undisturbed at room temperature overnight.

4.4.3.2 Nanoparticle Superstructure Assembly

Lyophilized peptide conjugate (9 nmol for single component (37.5 nM) studies and 18 nmol (75 nM) total for co-assembly studies) was dissolved in 250 μ L of 0.1 M HEPES buffer and incubated on the benchtop for 30 minutes. Next, 2 μ L of a 1:1 mixture of 0.1 M chloroauric acid (HAuCl₄) in NanoPure water and 0.1 M triethylammonium buffer was added to the solution. When a black precipitate was observed, the solution was vortexed until it dissolved. The solution was incubated on the benchtop for 16 hours to allow for maximum assembly.

4.4.4 Characterization and Sample Preparation

4.4.4.1 Circular Dichroism (CD) Spectroscopy

Lyophilized peptide conjugate (9 nmol for single component (37.5 nM) studies and 18 nmol (75 nM) total for co-assembly studies) was dissolved in 250 μ L 0.01 M HEPES buffer and allowed to incubate overnight. CD measurements were collected using an Olis DSM 17 CD spectrometer with a quartz cuvette (0.1 cm path length) at 25 °C with a scan rate of 8 nm/min.

4.4.4.2 Fluorescence Plate Reader

Thioflavin T (ThT) fluorescence assays were conducted in a 96-well black plate (F-bottom Greiner bio-one No.655209) at 26 °C in a Tecan M1000 fluorescence plate reader. The ThT fluorescence kinetic profile was recorded at 3 min reading intervals and 5 s shaking (372 rpm) before each read (440 nm excitation, 482 nm emission). Lyophilized peptide conjugates (9 nmol for single component (37.5 nM) studies and 18 nmol (75 nM) total for co-assembly studies) were dissolved in 250 μ L of 5 μ M ThT in 0.1 M HEPES buffer. After brief agitation, the sample solution was transferred to each well. All fluorescence spectra signals have been background corrected.

4.4.4.3 Atomic Force Microscopy (AFM)

AFM images were collected on a Bruker Dimension Icon Atomic Force microscope controlled by NanoScope VI controller in ScanAsystAir mode. 0.1% APTES (3-aminopropyltriethoxy-silane) solution was drop casted onto a freshly cut mica surface, rinsed with NanoPure

water and allowed to dry in a dessicator overnight. 50 μL of peptide conjugate in 0.1 M HEPES (75 μM) was then drop cast and rinsed with water after 10 min and allowed to dry.

4.4.4.4 Transmission Electron Microscopy (TEM)

TEM images were collected on Hitachi H-9500 microscope operating at 300 kV (Nanoscale Fabrication and Characterization Facility, Petersen Institute of Nanoscience and Engineering, University of Pittsburgh, PA). Images were analyzed using ImageJ software.

5.0 Broader Implications and Future Directions

The research in this dissertation studied the fundamental effect of atomic- and molecular-level modifications on biological and synthetic nanoscale structure and function. While the effect of structural modifications like the aliphatic tail length or peptide valency were already established, there remained a question of how amino acid modifications would affect fiber and Au NP superstructure growth and morphology.

This dissertation begins by studying the effect of hydrophobic modifications to the peptide conjugates β -sheet forming amino acids. Rational substitutions were made to increase the peptide hydrophobicity without disrupting the existing β -sheet secondary structures in assembled fibers. While the results were presented in the context of our single- and double-helical NP superstructures, we developed a fundamental strategy for leveraging peptide modifications to increase or decrease amyloid fibrilization. Chapters 3 and 4 shift the focus to the peptide-Au NP relationship. When understanding source of the double- versus single-helical Au NP superstructures, we determined this nanoscale structural rearrangement can be correlated to the Au(111) affinity of the amino acids. We developed a method to quantify this interaction using ‘binding scores’ generated from computational simulations, which allowed up to compare the cumulative affinity of a specific peptide sequence. Additionally, these ‘binding scores’ could be calculated for the individual assembly module amino acids and particle binding amino acids. This revealed a clear trend of decreasing C-terminal peptide-Au affinity accompanying the nanostructure transformation. The additive ‘binding scores’ allowed us to examine a specific

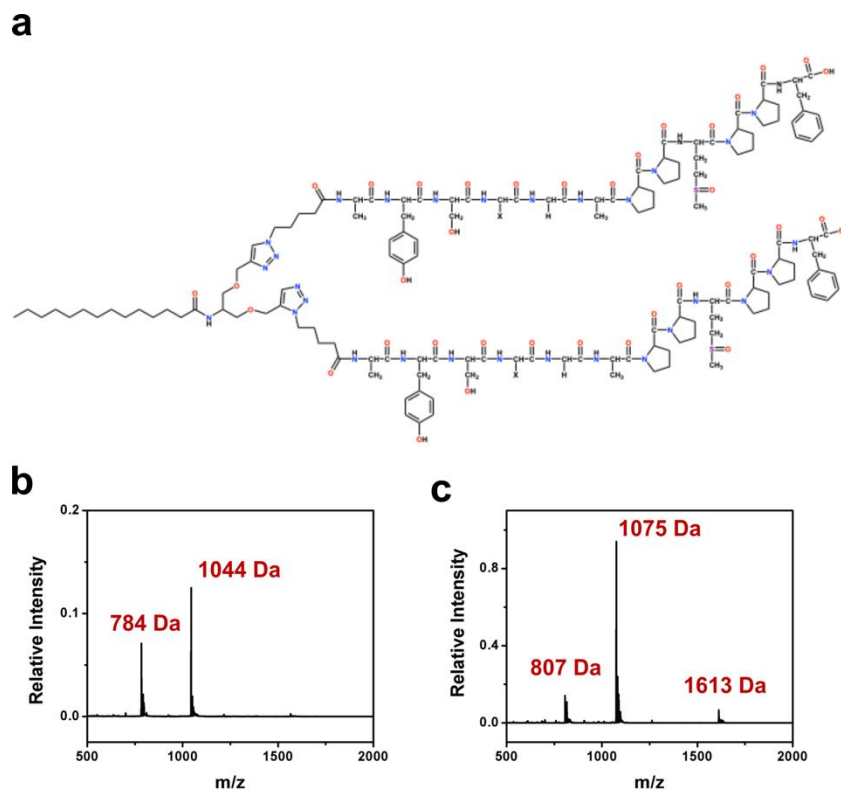
region of the peptide; while in our work this was used because our molecular model suggests that only the C-terminal amino acids associate with the Au NP, this could also be useful for the design of site-specific inorganic binding peptides.

Typically, a single modification to a peptide will impact the entire secondary structure and thus the interaction with a surface, making it challenging to study series of modified peptides on a surface. Interestingly, we determined that the PPII helical secondary structure imparts a degree of rigidity to the binding module, allowing us to pinpoint the effects of specific residue modifications on the Au affinity without having to consider the entire peptide conformation. This insight is important for peptide biomineralization because it provides a sequence-dependent method to control one of the many variables when a peptide is immobilized on a surface.

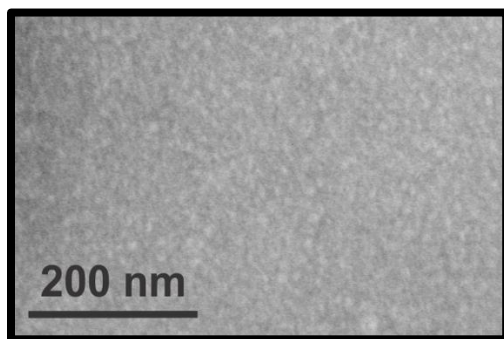
The final chapter of this work adds a layer of functionality to the design system. By introducing designed electrostatic interactions, we increase our ability to control the fibrilization of the peptide conjugates. Additionally, we were able to study the effect of external charge interactions on the peptide-Au NP interactions. This project lays the groundwork for improving upon this work and designing new electrostatically-driven Au NP assembly methods. Understanding the conjugate as three distinct sections (*i.e.* the hydrophobic tail and β -sheet amino acids in the assembly module and the PPII amino acids in the particle binding module) provides a foundation to introduce more structural and functional complexity to our assembly system, like introducing dynamic functional groups to produce environmentally-responsive Au NP superstructures.

By studying a peptide-based amphiphilic molecular building block, we have created a versatile and acutely tunable Au NP assembly method. The information we learn from studying the fiber assembly is relevant for nanoparticle assembly but also in general relates to peptide and protein amyloid fibrillation. Additionally, the assembled structures bind and stabilize Au NP assemblies, providing a platform to study peptide-inorganic particle interactions. We produce NP superstructures with unique plasmonic properties, allowing us to investigate the effect of structure and morphology of Au NP assemblies. The information gained from these research efforts is important for developing our method of peptide-based Au NP assembly and also provides key insights in the fields of amphiphilic fibrillation and peptide biomineralization. Ultimately, the key to designing precisely-controlled synthetic materials is a strong understanding of the fundamental cause and effects that arise at the molecular scale. This work provides those insights and paves the way for new synthetic methods and structures.

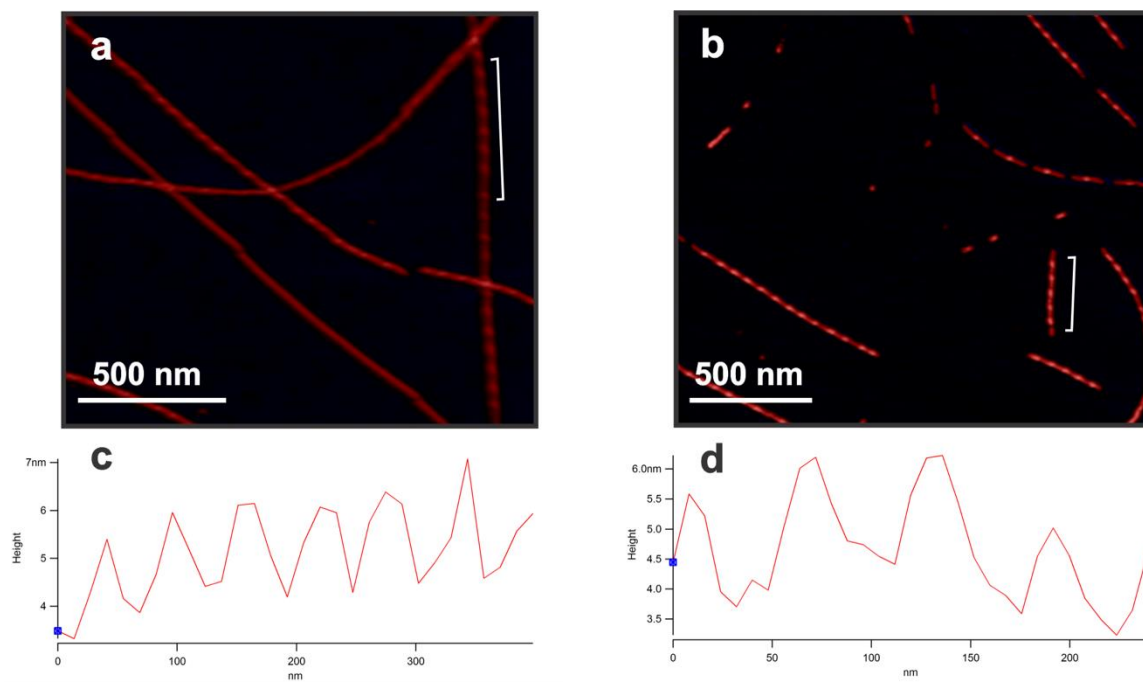
Appendix A Supporting Information for Chapter 2: “Leveraging Peptide Sequence Modifications to Promote Assembly of Chiral Helical Gold Nanoparticle Superstructures”



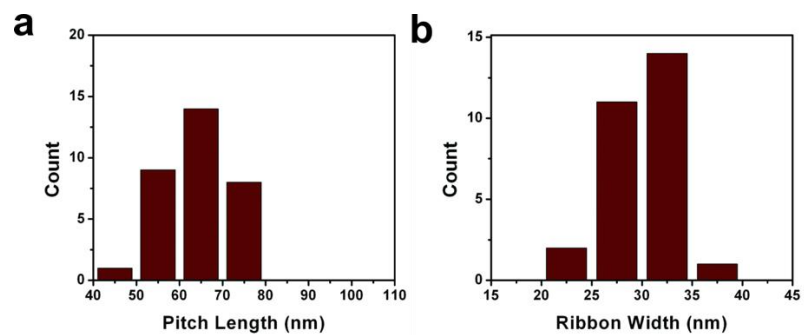
Appendix Figure 2. (a) Representative molecular structure of C_{14} -(PEP_{Au}^{Mox})₂^X. LC-MS mass assignment of (b) C_{14} -(AYSTGAPPM^{ox}PPF)₂, $m/z = 1044$ Da ($M-3H^+$)/3; 784 Da ($M-4H^+$)/4; and (c) C_{14} -(AYSFGAPPM^{ox}PPF)₂, $m/z = 1613$ Da ($M-2H^+$)/2; 1075 Da ($M-3H^+$)/3; 807 Da ($M-4H^+$)/4.



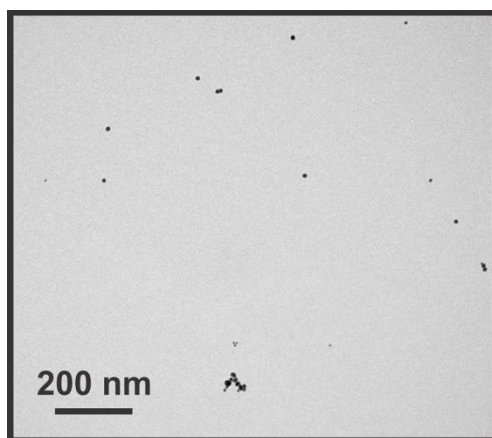
Appendix Figure 3. Negatively-stained TEM image of C_{14} -(AYSSGAPPM^{ox}PPF)₂ after assembly experiment in 0.1 M HEPES. Fiber assemblies are not observed.



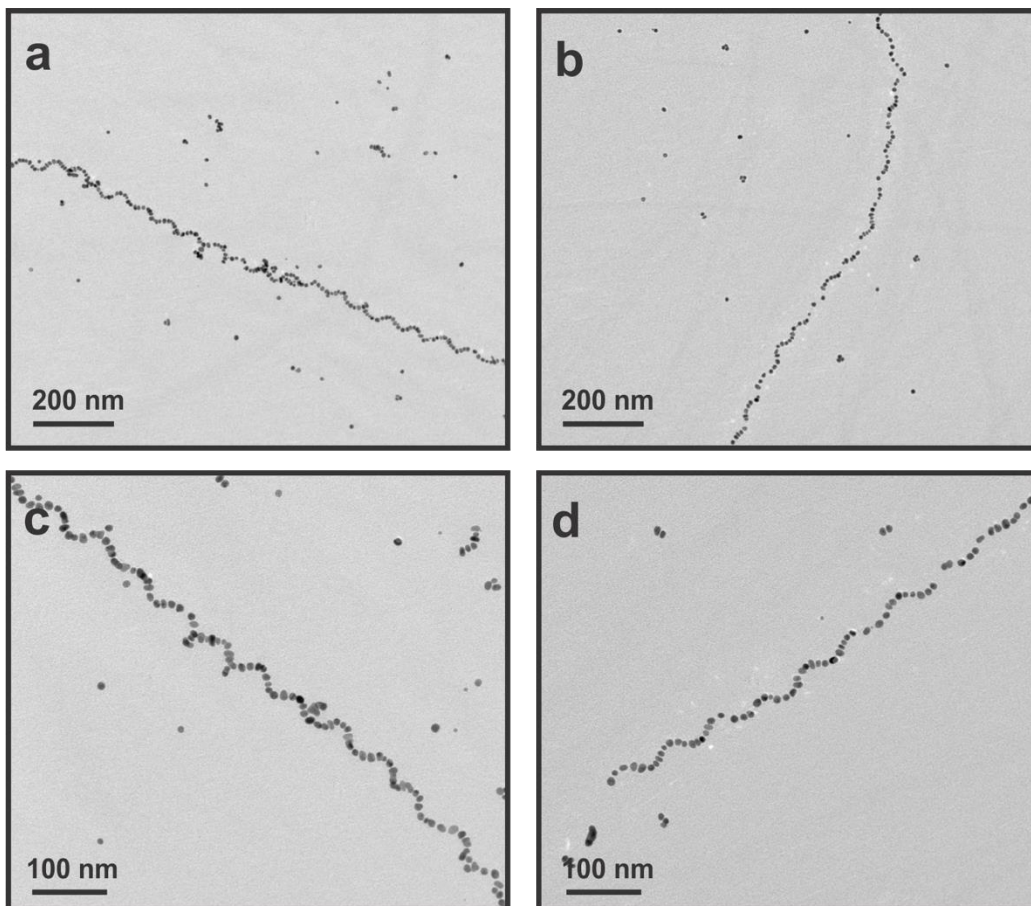
Appendix Figure 4. Additional AFM images of (a, b) $C_{14}-(AYSFGAPPm^{ox}PPF)_2$, with labeled segments corresponding to (c, d) height traces.



Appendix Figure 5. AFM measurements of C_{14} -(AYSFGAPPMM^{ox}PPF)₂. (a) Ribbon pitch distribution and (b) ribbon width distribution.

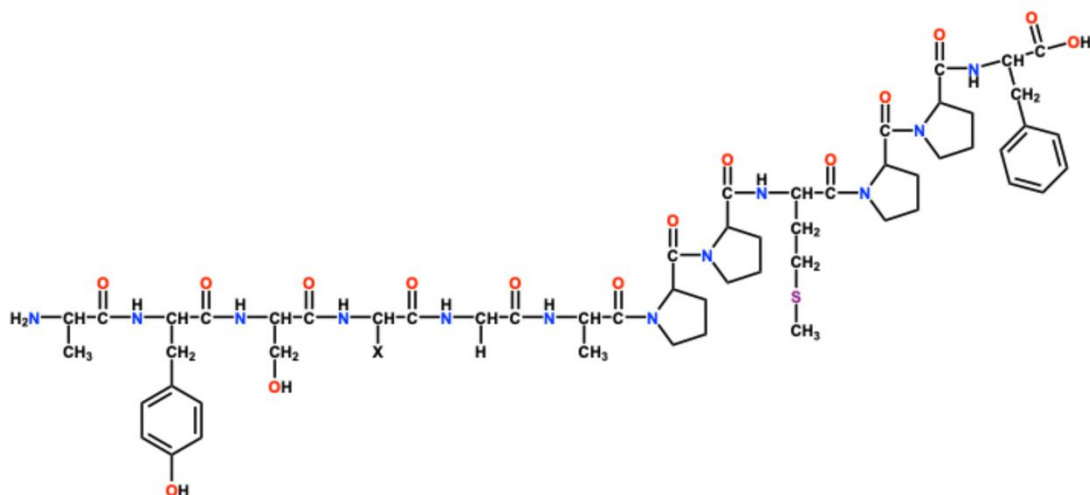


Appendix Figure 6. TEM image of discrete Au NPs synthesized using C_{14} -(AYSSGAPPMM^{ox}PPF)₂.

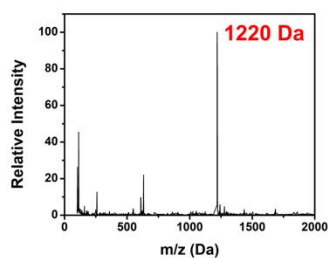


Appendix Figure 7. Additional TEM images of single helices prepared using C_{14} -(AYSFGAPPM^{ox}PPF)₂.

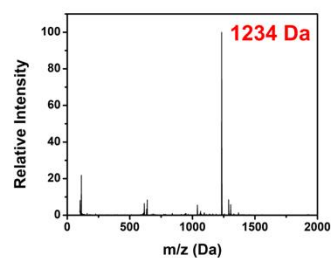
a



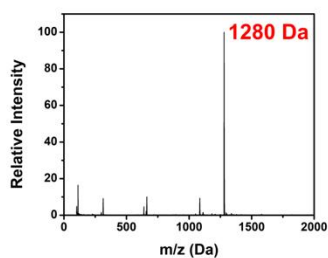
b



c

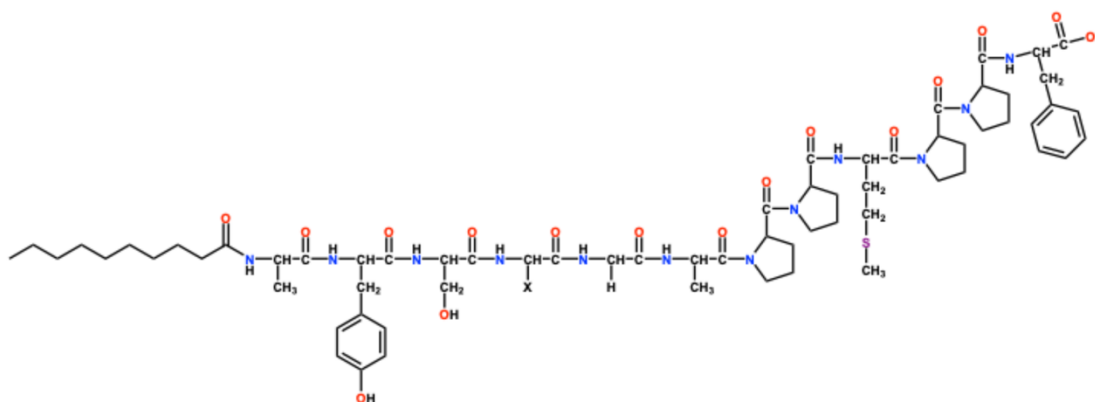


d

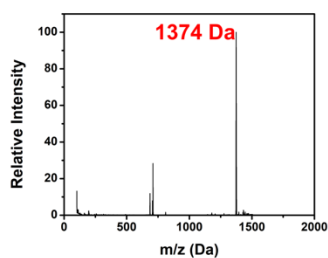


Appendix Figure 8. (a) Representative molecular structure of $\text{NH}_2\text{-PEP}_{\text{Au}}^{\text{X}}$. LC-MS mass assignment of (a) $\text{NH}_2\text{-AYSSGAPPMPF}$, $m/z = 1220$ Da (M-H^+); 633 Da ($\text{M-H}^+ + \text{HCOO}^-$)/2; 609 Da (M-2H^+)/2; (b) $\text{NH}_2\text{-AYSTGAPPMPF}$, $m/z = 1234$ Da (M-H^+); 641 Da ($\text{M-H}^+ + \text{HCOO}^-$)/2; 617 Da (M-2H^+)/2; and (c) $\text{NH}_2\text{-AYSFGAPPMPF}$, $m/z = 1280$ Da (M-H^+); 663 Da ($\text{M-H}^+ + \text{HCOO}^-$)/2; 639 Da (M-2H^+)/2.

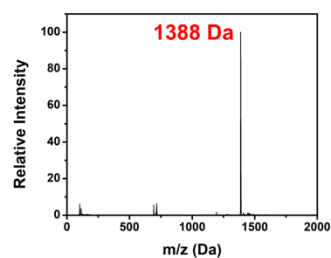
a



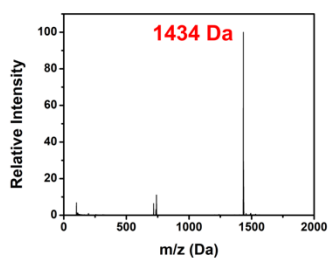
b



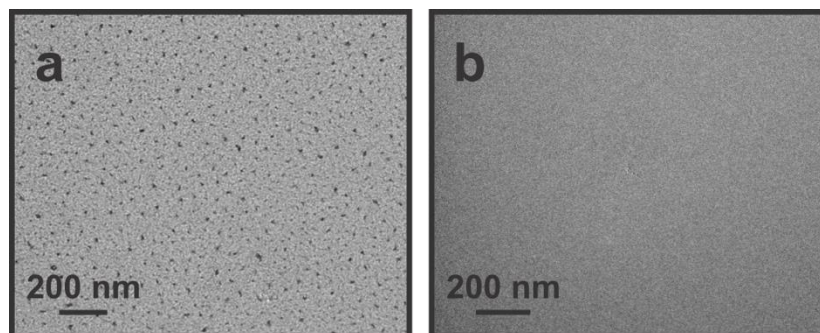
c



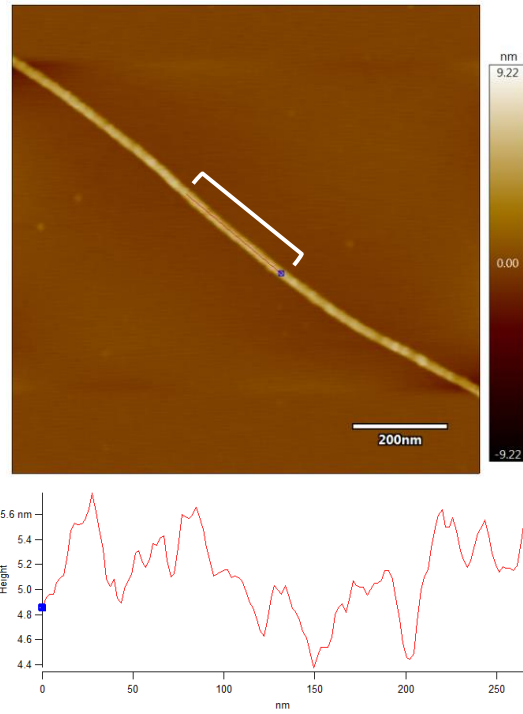
d



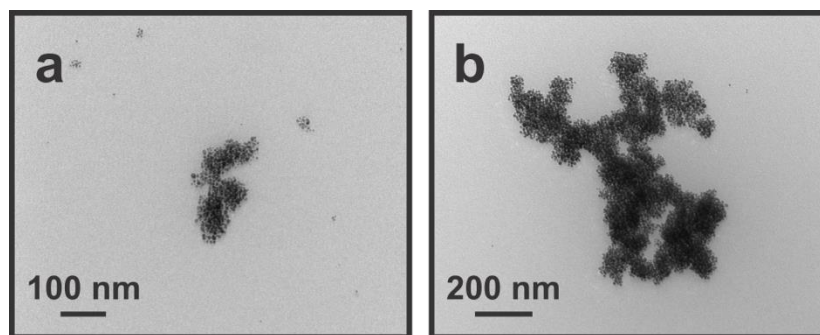
Appendix Figure 9. (a) Representative molecular structure of C_{10} -PEP_{Au}^X. LC-MS mass assignment of (b) C_{10} -AYSSGAPPMPF, $m/z = 1374$ Da ($M-H^+$); 711 Da ($M-H^+ HCOO^-$)/2; 687 Da ($M-2H^+$)/2; (c) C_{10} -AYSTGAPPMPF, $m/z = 1388$ Da ($M-H^+$); 717 Da ($M-H^+ HCOO^-$)/2; 693 Da ($M-2H^+$)/2; and (d) C_{10} -AYSFGAPPMPF, $m/z = 1434$ Da ($M-H^+$); 741 Da ($M-H^+ HCOO^-$)/2; 717 Da ($M-2H^+$)/2.



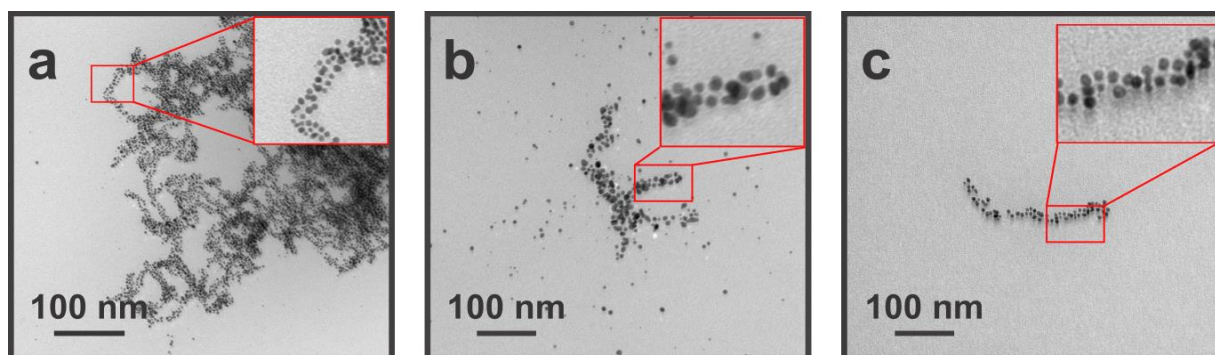
Appendix Figure 10. Negatively-stained TEM image of (a) C₁₀-AYSSGAPMPPF and (b) C₁₀-AYSTGAPMPPF after assembly experiments in 0.1 M HEPES. Fiber assemblies are not observed.



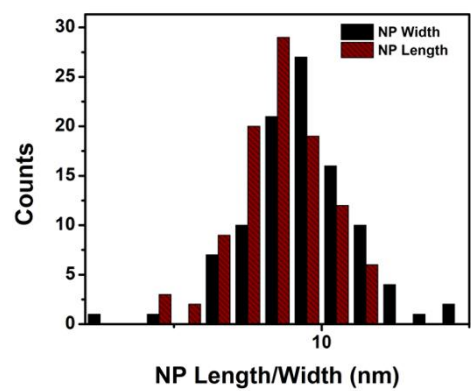
Appendix Figure 11. Additional AFM image of C₁₀-AYSFGAPPMPF fibers. Height trace does not indicate well-defined helicity.



Appendix Figure 12. TEM images of discrete Au NPs/Au NP aggregates formed using (a) C₁₀-AYSSGAPMPPF and (b) C₁₀-AYSTGAPMPPF.



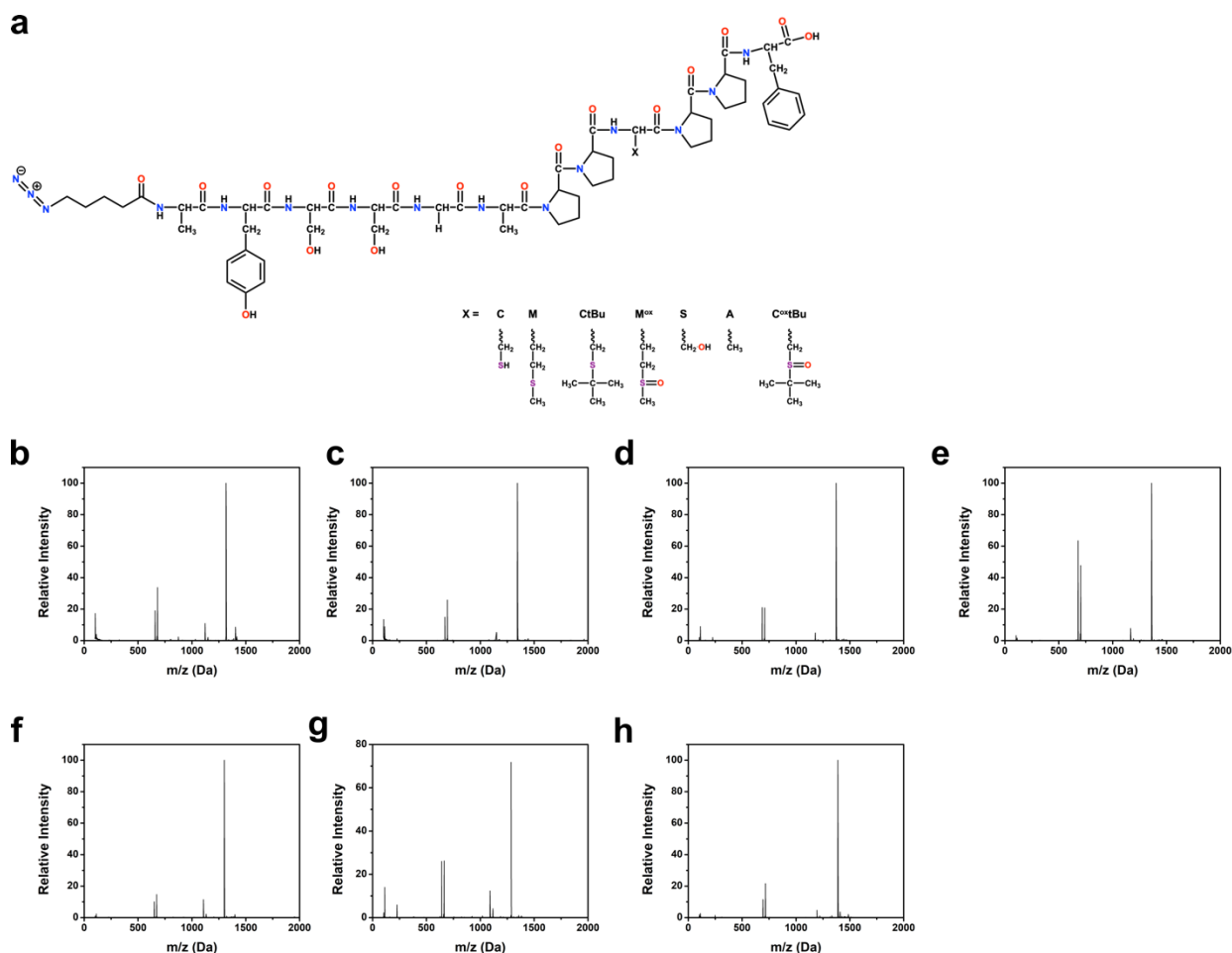
Appendix Figure 13. (a-c) Additional TEM images of Au NP assemblies formed using C₁₀-AYSFGAPMPPF. High magnification images highlight the helical nature of the superstructures.



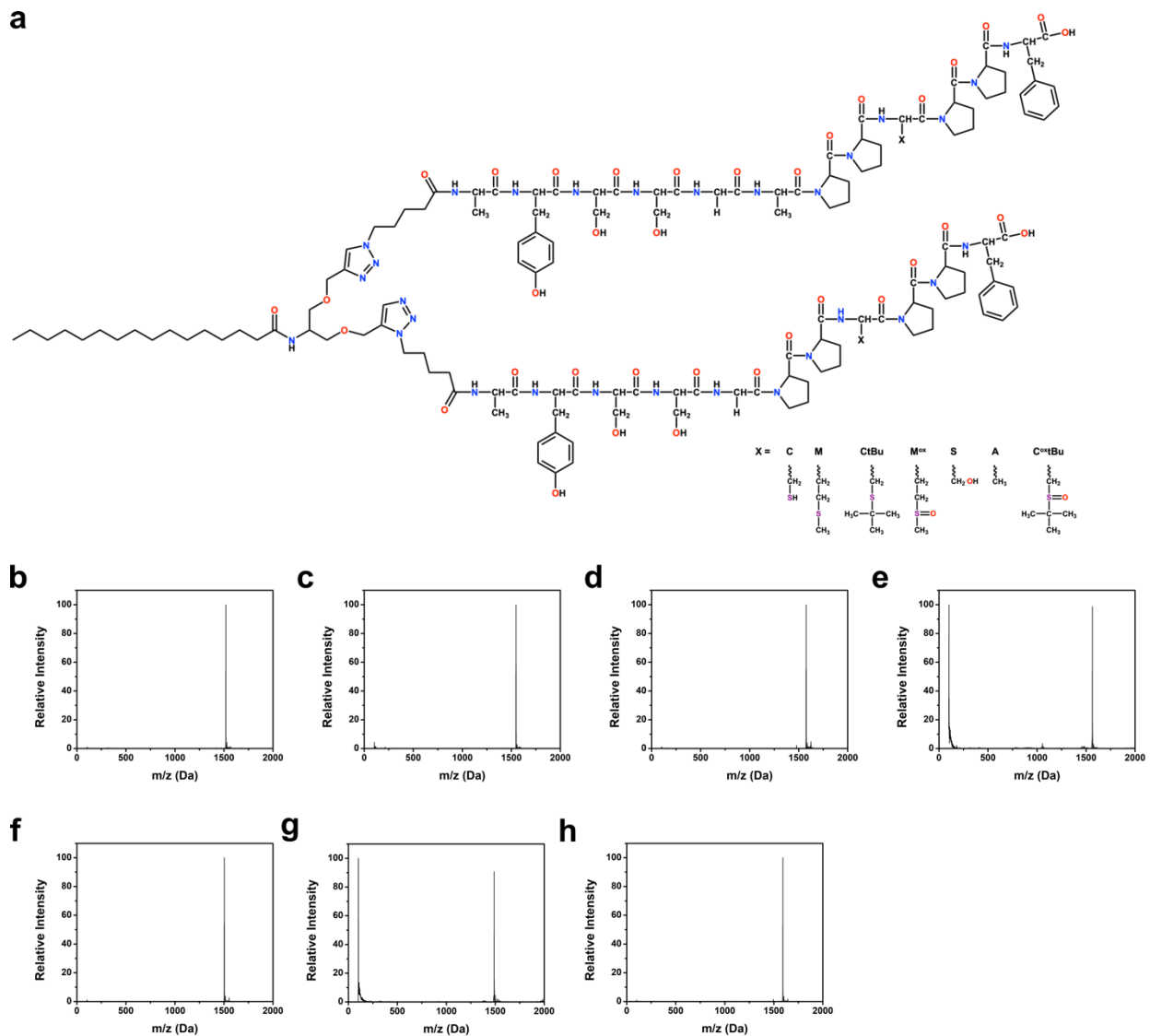
Appendix Figure 14. Particle dimensions of Au NPs within double helices formed using C₁₀-AYSFGAPPMPF.

Appendix B Supporting Information for Chapter 3: “Single Amino Acid Modifications for Controlling the Helicity of Peptide-Based Chiral Gold Nanoparticle Superstructures”

Appendix B.1 Peptide Conjugate Synthesis and Characterization

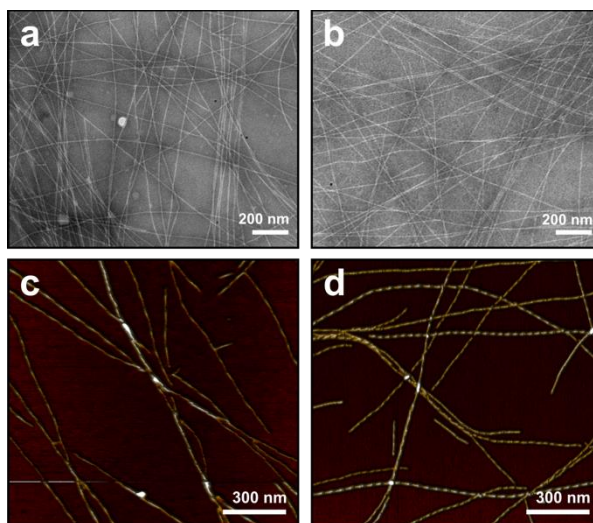


Appendix Figure 15. (a) Representative molecular structure of N₃-AYSSGAPPXPPF. LC-MS mass assignment of (b) N₃-AYSSGAPPCPPF, m/z = 1318 Da (M-H⁺); 682 Da (M-2H⁺+ HCOO⁻)/2; 658 Da (M-2H⁺)/2; (c) N₃-AYSSGAPPMPPF, m/z = 1347 Da (M-H⁺); 696 Da (M-2H⁺+ HCOO⁻)/2; 672 Da (M-2H⁺)/2; (d) N₃-AYSSGAPPCtBuPPF, m/z = 1374 Da (M-H⁺); 710 Da (M-2H⁺+ HCOO⁻)/2; 686 Da (M-2H⁺)/2; (e) N₃-AYSSGAPPM^{ox}PPF, m/z = 1363 Da (M-H⁺); 704 Da (M-2H⁺+ HCOO⁻)/2; 680 Da (M-2H⁺)/2; (f) N₃-AYSSGAPPSPPF, m/z = 1302 Da (M-H⁺); 674 Da (M-2H⁺+ HCOO⁻)/2; 650 Da (M-2H⁺)/2; (g) N₃-AYSSGAPPAPPF, m/z = 1286 Da (M-H⁺); 666 Da (M-2H⁺+ HCOO⁻)/2; 642 Da (M-2H⁺)/2; (h) N₃-AYSSGAPPC^{ox}tBuPPF, m/z = 1390 Da (M-H⁺); 718 Da (M-2H⁺+ HCOO⁻)/2; 694 Da (M-2H⁺)/2.

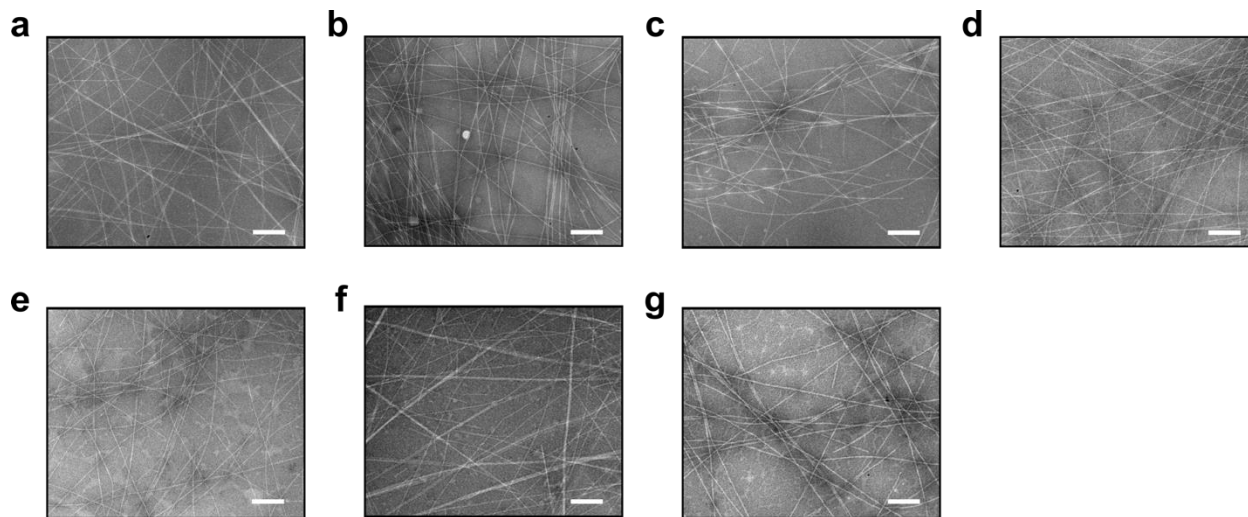


Appendix Figure 16. (a) Representative molecular structure of C_{16} -(AYSSGAPPXPPF)₂. LC-MS mass assignment of (b) C_{16} -(AYSSGAPPCPPF)₂, m/z 1520 Da ($M-2H^+$)/2; (c) C_{16} -(AYSSGAPPMPPF)₂, m/z 1548 Da ($M-2H^+$)/2; (d) C_{16} -(AYSSGAPPCtBuPPF)₂, m/z 1576 Da ($M-2H^+$)/2; (e) C_{16} -(AYSSGAPPM^{ox}PPF)₂, m/z 1565 Da ($M-2H^+$)/2; (f) C_{16} -(AYSSGAPPSPPF)₂, m/z 1504 Da ($M-2H^+$)/2; (g) C_{16} -(AYSSGAPPAPPF)₂, m/z 1488 Da ($M-2H^+$)/2; (h) C_{16} -(AYSSGAPPC^{ox}tBuPPF)₂, m/z 1592 Da ($M-2H^+$)/2.

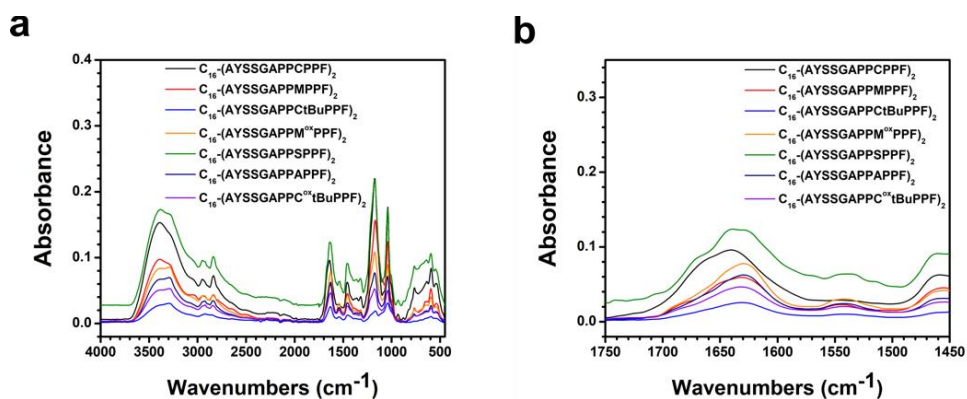
Appendix B.2 Peptide Conjugate Assembly Studies



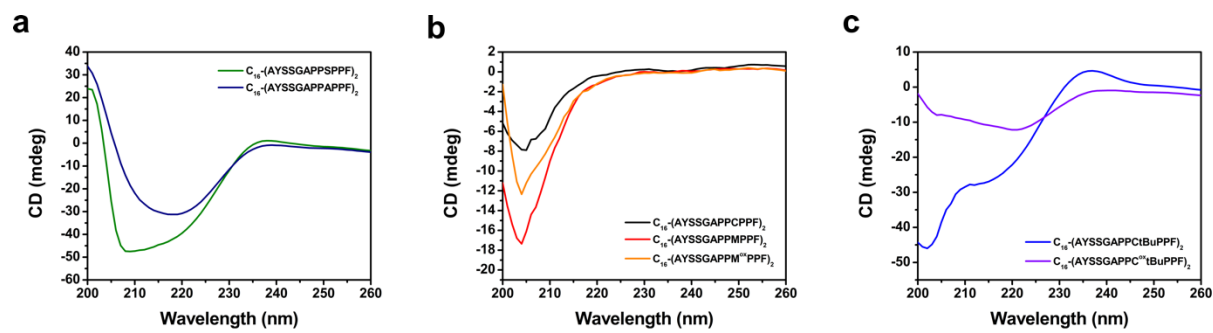
Appendix Figure 17. TEM and AFM images of C_{16} -(AYSSGAPMPPF)₂ (a,c) and C_{16} -(AYSSGAPM^{ox}PPF)₂ (b,d).



Appendix Figure 18. TEM images of peptide conjugate fibers assembled from (a) C_{16} -(AYSSGAPPCPPF)₂, (b) C_{16} -(AYSSGAPMPPF)₂, (c) C_{16} -(AYSSGAPPCtBuPPF)₂, (d) C_{16} -(AYSSGAPPM^{ox}PPF)₂, (e) C_{16} -(AYSSGAPSPPF)₂, (f) C_{16} -(AYSSGAPPAPPF)₂, and (g) C_{16} -(AYSSGAPPC^{ox}tBuPPF)₂. Scale bars 200 nm.

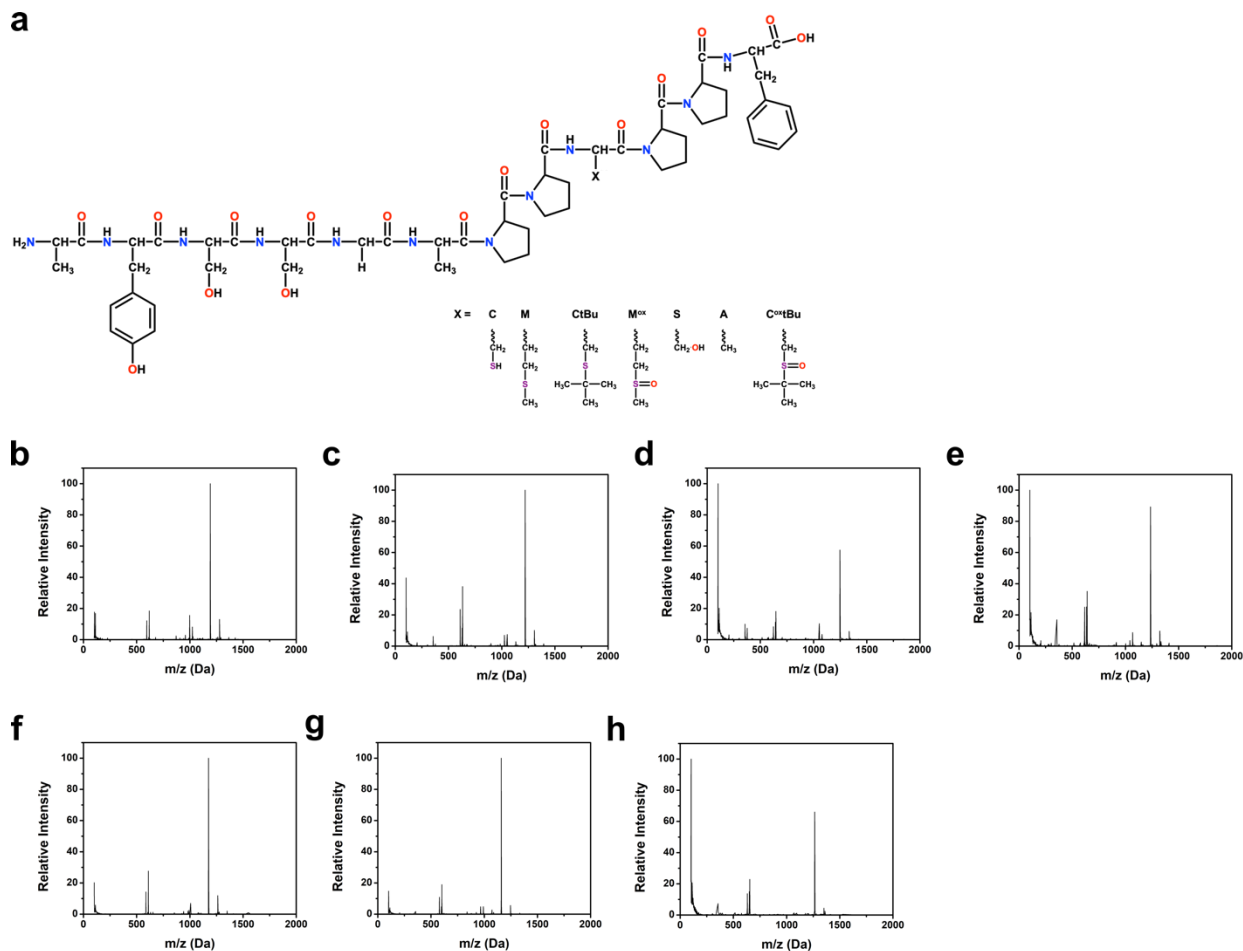


Appendix Figure 19. ATR-FTIR spectra of peptide conjugate fibers showing (a) the full wavelength range and (b) expanded view of the amine region.

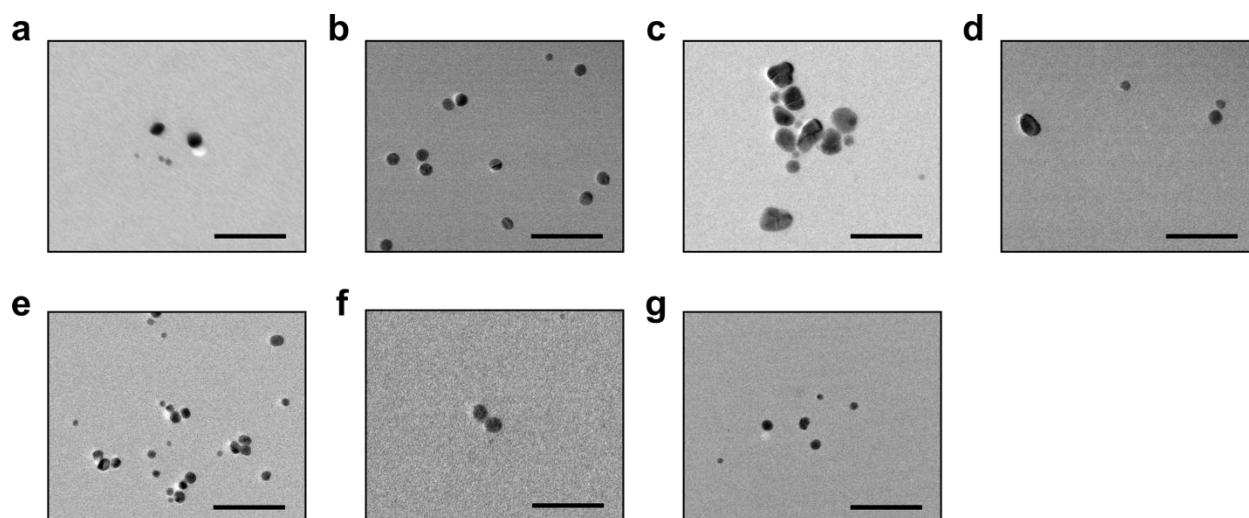


Appendix Figure 20. CD spectra of the peptide conjugate fibers.

Appendix B.3 Synthesis of Amine-Terminated Peptide Variants and NP Synthesis Studies



Appendix Figure 21. (a) Representative molecular structure of NH₂-AYSSGAPPXPPF. LC-MS mass assignment of (b) NH₂-AYSSGAPPCPPF, $m/z = 1193$ Da ($M-H^+$); 619 Da ($M-2H^+ + HCOO^-$)/2; 596 Da ($M-2H^+$)/2; (c) NH₂-AYSSGAPPMPF, $m/z = 1221$ Da ($M-H^+$); 633 Da ($M-2H^+ + HCOO^-$)/2; 610 Da ($M-2H^+$)/2; (d) NH₂-AYSSGAPPCtBuPF, $m/z = 1249$ Da ($M-H^+$); 647 Da ($M-2H^+ + HCOO^-$)/2; 623 Da ($M-2H^+$)/2; (e) NH₂-AYSSGAPPM^{ox}PF, $m/z = 1237$ Da ($M-H^+$); 641 Da ($M-2H^+ + HCOO^-$)/2; 618 Da ($M-2H^+$)/2; (f) NH₂-AYSSGAPPSPF, $m/z = 1177$ Da ($M-H^+$); 611 Da ($M-2H^+ + HCOO^-$)/2; 588 Da ($M-2H^+$)/2; (g) NH₂-AYSSGAPPAPPF, $m/z = 1161$ Da ($M-H^+$); 603 Da ($M-2H^+ + HCOO^-$)/2; 580 Da ($M-2H^+$)/2; (h) NH₂-AYSSGAPPC^{ox}tBuPF, $m/z = 1265$ Da ($M-H^+$); 655 Da ($M-2H^+ + HCOO^-$)/2; 632 Da ($M-2H^+$)/2.

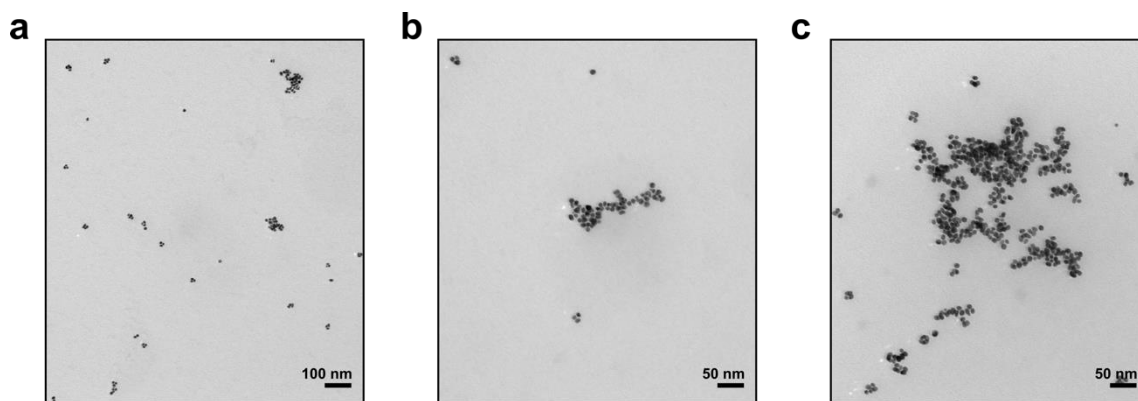


Appendix Figure 22. Au NPs produced from of $\text{NH}_2\text{-AYSSGAPPXPPF}$, where X = (a) C, (b) M, (c) CtBu, (d) M^{ox} , (e) S, (f) A, and (g) $\text{C}^{\text{ox}}\text{tBu}$. Scale bars are 50 nm.

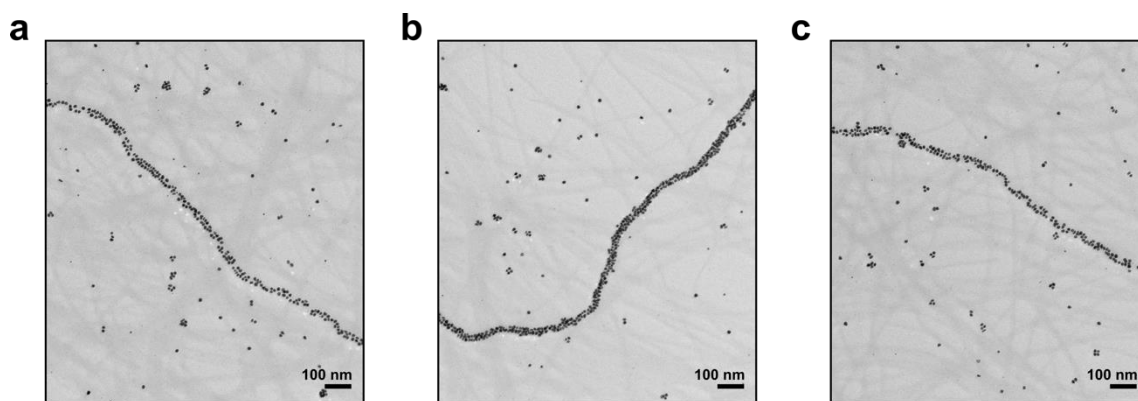
Appendix Table 1. Particle length and width of Au NPs synthesized by amine-terminated peptide variants.

	C	M	CtBu	M^{ox}	S	A	$\text{C}^{\text{ox}}\text{tBu}$
Particle Length (nm)	6.6 ± 3.7	9.6 ± 1.4	14.2 ± 7.4	7.6 ± 3.0	7.3 ± 2.0	4.6 ± 1.8	7.4 ± 2.1
Particle Width (nm)	6.4 ± 3.3	8.7 ± 1.2	12.4 ± 5.7	6.6 ± 1.9	6.3 ± 1.6	4.1 ± 1.4	6.7 ± 1.7

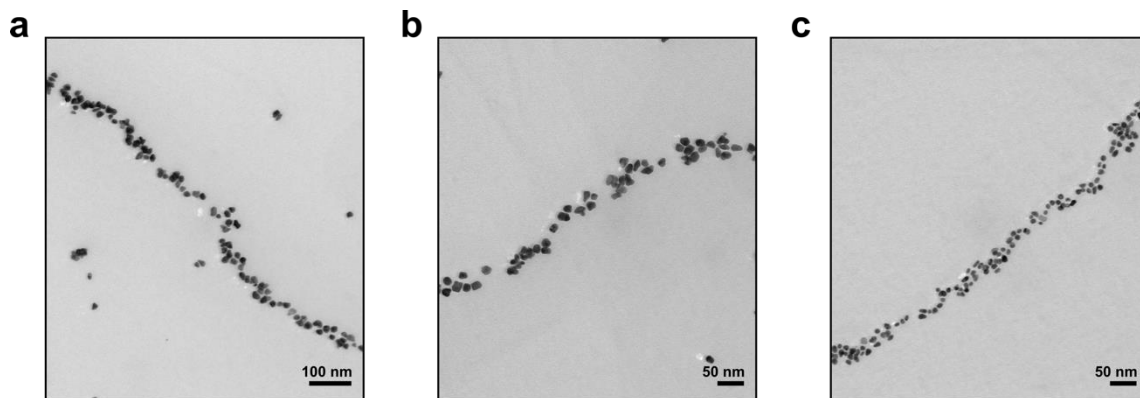
Appendix B.4 Nanoparticle Assembly Studies



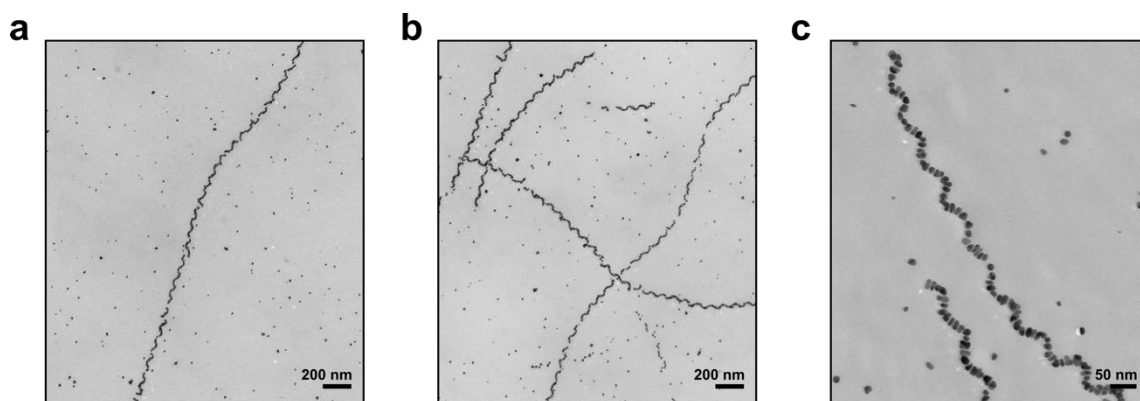
Appendix Figure 23. Additional TEM images of Au NP assemblies produced by C_{16} -(AYSSGAPPCPF)₂.



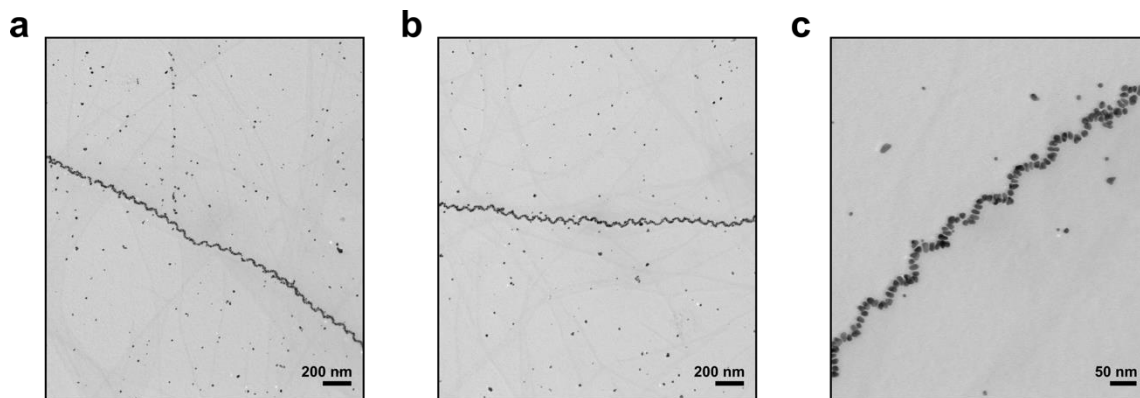
Appendix Figure 24. Additional TEM images of Au NP assemblies produced by C_{16} -(AYSSGAPMPPF)₂.



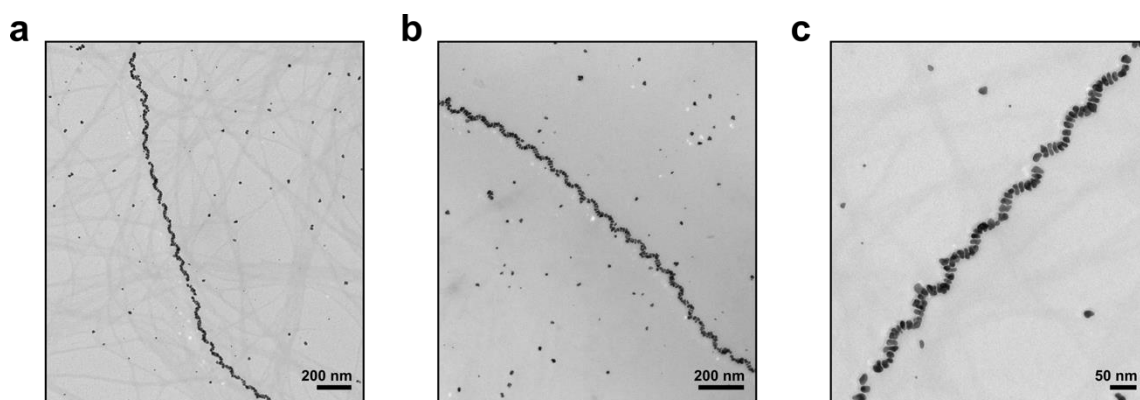
Appendix Figure 25. Additional TEM images of Au NP assemblies produced by C_{16} -(AYSSGAPPCtBuPPF)₂.



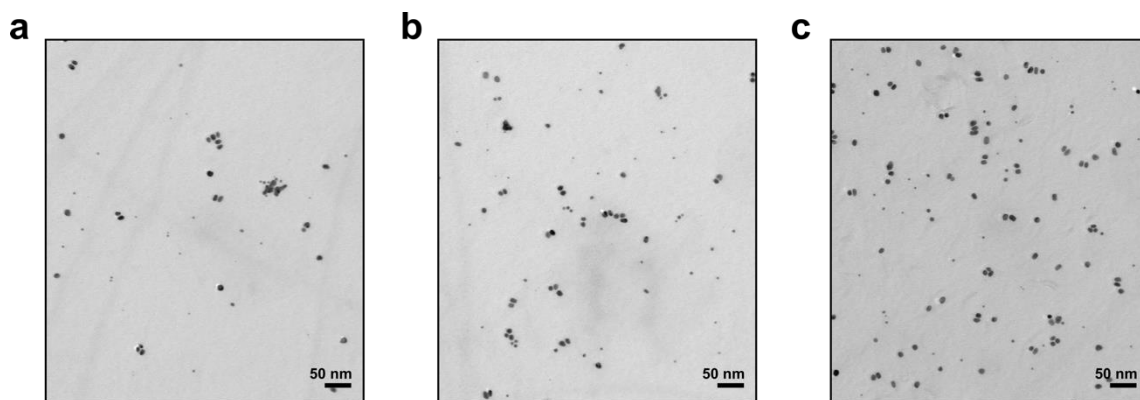
Appendix Figure 26. Additional TEM images of Au NP assemblies produced by C_{16} -(AYSSGAPPM^{ox}PPF)₂.



Appendix Figure 27. Additional TEM images of Au NP assemblies produced by C_{16} -(AYSSGAPSPPF)₂.

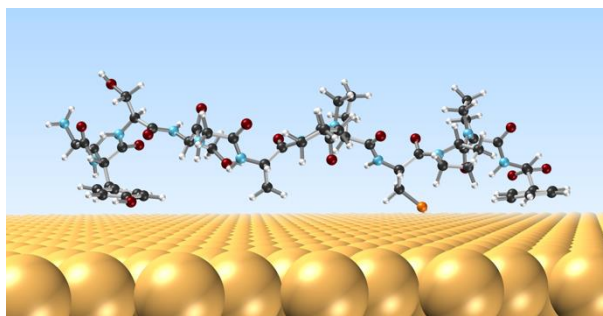


Appendix Figure 28. Additional TEM images of Au NP assemblies produced by C_{16} -(AYSSGAPPAPPF)₂.

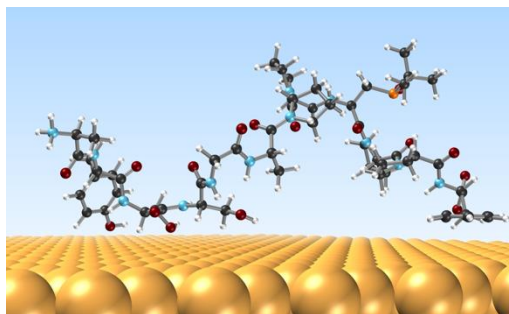


Appendix Figure 29. Additional TEM images of Au NP assemblies produced by C_{16} -(AYSSGAPPC^{ox}tBuPPF)₂.

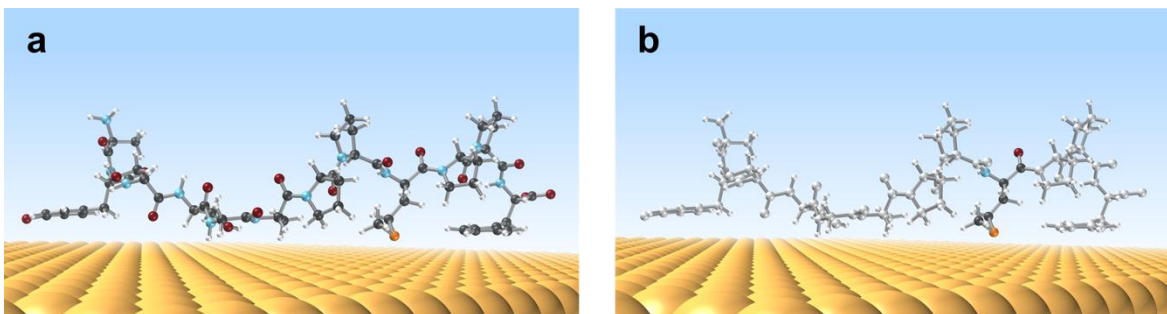
Appendix B.5 Representative Structures of Peptide Variants on Au(111) Surface



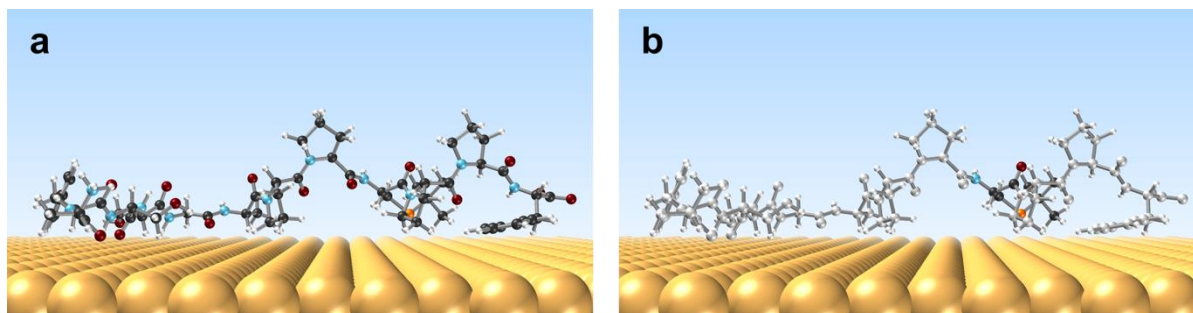
Appendix Figure 30. Representative structure of 9C peptide adsorbed on Au(111) surface according to REST-MD simulations (C, dark grey; H, light grey; N, blue; O, dark red; S, orange).



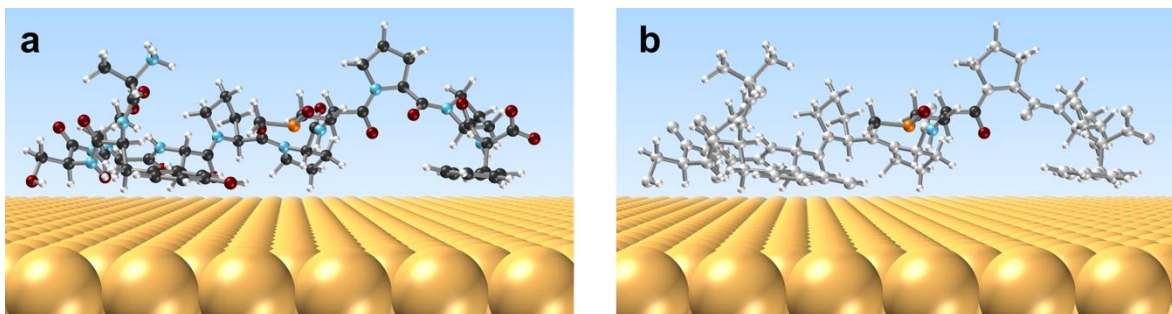
Appendix Figure 31. Representative structure of 9C^{ox}tBu peptide adsorbed on Au(111) surface according to REST-MD simulations (C, dark grey; H, light grey; N, blue; O, dark red; S, orange).



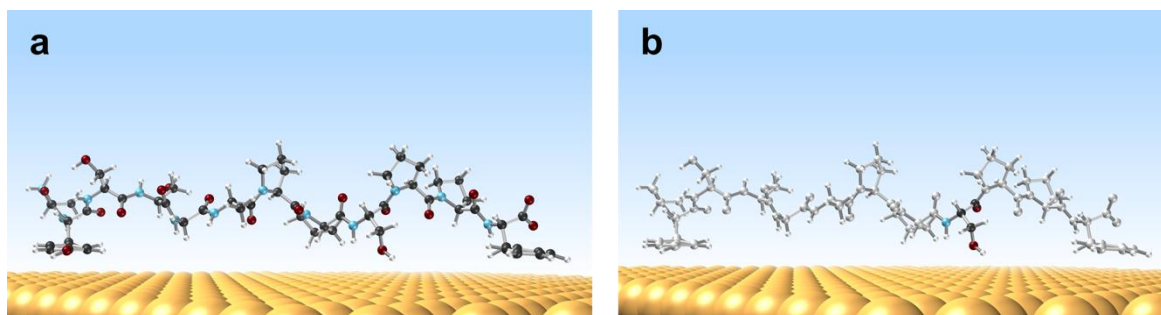
Appendix Figure 32. Representative structure of 9M peptide adsorbed on Au(111) surface according to REST-MD simulations (C, dark grey; H, light grey; N, blue; O, dark red; S, orange). In a), all atoms are colored, while in b) only the atoms of the 9th amino acid are colored for emphasis.



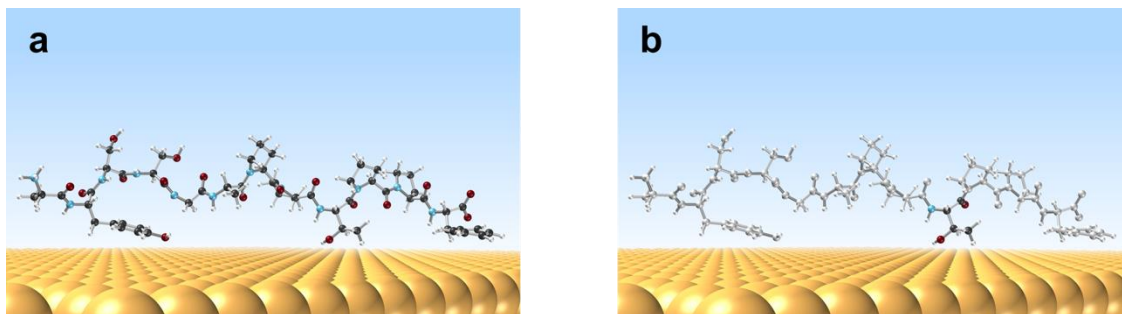
Appendix Figure 33. Representative structure of 9CtBu peptide adsorbed on Au(111) surface according to REST-MD simulations (C, dark grey; H, light grey; N, blue; O, dark red; S, orange). In a), all atoms are colored, while in b) only the atoms of the 9th amino acid are colored for emphasis.



Appendix Figure 34. Representative structure of 9M^{ox} peptide adsorbed on Au(111) surface according to EST-MD simulations (C, dark grey; H, light grey; N, blue; O, dark red; S, orange). In a), all atoms are colored, while in b) only the atoms of the 9th amino acid are colored for emphasis.

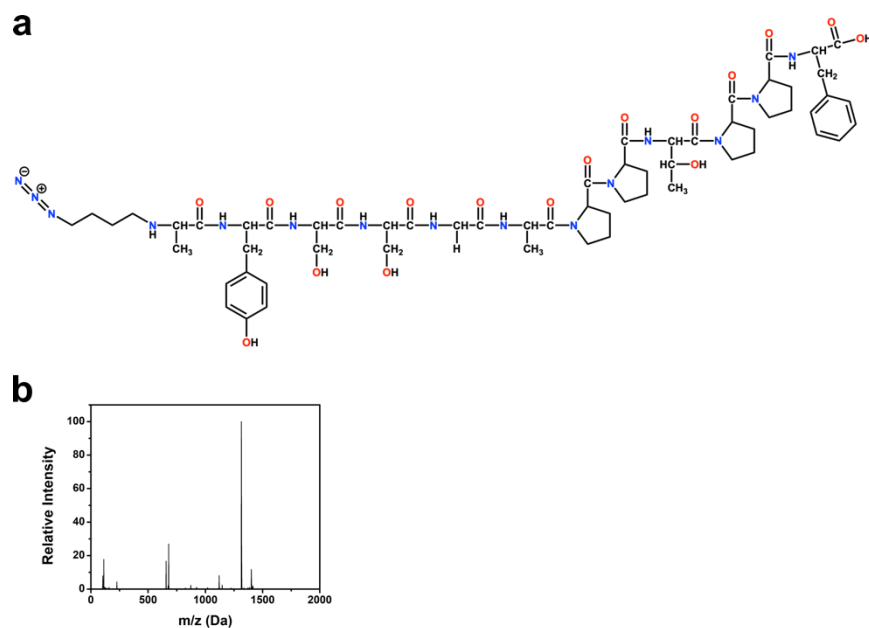


Appendix Figure 35. Representative structure of 9S peptide adsorbed on Au(111) surface according to REST-MD simulations (C, dark grey; H, light grey; N, blue; O, dark red). In a), all atoms are colored, while in b) only the atoms of the 9th amino acid are colored for emphasis.

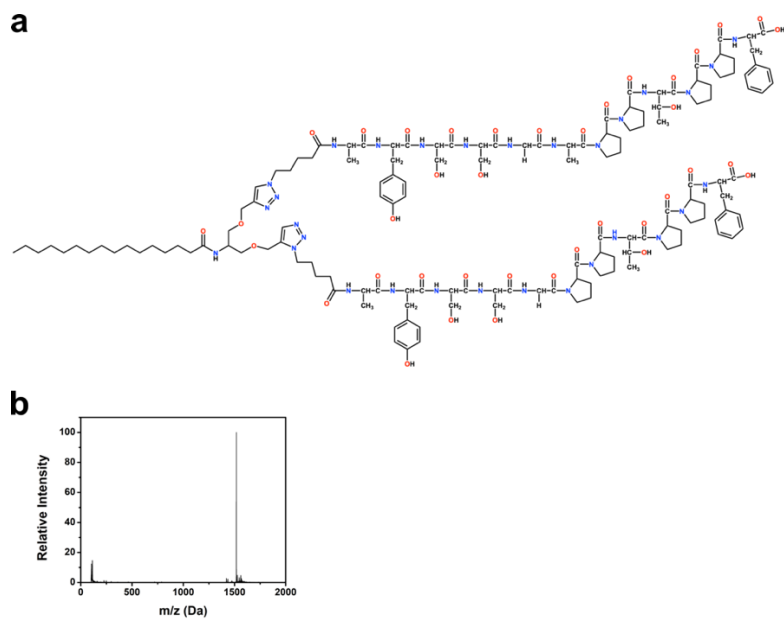


Appendix Figure 36. Representative structure of 9T peptide adsorbed on Au(111) surface according to REST-MD simulations (C, dark grey; H, light grey; N, blue; O, dark red). In a), all atoms are colored, while in b) only the atoms of the 9th amino acid are colored for emphasis.

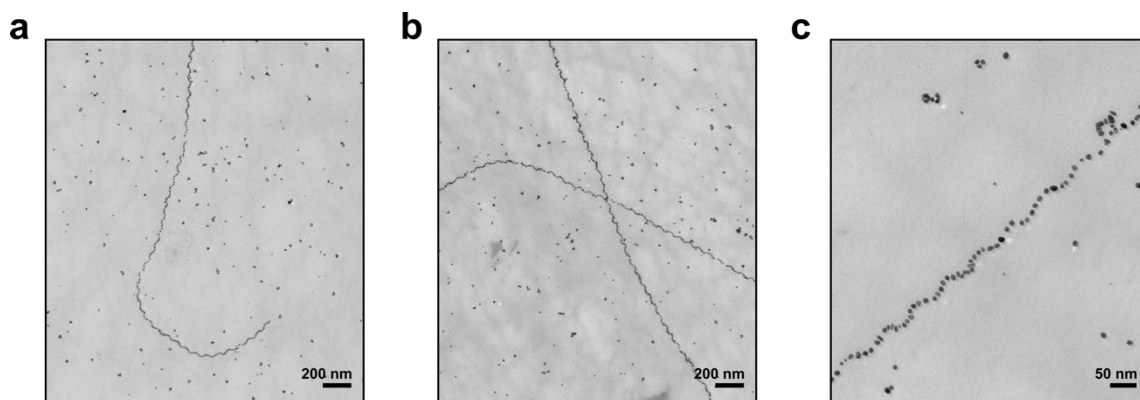
Appendix B.6 9T Peptide Conjugate Synthesis and NP Assembly Studies



Appendix Figure 37. (a) Molecular structure and (b) LC-MS mass assignment of N_3 -AYSSGAPPTPPF, $m/z = 1316$ Da ($M-H^+$); 681 Da ($M-2H^+ + HCOO^-$)/2; 657 Da ($M-2H^+$)/2.



Appendix Figure 38. (a) Molecular structure and (b) LC-MS mass assignment of C_{16} -(AYSSGAPPTPPF)₂, m/z 1518 Da ($M-2H^+$)/2.



Appendix Figure 39. Additional TEM images of Au NP assemblies produced by C_{16} -(AYSSGAPTPPF)₂.

Appendix B.7 Computational Methodology and Supporting Data

Appendix B.7.1 General Simulation Set-up

All molecular dynamics (MD) simulations were performed using the GROMACS software package (version 2021)¹¹⁰. The simulation system comprised one Au slab presenting the (111) surface in an orthorhombic periodic simulation cell with dimensions 5.8nm x 6.1nm x 6.8nm, with the z-axis perpendicular to the Au(111) surface. During all MD simulations, all Au atoms in the slab were held fixed in space during these simulations, with only the Au atom dipoles able to freely rotate. Random initial dipole positions were used throughout. Our previous tests indicated very little difference between binding obtained using a rigid substrate, vs. using a slab where all atoms are free to move.¹³⁵ Each simulation comprised one peptide, a slab of five layers of Au atoms, presenting the Au(111) surface on both facets, and approximately 6000 water molecules. Frames were saved every 1 ps unless stated otherwise.

All simulations were performed in the Canonical (NVT) ensemble at 300K, using the Nose-Hoover thermostat.^{111,136} The MD leap-frog algorithm¹³⁷ was used to integrate Newton's equations of motion using a timestep of 1 fs. The Verlet grid cut-off scheme¹³⁸ was applied for neighbor searching. The particle-mesh Ewald (PME) algorithm¹³⁹ was used for calculating electrostatic interactions. The CHARMM22* force field^{113,114} was used for the peptides, the modified TIP3P potential was used for water,¹¹⁵ and the polarizable GoIP-CHARMM force-field¹⁴⁰ was used for the Au slab.

Appendix B.7.2 Replica Exchange with Solute Tempering MD simulations

REST-MD simulations for each of the six peptides ($\text{PEP}_{\text{Au}}^{\text{A},9}$, $\text{PEP}_{\text{Au}}^{\text{S},9}$, $\text{PEP}_{\text{Au}}^{\text{C},9}$, $\text{PEP}_{\text{Au}}^{\text{T},9}$, $\text{PEP}_{\text{Au}}^{\text{CtBu},9}$, $\text{PEP}_{\text{Au}}^{\text{CoxtBu},9}$) were run in the adsorbed state at the aqueous Au(111) interface. Sixteen replicas were used with an ‘effective temperature’ window of 300-430 K following the Terakawa implementation,^{116,141} as reported previously. Note that the effective temperature is used to determine the scaling factors to modify the Hamiltonian, and does not refer to the thermal temperature of the system (which remained at 300 K throughout). The initial peptide backbone structures of the 16 replicas were taken from previous work,⁴² and captured a range of different secondary structures as well as random coil structures. The 16 values of lambda used to scale our force-field were: $\lambda_i = 0.000, 0.057, 0.114, 0.177, 0.240, 0.310, 0.382, 0.458, 0.528, 0.597, 0.692, 0.750, 0.803, 0.855, 0.930,$ and 1.000, as established in previous work. Prior to each production REST-MD simulation, the 16 initial configurations were energy minimized and then equilibrated at their target potential for 0.5 ns, with no exchange moves attempted during this period. During the production run, exchanges were attempted every 1 ps. Each REST-MD trajectory was of 15 ns duration (amounting to $16 \times 15 \text{ ns} = 0.24 \mu\text{s}$ of nominal total simulation time).

Appendix B.7.3 Clustering Analysis

Structures in each production trajectory were classified into groups (herein referred to as clusters) on the basis of similarity in the peptide backbone conformation (backbone defined as 36

atoms per peptide: amide nitrogen, alpha carbon, and carbonyl carbon per each residue), as determined by the root mean square deviation (RMSD) in those backbone atom positions. Clustering was performed over all 15001 frames of each production REST-MD trajectory using the Daura algorithm¹¹⁷ using the gmx-cluster utility with a cut-off of 2.0 Å in the RMSD of selected atomic positions. The number of frames in each cluster is used to determine the relative population of each cluster. Cross-cluster similarity (*i.e.* determining the backbone conformation similarity between clusters of different peptides) was evaluated based on the RMSD of the backbone atomic positions for the top five most populated clusters for each peptide (based on the cluster centroid structure in each case) in the pair under comparison. A matched pair of clusters was defined to have an RMSD value smaller than 2.0 Å and a near-matched pair was similarly defined to have an RMSD greater than 2.0 Å and less than or equal to 2.5 Å.

Appendix B.7.4 Residue contact analysis

To quantify residue-surface contact for each peptide in the REST-MD simulations, the vertical distance (perpendicular to the surface plane) between the topmost Au atoms on the Au(111) surface and a reference site on each residue (summarized in Table S1) was calculated for every frame in each REST-MD trajectory. The residue was considered as in contact with Au surface if the measured distance was less than or equal to the cut-off values used here (which have been determined and published elsewhere³⁹). For the non-standard residues, we used the sulfur atom as the reference site and a cut-off value of 4.5 Å for determining the surface contact. The summary of reference sites and cut-off values are shown in Table S2. The degree of residue

surface contact is expressed as a percentage of the 15001 frames for which that specific residue was determined to be in contact.

Appendix Table 2. Reference sites and cut-off values for each residue used to determine residue-surface contact.

Residue	Reference atom	Cut-off (Å)
Ala	Beta carbon	4.5
Tyr	c.o.m. of ring heavy atoms	4.0
Ser	Side-chain oxygen	4.3
Gly	Alpha carbon	4.6
Pro	Gamma carbon	4.5
Phe	c.o.m. of ring heavy atoms	4.0
Cys	Sulfur	3.5
Met	Sulfur	3.5
Thr	Side-chain oxygen	4.0
M ^{ox}	Sulfur	4.5
CtBu	Sulfur	4.5

C ^{ox} tBu	Sulfur	4.5
---------------------	--------	-----

Appendix B.7.5 Steered MD and umbrella sampling calculations

The umbrella sampling approach was used to evaluate the potential of mean force profiles of M^{ox}, CtBu and C^{ox}tBu amino acid analogues binding at the aqueous Au(111) interface. The residue binding energy profiles were calculated using similar methodology described in previous work.¹¹⁸ Both the N- and C-termini of these amino acid were capped. Steered pulling simulations were conducted to accelerate the binding progress along the direction perpendicular to the surface plane (along the z-axis) with a constant speed, thus the harmonic force constant for the steered MD and subsequent umbrella sampling simulations was set to 3000 kJ mol⁻¹ nm⁻², with a pulling rate of 0.05 nm ns⁻¹. The spatial interval between adjacent umbrella sampling windows was 0.05 nm along the z-axis (defined as the reaction coordinate), in which each umbrella sampling window was centered at each value of the reaction coordinate, and an *NVT* simulation under the applied force constant was run for 100 ns per window. The resultant PMF profiles with estimated errors were obtained using WHAM using “traj” bootstrapping method with 200 bootstraps and a default tolerance of 10⁻⁶ using the gmx-wham utility.¹¹⁹

Appendix Table 3. Amino acid binding free energies in kJ mol^{-1} (as reported in Palafox-Hernandez *et al.*, *Chem. Mater.* 2014, 26, 4960-4969). Values for CtBu, M^{ox} and C^{ox}tBu were obtained in current work.

Amino acid	Binding E.
A	-9.0
Y	-31.5
S	-10.0
G	-15.0
P	-13.0
F	-20.0
C	-32.0
M	-23.0
CtBu	-23.0
Mox	-11.6
T	-12.5
CoxtBu	-12.9

Appendix Table 4. Residue surface contact (“Contact”) expressed as a fraction between 0 and 1, and residue binding score (“Bind Sc.”, kJ mol⁻¹) defined as the contact fraction multiplied by the residue binding free energy (Table S3), for the C, M and CtBu peptide variants. Blue highlighting indicates the 9th residue.

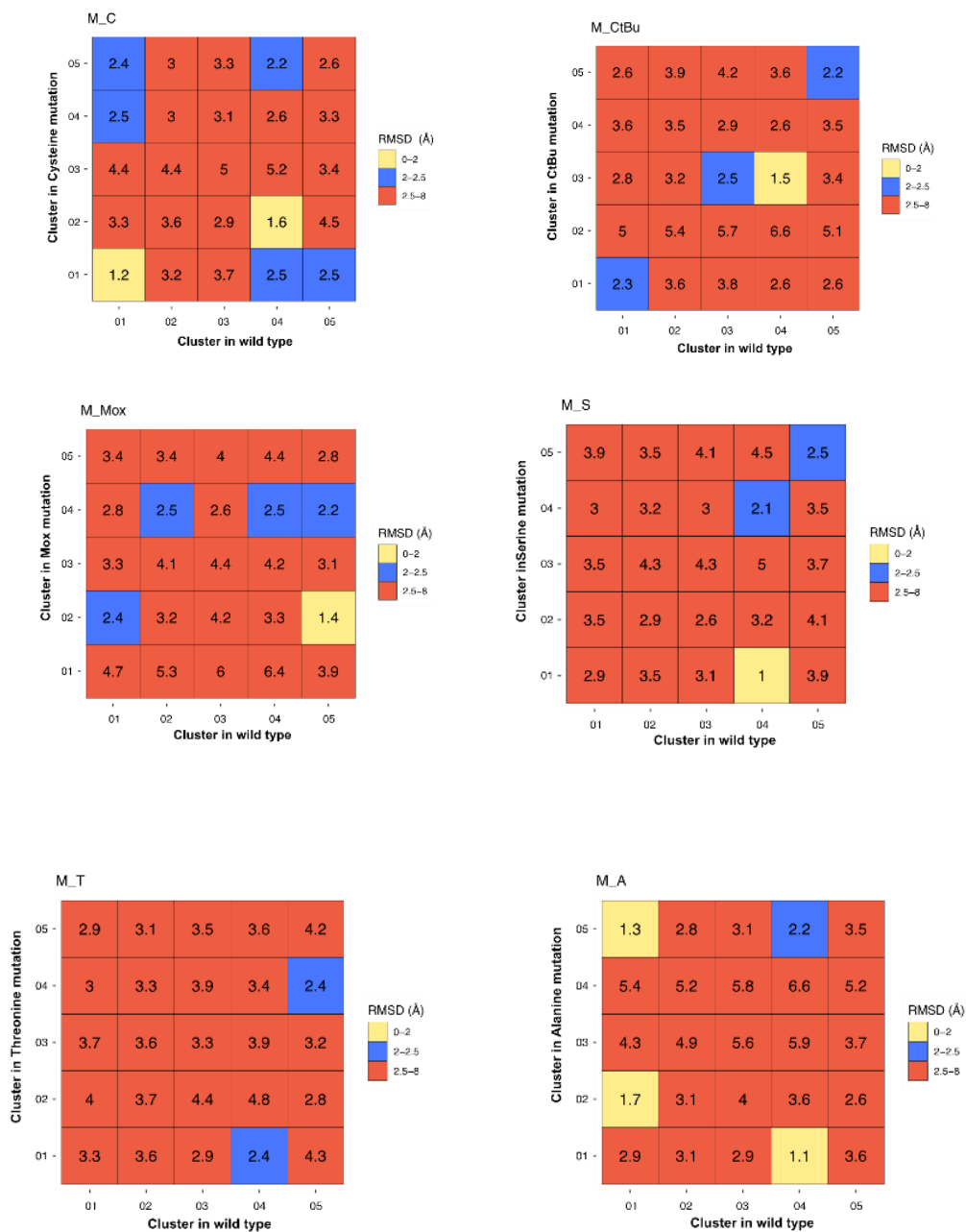
C			M			CtBu		
Residue	Contact	Bind Sc.	Residue	Contact	Bind Sc.	Residue	Contact	Bind Sc.
A	0.08	-0.72	A	0.03	-0.27	A	0.1	-0.9
Y	0.65	-20.48	Y	0.98	-30.87	Y	0.81	-25.52
S	0.35	-3.5	S	0.23	-2.3	S	0.15	-1.5
S	0.52	-5.2	S	0.58	-5.8	S	0.34	-3.4
G	0.52	-7.8	G	0.62	-9.3	G	0.56	-8.4
A	0.77	-6.93	A	0.73	-6.57	A	0.48	-4.32
P	0.41	-5.33	P	0.41	-5.33	P	0.32	-4.16
P	0.12	-1.56	P	0.17	-2.21	P	0.2	-2.6
C	0.88	-28.16	M	0.96	-22.08	CtBu	0.55	-12.65
P	0.27	-3.51	P	0.45	-5.85	P	0.6	-7.8
P	0.05	-0.65	P	0.06	-0.78	P	0.13	-1.69
F	0.76	-15.2	F	0.95	-19	F	0.73	-14.6

Appendix Table 5. Residue surface contact (“Contact”) expressed as a fraction between 0 and 1, and residue binding score (“Bind Sc.”, kJ mol⁻¹) defined as the contact fraction multiplied by the residue binding free energy (Table S3), for M^{ox}, S, and T peptide variants. Blue highlighting indicates the 9th residue.

Mox			S			T		
Residue	Contact	Bind Sc.	Residue	Contact	Bind Sc.	Residue	Contact	Bind Sc.
A	0.06	-0.54	A	0.14	-1.26	A	0.07	-0.63
Y	0.97	-30.56	Y	0.86	-27.09	Y	0.88	-27.72
S	0.23	-2.3	S	0.09	-0.9	S	0.1	-1
S	0.5	-5	S	0.36	-3.6	S	0.21	-2.1
G	0.66	-9.9	G	0.29	-4.35	G	0.23	-3.45
A	0.67	-6.03	A	0.46	-4.14	A	0.15	-1.35
P	0.44	-5.72	P	0.27	-3.51	P	0.17	-2.21
P	0.19	-2.47	P	0.26	-3.38	P	0.4	-5.2
Mox	0.58	-6.73	S	0.63	-6.3	T	0.38	-4.75
P	0.36	-4.68	P	0.25	-3.25	P	0.33	-4.29
P	0.11	-1.43	P	0.05	-0.65	P	0.17	-2.21
F	0.81	-16.2	F	0.81	-16.2	F	0.61	-12.2

Appendix Table 6. Residue surface contact (“Contact”) expressed as a fraction between 0 and 1, and residue binding score (“Bind Sc.”, kJ mol⁻¹) defined as the contact fraction multiplied by the residue binding free energy (Table S3), for A and C^{ox}tBu peptide variants. Blue highlighting indicates the 9th residue.

A			CoxtBu		
Residue	Contact	Bind Sc.	Residue	Contact	Bind Sc.
A	0.02	-0.18	A	0.13	-1.17
Y	0.97	-30.56	Y	0.77	-24.26
S	0.4	-4	S	0.17	-1.7
S	0.63	-6.3	S	0.35	-3.5
G	0.65	-9.75	G	0.38	-5.7
A	0.68	-6.12	A	0.25	-2.25
P	0.51	-6.63	P	0.2	-2.6
P	0.11	-1.43	P	0.43	-5.59
A	0.3	-2.7	CoxtBu	0.13	-1.68
P	0.3	-3.9	P	0.22	-2.86
P	0.07	-0.91	P	0.17	-2.21
F	0.92	-18.4	F	0.73	-14.6

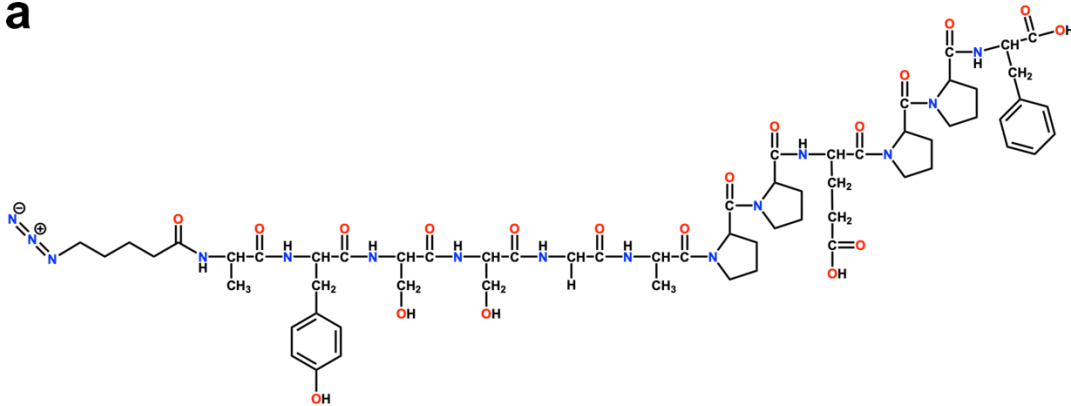


Appendix Figure 40. Results from cross-cluster comparison of cluster centroid of the top 5 clusters of the original (“wild type”) peptide and those of the peptide variants. Light colored squares indicate conformational matches and the blue squares indicate near-matched structures.

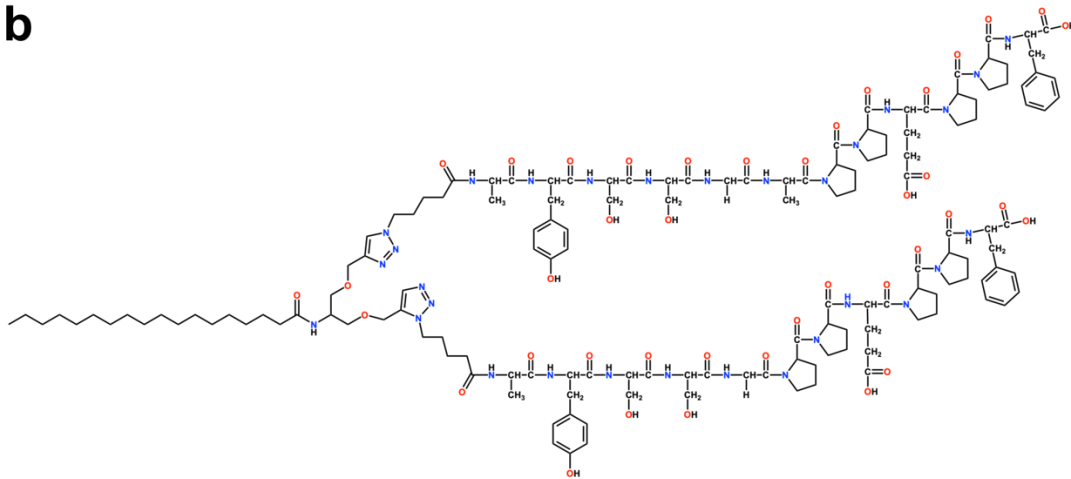
Appendix C Supporting Information for Chapter 4: “Cooperative Assembly of Nanoparticle Superstructures through Designed Electrostatic Interactions”

Appendix C.1 Peptide and Peptide Conjugate Synthesis

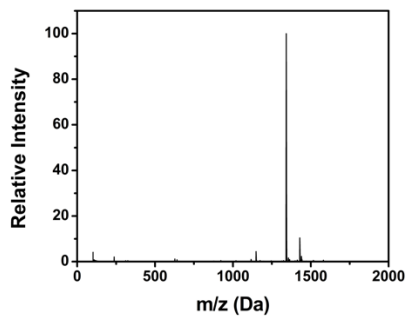
a



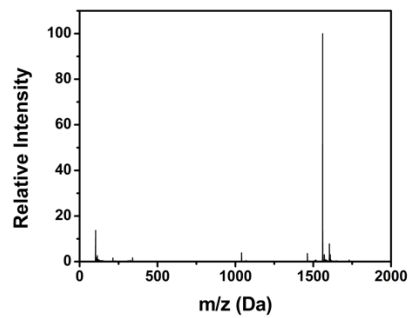
b



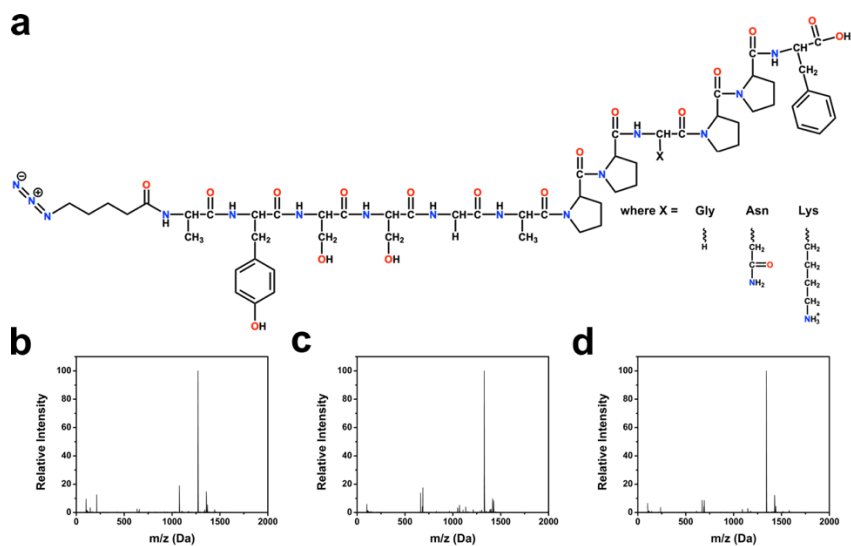
c



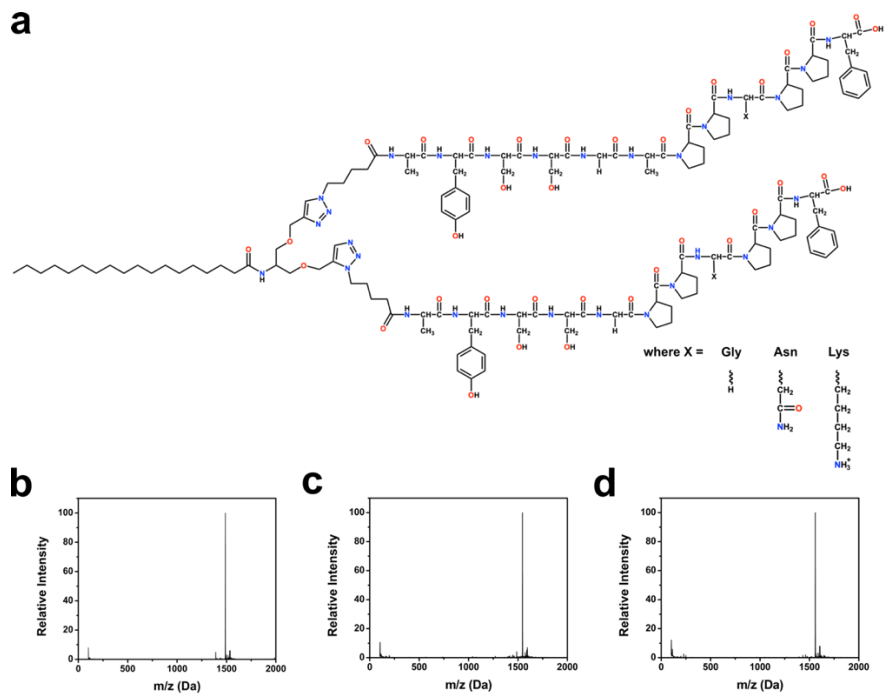
d



Appendix Figure 41. (a) Representative molecular structure of N₃-AYSSGAPPEPPF and (b) C₁₆-(AYSSGAPPEPPF)₂. LC-MS mass assignment of (c) N₃-AYSSGAPPEPPF, m/z = 1343 Da (M-H⁺); and (d) C₁₆-(AYSSGAPPEPPF)₂, m/z = 1559 Da (M-2H⁺)/2.

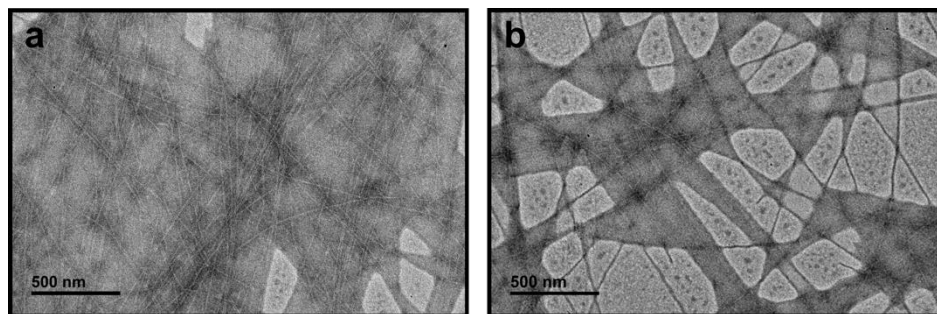


Appendix Figure 42. (a) Representative molecular structure of N₃-AYSSGAPPXPPF. LC-MS mass assignment of (b) N₃-AYSSGAPPGPPF, m/z = 1271 Da (M-H⁺); (c) N₃-AYSSGAPPNPPF, m/z = 1328 Da (M-H⁺); (d) N₃-AYSSGAPPKPPF, m/z = 1342 Da (M-H⁺).

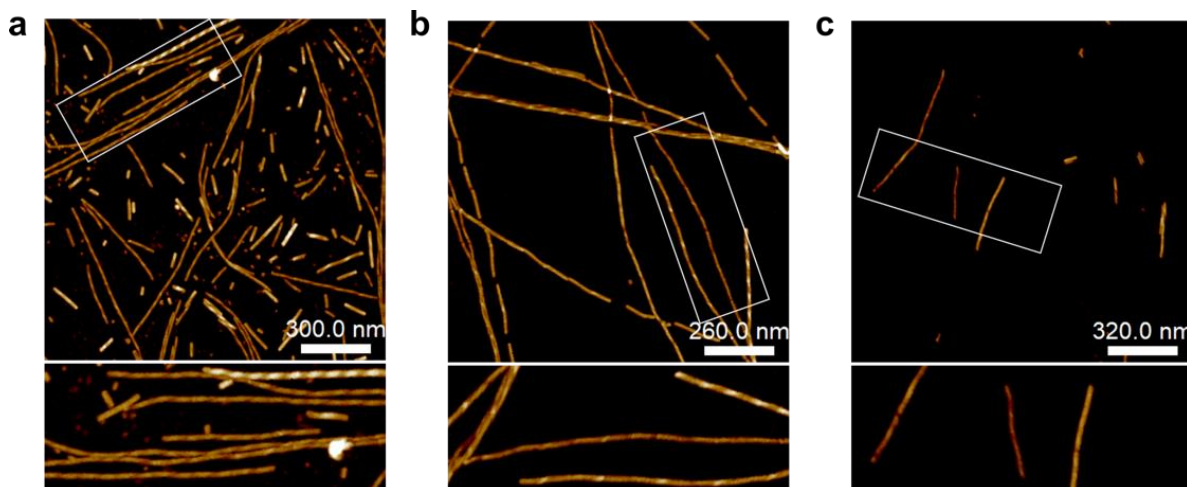


Appendix Figure 43. (a) Representative molecular structure of C_{16} -(AYSSGAPPXPPF)₂. LC-MS mass assignment of (b) C_{16} -(AYSSGAPPGPPF)₂, m/z 1487 Da ($M-2H^+$)/2; (c) C_{16} -(AYSSGAPPNPPF)₂, m/z 1544 Da ($M-2H^+$)/2; and (d) C_{16} -(AYSSGAPPKPPF)₂, m/z 1558 Da ($M-2H^+$)/2.

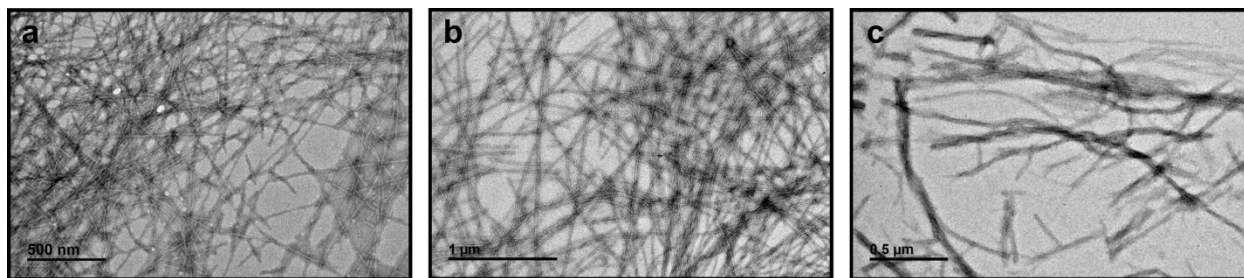
Appendix C.2 Single Component Fiber and Nanoparticle Assembly Studies



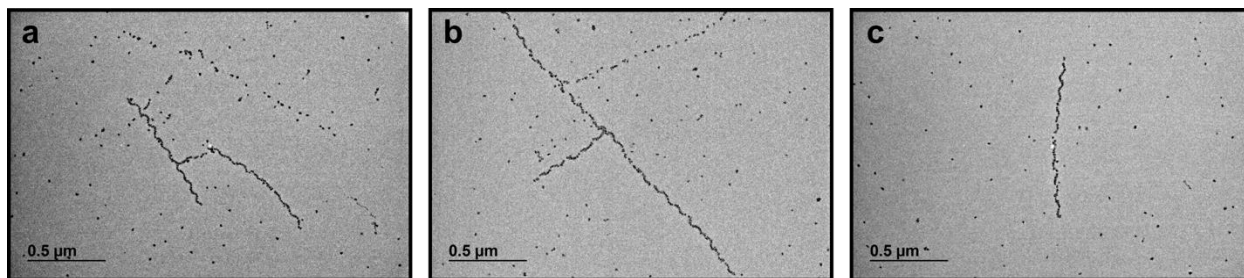
Appendix Figure 44. Negatively stained TEM images of peptide conjugate fibers produced from (a,b) C_{18} -(AYSSGAPPEPPF)₂.



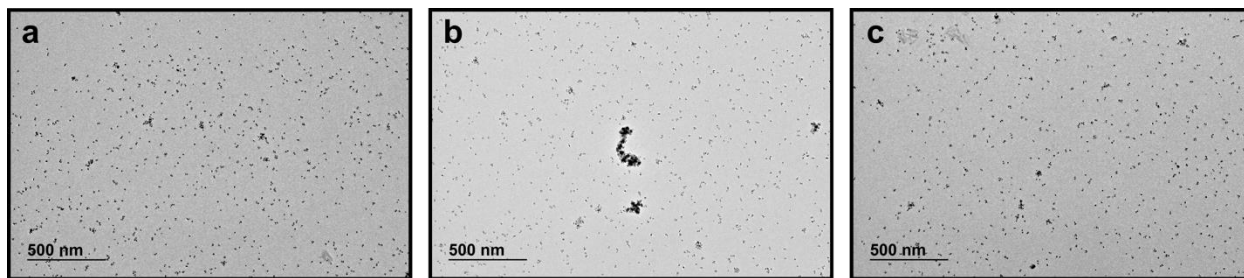
Appendix Figure 45. AFM images of peptide conjugate fibers produced from (a) C_{18} -(AYSSGAPPGPPF)₂, (b) C_{18} -(AYSSGAPPNPPF)₂, and (c) C_{18} -(AYSSGAPPKPPF)₂.



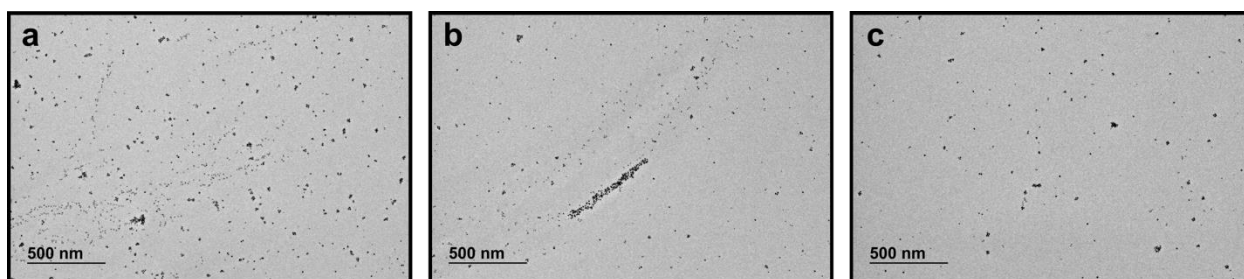
Appendix Figure 46. Negatively stained TEM images of peptide conjugate fibers produced from (a) C_{18} -(AYSSGAPPGPPF)₂, (b) C_{18} -(AYSSGAPPNPPF)₂, and (c) C_{18} -(AYSSGAPPKPPF)₂.



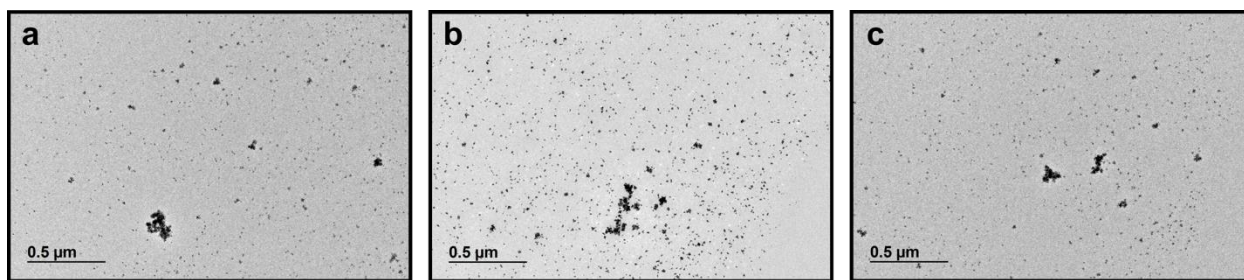
Appendix Figure 47. Additional TEM images of Au NP assemblies formed from 75 nM C_{18} -(AYSSGAPPGPPF)₂.



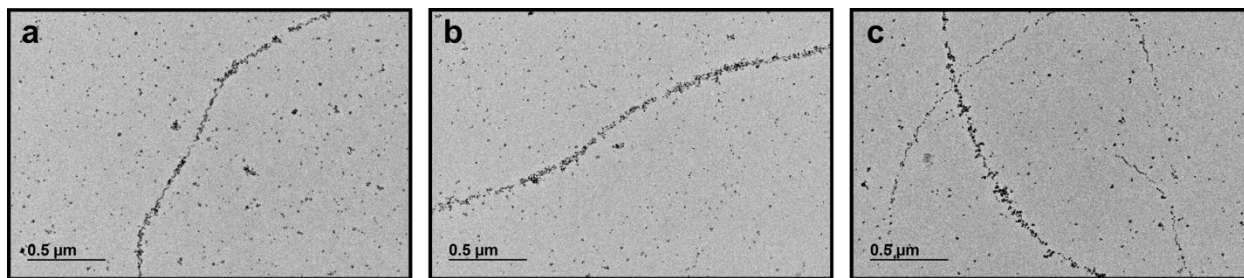
Appendix Figure 48. Additional TEM images of Au NP assemblies formed from 75 nM C_{18} -(AYSSGAPPNPPF)₂.



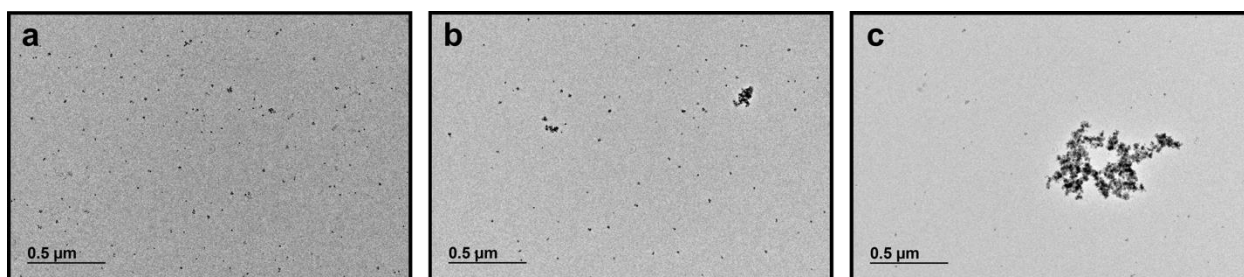
Appendix Figure 49. Additional TEM images of Au NP assemblies formed from 75 nM C_{18} -(AYSSGAPPKPPF)₂.



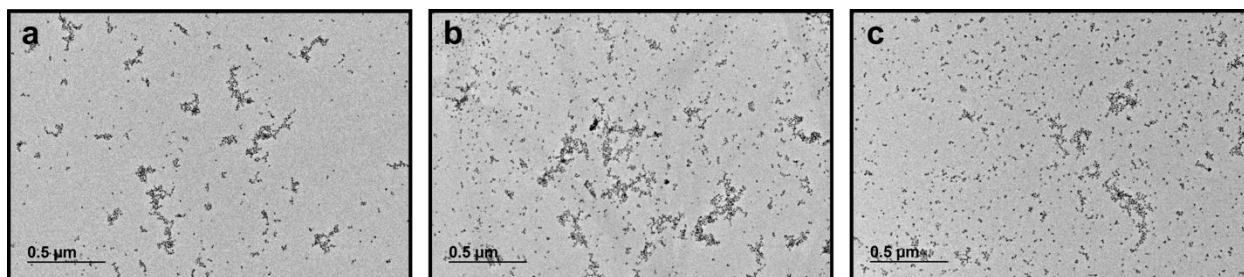
Appendix Figure 50. Additional TEM images of Au NP assemblies formed from 37.5 nM C_{18} -(AYSSGAPPEPPF)₂.



Appendix Figure 51. Additional TEM images of Au NP assemblies formed from 37.5 nM C₁₈-(AYSSGAPPGPPF)₂.



Appendix Figure 52. Additional TEM images of Au NP assemblies formed from 37.5 nM C₁₈-(AYSSGAPPNPPF)₂.

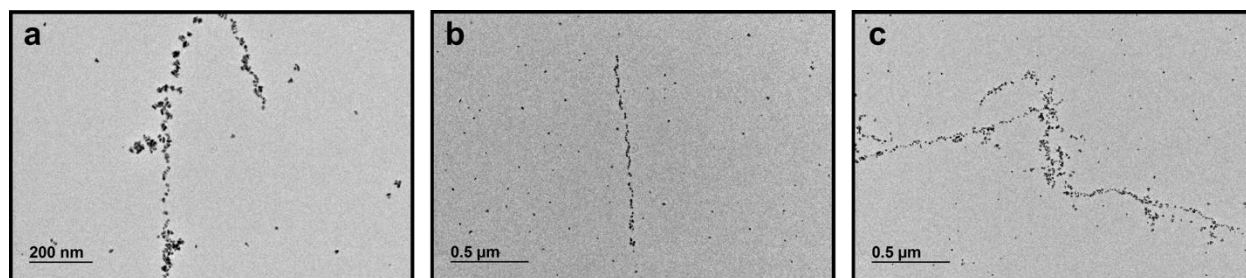


Appendix Figure 53. Additional TEM images of Au NP assemblies formed from 37.5 nM C₁₈-(AYSSGAPPKPPF)₂.

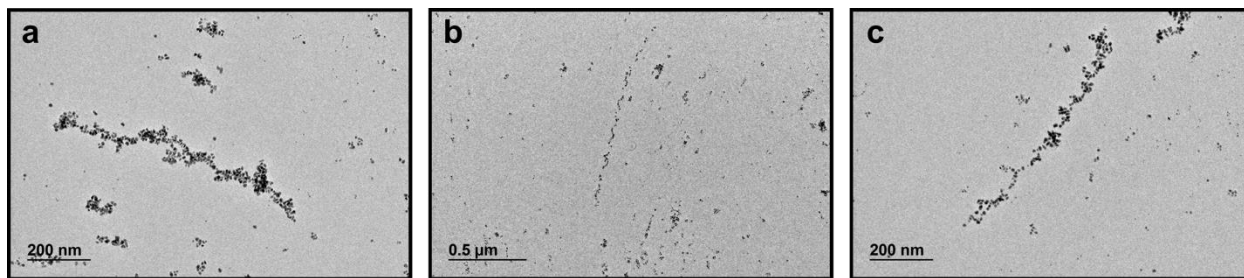
Appendix Table 7. Particle dimensions for Au NPs synthesized from 37.5 nM and 75 nM peptide conjugates.

	C_{18} -(PEP _{Au} ^{E,9}) ₂		C_{18} -(PEP _{Au} ^{G,9}) ₂		C_{18} -(PEP _{Au} ^{N,9}) ₂		C_{18} -(PEP _{Au} ^{K,9}) ₂	
	37.5 nM	75 nM	37.5 nM	75 nM	37.5 nM	75 nM	37.5 nM	75 nM
Particle Length (nm)	15.06 ± 4.6	11.04 ± 3.2	11.91 ± 3.0	15.07 ± 3.3	11.01 ± 3.0	8.86 ± 1.8	11.66 ± 1.9	8.53 ± 2.6
Particle Width (nm)	11.41 ± 2.07	9.62 ± 2.1	10.02 ± 2.4	10.70 ± 2.5	9.13 ± 2.7	7.05 ± 1.3	10.12 ± 1.9	7.19 ± 1.7

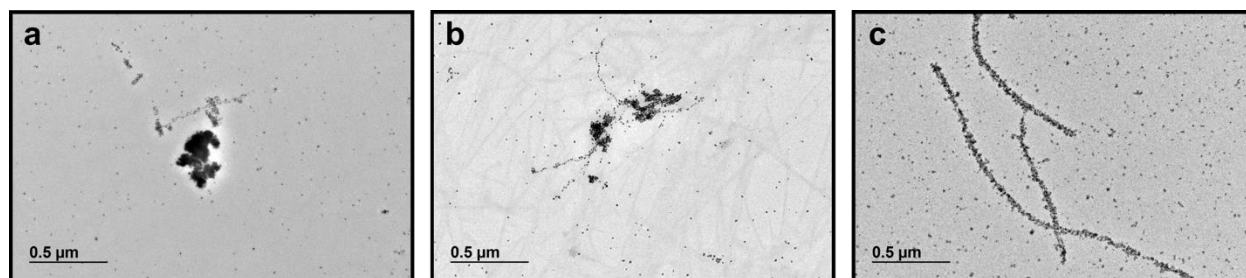
Appendix C.3 Multi-Component Fiber and Au NP Assembly Studies



Appendix Figure 54. Additional TEM images of Au NP assemblies formed from 1:1 mixture of C_{18} -(AYSSGAPPEPF)₂ and C_{18} -(AYSSGAPPGPPF)₂.



Appendix Figure 55. Additional TEM images of Au NP assemblies formed from 1:1 mixture of C_{18} -(AYSSGAPPEPPF)₂ and C_{18} -(AYSSGAPPNPPF)₂.



Appendix Figure 56. Additional TEM images of Au NP assemblies formed from 1:1 mixture of C₁₈-(AYSSGAPPEPPF)₂ and C₁₈-(AYSSGAPPKPPF)₂.

Appendix Table 8. Particle Dimensions for mixed Au NP assemblies.

	9G + 9E	9N + 9E	9K + 9E
Particle Length (nm)	13.70 ± 4.1	10.36 ± 2.7	9.51 ± 2.6
Particle Width (nm)	9.71 ± 2.7	7.83 ± 1.6	7.79 ± 1.8

References

- (1) Mann, S.; Shenton, W.; Li, M.; Connolly, S.; Fitzmaurice, D. Biologically Programmed Nanoparticle Assembly. *Adv. Mater.* **2000**, *12* (2), 147–150.
- (2) Choi, C. L.; Alivisatos, A. P. From Artificial Atoms to Nanocrystal Molecules: Preparation and Properties of More Complex Nanostructures. *Annu. Rev. Phys. Chem.* **2010**, *61* (1), 369–389.
- (3) Govorov, A. O.; Gun'ko, Y. K.; Slocik, J. M.; Gérard, V. A.; Fan, Z.; Naik, R. R. Chiral Nanoparticle Assemblies: Circular Dichroism, Plasmonic Interactions, and Exciton Effects. *J. Mater. Chem.* **2011**, *21* (42), 16806–16818.
- (4) Velev, O. D.; Gupta, S. Materials Fabricated by Micro- and Nanoparticle Assembly – The Challenging Path from Science to Engineering. *Adv. Mater.* **2009**, *21* (19), 1897–1905.
- (5) Xie, J.; Lee, J. Y.; Wang, D. I. C. Seedless, Surfactantless, High-Yield Synthesis of Branched Gold Nanocrystals in HEPES Buffer Solution. *Scopus* **2007**.
- (6) Lee, M. S.; Yee, D. W.; Ye, M.; Macfarlane, R. J. Nanoparticle Assembly as a Materials Development Tool. *J. Am. Chem. Soc.* **2022**, *144* (8), 3330–3346.
- (7) Liu, S.; Tang, Z. Nanoparticle Assemblies for Biological and Chemical Sensing. *J. Mater. Chem.* **2010**, *20* (1), 24–35.
- (8) Rao, A.; Roy, S.; Jain, V.; Pillai, P. P. Nanoparticle Self-Assembly: From Design Principles to Complex Matter to Functional Materials. *ACS Appl. Mater. Interfaces* **2022**.
- (9) V. Uljijn, R.; M. Smith, A. Designing Peptide Based Nanomaterials. *Chem. Soc. Rev.* **2008**, *37* (4), 664–675.
- (10) Zhou, Y.; Marson, R. L.; van Anders, G.; Zhu, J.; Ma, G.; Ercius, P.; Sun, K.; Yeom, B.; Glotzer, S. C.; Kotov, N. A. Biomimetic Hierarchical Assembly of Helical Supraparticles from Chiral Nanoparticles. *ACS Nano* **2016**, *10* (3), 3248–3256.
- (11) Kumar, J.; Eraña, H.; López-Martínez, E.; Claes, N.; Martín, V. F.; Solís, D. M.; Bals, S.; Cortajarena, A. L.; Castilla, J.; Liz-Marzán, L. M. Detection of Amyloid Fibrils in Parkinson's Disease Using Plasmonic Chirality. *Proc. Natl. Acad. Sci. USA* **2018**, *115* (13), 3225–3230.
- (12) Maude, S.; Tai, L. R.; Davies, R. P. W.; Liu, B.; Harris, S. A.; Kocienski, P. J.; Aggeli, A. Peptide Synthesis and Self-Assembly. In *Peptide-Based Materials*; Deming, T., Ed.; Springer: Berlin, Heidelberg, 2012; pp 27–69.

- (13) Lee, H.-E.; Ahn, H.-Y.; Lee, J.; Nam, K. T. Biomolecule-Enabled Chiral Assembly of Plasmonic Nanostructures. *ChemNanoMat* **2017**, *3* (10), 685–697.
- (14) Zhu, J.; Avakyan, N.; Kakkis, A.; Hoffnagle, A. M.; Han, K.; Li, Y.; Zhang, Z.; Choi, T. S.; Na, Y.; Yu, C.-J.; Tezcan, F. A. Protein Assembly by Design. *Chem. Rev.* **2021**, *121* (22), 13701–13796.
- (15) Narwani, T. J.; Santuz, H.; Shinada, N.; Melarkode Vattekatte, A.; Ghouzam, Y.; Srinivasan, N.; Gelly, J.-C.; de Brevern, A. G. Recent Advances on Polyproline II. *Amino Acids* **2017**, *49* (4), 705–713.
- (16) Fujiwara, K.; Toda, H.; Ikeguchi, M. Dependence of α -Helical and β -Sheet Amino Acid Propensities on the Overall Protein Fold Type. *BMC Struct. Biol.* **2012**, *12* (1), 18.
- (17) Kaiser, E. T.; Kézdy, F. J. Secondary Structures of Proteins and Peptides in Amphiphilic Environments. (A Review). *Proc. Natl. Acad. Sci. USA* **1983**, *80* (4), 1137–1143.
- (18) Aggeli, A.; Nyrkova, I. A.; Bell, M.; Harding, R.; Carrick, L.; McLeish, T. C. B.; Semenov, A. N.; Boden, N. Hierarchical Self-Assembly of Chiral Rod-like Molecules as a Model for Peptide β -Sheet Tapes, Ribbons, Fibrils, and Fibers. *Proc. Natl. Acad. Sci. USA* **2001**, *98* (21), 11857–11862.
- (19) Yamada, K.; Ihara, H.; Ide, T.; Fukumoto, T.; Hirayama, C. Formation of Helical Super Structure from Single-Walled Bilayers by Amphiphiles with Oligo-l-Glutamic Acid-Head Group. *Chem. Lett.* **1984**, *13* (10), 1713–1716.
- (20) Dasgupta, A.; Das, D. Designer Peptide Amphiphiles: Self-Assembly to Applications. *Langmuir* **2019**, *35* (33), 10704–10724.
- (21) Han, Y.; Noguchi, H.; Sakaguchi, K.; Uosaki, K. Formation Process and Solvent-Dependent Structure of a Polyproline Self-Assembled Monolayer on a Gold Surface. *Langmuir* **2011**, *27* (19), 11951–11957.
- (22) Adzhubei, A. A.; Sternberg, M. J. E.; Makarov, A. A. Polyproline-II Helix in Proteins: Structure and Function. *J. Mol. Biol.* **2013**, *425* (12), 2100–2132.
- (23) O'Brien, K. T.; Mooney, C.; Lopez, C.; Pollastri, G.; Shields, D. C. Prediction of Polyproline II Secondary Structure Propensity in Proteins. *R. Soc. Open Sci.* **2020**, *7* (1), 191239.
- (24) Hunter, G. K.; Goldberg, H. A. Modulation of Crystal Formation by Bone Phosphoproteins: Role of Glutamic Acid-Rich Sequences in the Nucleation of Hydroxyapatite by Bone Sialoprotein. *Biochem J* **1994**, *302* (Pt 1) (Pt 1), 175–179.
- (25) Bond, G. M.; Richman, R. H.; McNaughton, W. P. Mimicry of Natural Material Designs and Processes. *JMEP* **1995**, *4* (3), 334–345.

- (26) Bradt, J.-H.; Mertig, M.; Teresiak, A.; Pompe, W. Biomimetic Mineralization of Collagen by Combined Fibril Assembly and Calcium Phosphate Formation. *Chem. Mater.* **1999**, *11* (10), 2694–2701.
- (27) Hendricks, M. P.; Sato, K.; Palmer, L. C.; Stupp, S. I. Supramolecular Assembly of Peptide Amphiphiles. *Acc. Chem. Res.* **2017**, *50* (10), 2440–2448.
- (28) Hartgerink, J. D.; Beniash, E.; Stupp, S. I. Self-Assembly and Mineralization of Peptide-Amphiphile Nanofibers. *Science* **2001**, *294* (5547), 1684–1688.
- (29) Lee, S. S.; Fyrner, T.; Chen, F.; Álvarez, Z.; Sleep, E.; Chun, D. S.; Weiner, J. A.; Cook, R. W.; Freshman, R. D.; Schallmo, M. S.; Katchko, K. M.; Schneider, A. D.; Smith, J. T.; Yun, C.; Singh, G.; Hashmi, S. Z.; McClendon, M. T.; Yu, Z.; Stock, S. R.; Hsu, W. K.; Hsu, E. L.; Stupp, S. I. Sulfated Glycopeptide Nanostructures for Multipotent Protein Activation. *Nature Nanotech.* **2017**, *12* (8), 821–829.
- (30) Morgan, C. E.; Dombrowski, A. W.; Rubert Pérez, C. M.; Bahnson, E. S. M.; Tsihlis, N. D.; Jiang, W.; Jiang, Q.; Vercammen, J. M.; Prakash, V. S.; Pritts, T. A.; Stupp, S. I.; Kibbe, M. R. Tissue-Factor Targeted Peptide Amphiphile Nanofibers as an Injectable Therapy To Control Hemorrhage. *ACS Nano* **2016**, *10* (1), 899–909.
- (31) Wu, C.-H.; Liu, I.-J.; Lu, R.-M.; Wu, H.-C. Advancement and Applications of Peptide Phage Display Technology in Biomedical Science. *J. Biomed. Sci.* **2016**, *23* (1), 8.
- (32) Chen, C.-L.; Rosi, N. L. Peptide-Based Methods for the Preparation of Nanostructured Inorganic Materials. *Angew. Chem., Int. Ed.* **2010**, *49* (11), 1924–1942.
- (33) Walsh, T. R.; Knecht, M. R. Biointerface Structural Effects on the Properties and Applications of Bioinspired Peptide-Based Nanomaterials. *Chem. Rev.* **2017**, *117* (20), 12641–12704.
- (34) Whaley, S. R.; English, D. S.; Hu, E. L.; Barbara, P. F.; Belcher, A. M. Selection of Peptides with Semiconductor Binding Specificity for Directed Nanocrystal Assembly. *Nature* **2000**, *405* (6787), 665–668.
- (35) B. Pandey, R.; Heinz, H.; Feng, J.; L. Farmer, B.; M. Slocik, J.; F. Drummy, L.; R. Naik, R. Adsorption of Peptides (A3, Flg, Pd2, Pd4) on Gold and Palladium Surfaces by a Coarse-Grained Monte Carlo Simulation. *Phys. Chem. Chem. Phys.* **2009**, *11* (12), 1989–2001.
- (36) Tamerler, C.; Duman, M.; Oren, E. E.; Gungormus, M.; Xiong, X.; Kacar, T.; Parviz, B. A.; Sarikaya, M. Materials Specificity and Directed Assembly of a Gold-Binding Peptide. *Small* **2006**, *2* (11), 1372–1378.
- (37) Naik, R. R.; Stringer, S. J.; Agarwal, G.; Jones, S. E.; Stone, M. O. Biomimetic Synthesis and Patterning of Silver Nanoparticles. *Nature Mater.* **2002**, *1* (3), 169–172.

- (38) Slocik, J. M.; Stone, M. O.; Naik, R. R. Synthesis of Gold Nanoparticles Using Multifunctional Peptides. *Small* **2005**, *1* (11), 1048–1052.
- (39) Tang, Z.; Palafox-Hernandez, J. P.; Law, W.-C.; Hughes, Z. E.; Swihart, M. T.; Prasad, P. N.; Knecht, M. R.; Walsh, T. R. Biomolecular Recognition Principles for Bionanocombinatorics: An Integrated Approach to Elucidate Enthalpic and Entropic Factors. *ACS Nano* **2013**, *7* (11), 9632–9646.
- (40) Palafox-Hernandez, J. P.; Tang, Z.; Hughes, Z. E.; Li, Y.; Swihart, M. T.; Prasad, P. N.; Walsh, T. R.; Knecht, M. R. Comparative Study of Materials-Binding Peptide Interactions with Gold and Silver Surfaces and Nanostructures: A Thermodynamic Basis for Biological Selectivity of Inorganic Materials. *Chem. Mater.* **2014**, *26* (17), 4960–4969.
- (41) Nguyen, M. A.; Hughes, Z. E.; Liu, Y.; Li, Y.; Swihart, M. T.; Knecht, M. R.; Walsh, T. R. Peptide-Mediated Growth and Dispersion of Au Nanoparticles in Water via Sequence Engineering. *J. Phys. Chem. C* **2018**, *122* (21), 11532–11542.
- (42) Mokashi-Punekar, S.; Walsh, T. R.; Rosi, N. L. Tuning the Structure and Chiroptical Properties of Gold Nanoparticle Single Helices via Peptide Sequence Variation. *J. Am. Chem. Soc.* **2019**, *141* (39), 15710–15716.
- (43) Bedford, N. M.; Hughes, Z. E.; Tang, Z.; Li, Y.; Briggs, B. D.; Ren, Y.; Swihart, M. T.; Petkov, V. G.; Naik, R. R.; Knecht, M. R.; Walsh, T. R. Sequence-Dependent Structure/Function Relationships of Catalytic Peptide-Enabled Gold Nanoparticles Generated under Ambient Synthetic Conditions. *J. Am. Chem. Soc.* **2016**, *138* (2), 540–548.
- (44) Palmer, L. C.; Stupp, S. I. Molecular Self-Assembly into One-Dimensional Nanostructures. *Acc. Chem. Res.* **2008**, *41* (12), 1674–1684.
- (45) Cui, H.; Webber, M. J.; Stupp, S. I. Self-Assembly of Peptide Amphiphiles: From Molecules to Nanostructures to Biomaterials. *Pept. Sci.* **2010**, *94* (1), 1–18.
- (46) Slocik, J. M.; Zabinski Jr., J. S.; Phillips, D. M.; Naik, R. R. Colorimetric Response of Peptide-Functionalized Gold Nanoparticles to Metal Ions. *Small* **2008**, *4* (5), 548–551.
- (47) Si, S.; Bhattacharjee, R. R.; Banerjee, A.; Mandal, T. K. A Mechanistic and Kinetic Study of the Formation of Metal Nanoparticles by Using Synthetic Tyrosine-Based Oligopeptides. *Chem. Eur. J.* **2006**, *12* (4), 1256–1265.
- (48) Habib, A.; Tabata, M.; Wu, Y. G. Formation of Gold Nanoparticles by Good's Buffers. *BCSJ* **2005**, *78* (2), 262–269.
- (49) Chen, C.-L.; Zhang, P.; Rosi, N. L. A New Peptide-Based Method for the Design and Synthesis of Nanoparticle Superstructures: Construction of Highly Ordered Gold Nanoparticle Double Helices. *J. Am. Chem. Soc.* **2008**, *130* (41), 13555–13557.

- (50) Paramonov, S. E.; Jun, H.-W.; Hartgerink, J. D. Self-Assembly of Peptide–Amphiphile Nanofibers: The Roles of Hydrogen Bonding and Amphiphilic Packing. *J. Am. Chem. Soc.* **2006**, *128* (22), 7291–7298.
- (51) Surewicz, W. K.; Mantsch, H. H.; Chapman, D. Determination of Protein Secondary Structure by Fourier Transform Infrared Spectroscopy: A Critical Assessment. *Biochemistry* **1993**, *32* (2), 389–394.
- (52) Georget, D. M. R.; Belton, P. S. Effects of Temperature and Water Content on the Secondary Structure of Wheat Gluten Studied by FTIR Spectroscopy. *Biomacromolecules* **2006**, *7* (2), 469–475.
- (53) Minor, D. L.; Kim, P. S. Measurement of the β -Sheet-Forming Propensities of Amino Acids. *Nature* **1994**, *367* (6464), 660–663.
- (54) Nowick, J. S.; Insaf, S. The Propensities of Amino Acids To Form Parallel β -Sheets. *J. Am. Chem. Soc.* **1997**, *119* (45), 10903–10908.
- (55) Street, A. G.; Mayo, S. L. Intrinsic β -Sheet Propensities Result from van Der Waals Interactions between Side Chains and the Local Backbone. *Proc. Natl. Acad. Sci. USA* **1999**, *96* (16), 9074–9076.
- (56) Bhattacharjee, N.; Biswas, P. Position-Specific Propensities of Amino Acids in the β -Strand. *BMC Struct. Biol.* **2010**, *10*, 29.
- (57) Weatherford, D. W.; Salemme, F. R. Conformations of Twisted Parallel Beta-Sheets and the Origin of Chirality in Protein Structures. *Proc. Natl. Acad. Sci. USA* **1979**, *76* (1), 19–23.
- (58) Song, C.; Zhao, G.; Zhang, P.; Rosi, N. L. Expedient Synthesis and Assembly of Sub-100 Nm Hollow Spherical Gold Nanoparticle Superstructures. *J. Am. Chem. Soc.* **2010**, *132* (40), 14033–14035.
- (59) Hwang, L.; Chen, C.-L.; Rosi, N. L. Preparation of 1-D Nanoparticle Superstructures with Tailorable Thicknesses Using Gold-Binding Peptide Conjugates. *Chem. Commun.* **2011**, *47* (1), 185–187.
- (60) Hwang, L.; Zhao, G.; Zhang, P.; Rosi, N. L. Size-Controlled Peptide-Directed Synthesis of Hollow Spherical Gold Nanoparticle Superstructures. *Small* **2011**, *7* (14), 1939–1942.
- (61) Merg, A. D.; Slocik, J.; Blaber, M. G.; Schatz, G. C.; Naik, R.; Rosi, N. L. Adjusting the Metrics of 1-D Helical Gold Nanoparticle Superstructures Using Multivalent Peptide Conjugates. *Langmuir* **2015**, *31* (34), 9492–9501.
- (62) Song, C.; Blaber, M. G.; Zhao, G.; Zhang, P.; Fry, H. C.; Schatz, G. C.; Rosi, N. L. Tailorable Plasmonic Circular Dichroism Properties of Helical Nanoparticle Superstructures. *Nano Lett.* **2013**, *13* (7), 3256–3261.

- (63) Fan, Z.; Govorov, A. O. Plasmonic Circular Dichroism of Chiral Metal Nanoparticle Assemblies. *Nano Lett.* **2010**, *10* (7), 2580–2587.
- (64) Fan, Z.; Govorov, A. O. Helical Metal Nanoparticle Assemblies with Defects: Plasmonic Chirality and Circular Dichroism. *J. Phys. Chem. C* **2011**, *115* (27), 13254–13261.
- (65) Zhang, C.; Song, C.; Fry, H. C.; Rosi, N. L. Peptide Conjugates for Directing the Morphology and Assembly of 1D Nanoparticle Superstructures. *Chem. Eur. J.* **2014**, *20* (4), 941–945.
- (66) Huisgen, R. 1,3-Dipolare Cycloadditionen Rückschau und Ausblick. *Angew. Chem., Int. Ed.* **1963**, *75* (13), 604–637.
- (67) Rostovtsev, V. V.; Green, L. G.; Fokin, V. V.; Sharpless, K. B. A Stepwise Huisgen Cycloaddition Process: Copper(I)-Catalyzed Regioselective “Ligation” of Azides and Terminal Alkynes. *Angew. Chem., Int. Ed.* **2002**, *41* (14), 2596–2599.
- (68) Merg, A. D.; Boatz, J. C.; Mandal, A.; Zhao, G.; Mokashi-Punekar, S.; Liu, C.; Wang, X.; Zhang, P.; van der Wel, P. C. A.; Rosi, N. L. Peptide-Directed Assembly of Single-Helical Gold Nanoparticle Superstructures Exhibiting Intense Chiroptical Activity. *J. Am. Chem. Soc.* **2016**, *138* (41), 13655–13663.
- (69) Lai, C.-T.; Rosi, N. L.; Schatz, G. C. All-Atom Molecular Dynamics Simulations of Peptide Amphiphile Assemblies That Spontaneously Form Twisted and Helical Ribbon Structures. *J. Phys. Chem. Lett.* **2017**, *8* (10), 2170–2174.
- (70) Mokashi-Punekar, S.; Merg, A. D.; Rosi, N. L. Systematic Adjustment of Pitch and Particle Dimensions within a Family of Chiral Plasmonic Gold Nanoparticle Single Helices. *J. Am. Chem. Soc.* **2017**, *139* (42), 15043–15048.
- (71) Mokashi-Punekar, S.; Brooks, S. C.; Hogan, C. D.; Rosi, N. L. Leveraging Peptide Sequence Modification to Promote Assembly of Chiral Helical Gold Nanoparticle Superstructures. *Biochemistry* **2020**, *60* (13), 1044–1049.
- (72) Alivisatos, A. P. Semiconductor Clusters, Nanocrystals, and Quantum Dots. *Science* **1996**, *271* (5251), 933–937.
- (73) Nie, Z.; Petukhova, A.; Kumacheva, E. Properties and Emerging Applications of Self-Assembled Structures Made from Inorganic Nanoparticles. *Nat. Nanotechnol.* **2010**, *5* (1), 15–25.
- (74) Xu, L.; Ma, W.; Wang, L.; Xu, C.; Kuang, H.; Kotov, N. A. Nanoparticle Assemblies: Dimensional Transformation of Nanomaterials and Scalability. *Chem. Soc. Rev.* **2013**, *42* (7), 3114–3126.
- (75) Laramy, C. R.; O’Brien, M. N.; Mirkin, C. A. Crystal Engineering with DNA. *Nat. Rev. Mater.* **2019**, *4* (3), 201–224.

- (76) Ben-Moshe, A.; Maoz, B. M.; Govorov, A. O.; Markovich, G. Chirality and Chiroptical Effects in Inorganic Nanocrystal Systems with Plasmon and Exciton Resonances. *Chem. Soc. Rev.* **2013**, *42* (16), 7028–7041.
- (77) Mokashi-Punekar, S.; Zhou, Y.; Brooks, S. C.; Rosi, N. L. Construction of Chiral, Helical Nanoparticle Superstructures: Progress and Prospects. *Adv. Mater.* *32* (41), 1905975.
- (78) Pendry, J. B. A Chiral Route to Negative Refraction. *Science* **2004**, *306* (5700), 1353–1355.
- (79) Ma, W.; Xu, L.; de Moura, A. F.; Wu, X.; Kuang, H.; Xu, C.; Kotov, N. A. Chiral Inorganic Nanostructures. *Chem. Rev.* **2017**, *117* (12), 8041–8093.
- (80) Fan, Z.; Govorov, A. O. Helical Metal Nanoparticle Assemblies with Defects: Plasmonic Chirality and Circular Dichroism. *J. Phys. Chem. C* **2011**, *115* (27), 13254–13261.
- (81) Chen, C.-L.; Rosi, N. L. Preparation of Unique 1-D Nanoparticle Superstructures and Tailoring Their Structural Features. *J. Am. Chem. Soc.* **2010**, *132* (20), 6902–6903.
- (82) Song, C.; Wang, Y.; Rosi, N. L. Peptide-Directed Synthesis and Assembly of Hollow Spherical CoPt Nanoparticle Superstructures. *Angew. Chem., Int. Ed.* **2013**, *52* (14), 3993–3995.
- (83) Song, C.; Blaber, M. G.; Zhao, G.; Zhang, P.; Fry, H. C.; Schatz, G. C.; Rosi, N. L. Tailorable Plasmonic Circular Dichroism Properties of Helical Nanoparticle Superstructures. *Nano Lett.* **2013**, *13* (7), 3256–3261.
- (84) Merg, A. D.; Boatz, J. C.; Mandal, A.; Zhao, G.; Mokashi-Punekar, S.; Liu, C.; Wang, X.; Zhang, P.; van der Wel, P. C. A.; Rosi, N. L. Peptide-Directed Assembly of Single-Helical Gold Nanoparticle Superstructures Exhibiting Intense Chiroptical Activity. *J. Am. Chem. Soc.* **2016**, *138* (41), 13655–13663.
- (85) Mokashi-Punekar, S.; Rosi, N. L. Deliberate Introduction of Particle Anisotropy in Helical Gold Nanoparticle Superstructures. *Part. Part. Syst. Charact.* **2019**, *36* (5), 1800504.
- (86) Mokashi-Punekar, S.; Merg, A. D.; Rosi, N. L. Systematic Adjustment of Pitch and Particle Dimensions within a Family of Chiral Plasmonic Gold Nanoparticle Single Helices. *J. Am. Chem. Soc.* **2017**, *139* (42), 15043–15048.
- (87) Hartgerink, J. D.; Beniash, E.; Stupp, S. I. Self-Assembly and Mineralization of Peptide-Amphiphile Nanofibers. *Science* **2001**, *294* (5547), 1684–1688.
- (88) Heinz, H.; Farmer, B. L.; Pandey, R. B.; Slocik, J. M.; Patnaik, S. S.; Pachter, R.; Naik, R. R. Nature of Molecular Interactions of Peptides with Gold, Palladium, and Pd–Au Bimetal Surfaces in Aqueous Solution. *J. Am. Chem. Soc.* **2009**, *131* (28), 9704–9714.

- (89) Cui, H.; Cheetham, A. G.; Pashuck, E. T.; Stupp, S. I. Amino Acid Sequence in Constitutionally Isomeric Tetrapeptide Amphiphiles Dictates Architecture of One-Dimensional Nanostructures. *J. Am. Chem. Soc.* **2014**, *136* (35), 12461–12468.
- (90) Wang, S.-T.; Lin, Y.; Spencer, R. K.; Thomas, M. R.; Nguyen, A. I.; Amdursky, N.; Pashuck, E. T.; Skaalure, S. C.; Song, C. Y.; Parmar, P. A.; Morgan, R. M.; Ercius, P.; Aloni, S.; Zuckermann, R. N.; Stevens, M. M. Sequence-Dependent Self-Assembly and Structural Diversity of Islet Amyloid Polypeptide-Derived β -Sheet Fibrils. *ACS Nano* **2017**, *11* (9), 8579–8589.
- (91) Moyer, T. J.; Cui, H.; Stupp, S. I. Tuning Nanostructure Dimensions with Supramolecular Twisting. *J. Phys. Chem. B* **2013**, *117* (16), 4604–4610.
- (92) Heinz, H.; Farmer, B. L.; Pandey, R. B.; Slocik, J. M.; Patnaik, S. S.; Pachter, R.; Naik, R. R. Nature of Molecular Interactions of Peptides with Gold, Palladium, and Pd–Au Bimetal Surfaces in Aqueous Solution. *J. Am. Chem. Soc.* **2009**, *131* (28), 9704–9714.
- (93) Zanna, N.; Milli, L.; Del Secco, B.; Tomasini, C. Factors Affecting the Stabilization of Polyproline II Helices in a Hydrophobic Environment. *Org. Lett.* **2016**, *18* (7), 1662–1665.
- (94) Barth, A. Infrared Spectroscopy of Proteins. *Biochim. Biophys. Acta. Bioenerg.* **2007**, *1767* (9), 1073–1101.
- (95) Philp, D.; Stoddart, J. F. Self-Assembly in Natural and Unnatural Systems. *Angew. Chem., Int. Ed.* **1996**, *35* (11), 1154–1196.
- (96) Matson, J. B.; Zha, R. H.; Stupp, S. I. Peptide Self-Assembly for Crafting Functional Biological Materials. *Curr. Opin. Solid State Mater. Sci.* **2011**, *15* (6), 225–235.
- (97) Sun, H.; Luo, Q.; Hou, C.; Liu, J. Nanostructures Based on Protein Self-Assembly: From Hierarchical Construction to Bioinspired Materials. *Nano Today* **2017**, *14*, 16–41.
- (98) Chiu, C.-Y.; Li, Y.; Ruan, L.; Ye, X.; Murray, C. B.; Huang, Y. Platinum Nanocrystals Selectively Shaped Using Facet-Specific Peptide Sequences. *Nature Chem.* **2011**, *3* (5), 393–399.
- (99) Lu, J.; Xue, Y.; Bernardino, K.; Zhang, N.-N.; Gomes, W. R.; Ramesar, N. S.; Liu, S.; Hu, Z.; Sun, T.; de Moura, A. F.; Kotov, N. A.; Liu, K. Enhanced Optical Asymmetry in Supramolecular Chiroplasmonic Assemblies with Long-Range Order. *Science* **2021**, *371* (6536), 1368–1374.
- (100) Merg, A. D.; Zhou, Y.; Smith, A. M.; Millstone, J. E.; Rosi, N. L. Ligand Exchange for Controlling the Surface Chemistry and Properties of Nanoparticle Superstructures. *ChemNanoMat* **2017**, *3* (10), 745–749.
- (101) Tang, Z.; Palafox-Hernandez, J. P.; Law, W.-C.; Hughes, Z. E.; Swihart, M. T.; Prasad, P. N.; Knecht, M. R.; Walsh, T. R. Biomolecular Recognition Principles for

- Bionanocombinatorics: An Integrated Approach To Elucidate Enthalpic and Entropic Factors. *ACS Nano* **2013**, 7 (11), 9632–9646.
- (102) Westcott, S. L.; Oldenburg, S. J.; Lee, T. R.; Halas, N. J. Formation and Adsorption of Clusters of Gold Nanoparticles onto Functionalized Silica Nanoparticle Surfaces. *Langmuir* **1998**, 14 (19), 5396–5401.
- (103) Li, Z.; Jin, R.; Mirkin, C. A.; Letsinger, R. L. Multiple Thiol-Anchor Capped DNA–Gold Nanoparticle Conjugates. *Nucleic Acids Res.* **2002**, 30 (7), 1558–1562.
- (104) Sandström, P.; Boncheva, M.; Åkerman, B. Nonspecific and Thiol-Specific Binding of DNA to Gold Nanoparticles. *Langmuir* **2003**, 19 (18), 7537–7543.
- (105) Helmy, R.; Fadeev, A. Y. Self-Assembled Monolayers Supported on TiO₂: Comparison of C₁₈H₃₇SiX₃ (X = H, Cl, OCH₃), C₁₈H₃₇Si(CH₃)₂Cl, and C₁₈H₃₇PO(OH)₂. *Langmuir* **2002**, 18 (23), 8924–8928.
- (106) Lin, Y.-J.; Chu, L.-K.; Horng, J.-C. Effects of the Terminal Aromatic Residues on Polyproline Conformation: Thermodynamic and Kinetic Studies. *J. Phys. Chem. B* **2015**, 119 (52), 15796–15806.
- (107) Ma, W.; Xu, L.; de Moura, A. F.; Wu, X.; Kuang, H.; Xu, C.; Kotov, N. A. Chiral Inorganic Nanostructures. *Chem. Rev.* **2017**, 117 (12), 8041–8093.
- (108) Yan, W.; Xu, L.; Xu, C.; Ma, W.; Kuang, H.; Wang, L.; Kotov, N. A. Self-Assembly of Chiral Nanoparticle Pyramids with Strong R/S Optical Activity. *J. Am. Chem. Soc.* **2012**, 134 (36), 15114–15121.
- (109) Kuzyk, A.; Schreiber, R.; Fan, Z.; Pardatscher, G.; Roller, E.-M.; Högele, A.; Simmel, F. C.; Govorov, A. O.; Liedl, T. DNA-Based Self-Assembly of Chiral Plasmonic Nanostructures with Tailored Optical Response. *Nature* **2012**, 483 (7389), 311–314.
- (110) Abraham, M. J.; Murtola, T.; Schulz, R.; Páll, S.; Smith, J. C.; Hess, B.; Lindahl, E. GROMACS: High Performance Molecular Simulations through Multi-Level Parallelism from Laptops to Supercomputers. *SoftwareX* **2015**, 1–2, 19–25.
- (111) Nosé, S. A Molecular Dynamics Method for Simulations in the Canonical Ensemble. *Mol. Phys.* **1984**, 52 (2), 255–268.
- (112) Hoover, W. G. Canonical Dynamics: Equilibrium Phase-Space Distributions. *Phys. Rev. A Gen. Phys.* **1985**, 31 (3), 1695–1697.
- (113) MacKerell, A. D.; Bashford, D.; Bellott, M.; Dunbrack, R. L.; Evanseck, J. D.; Field, M. J.; Fischer, S.; Gao, J.; Guo, H.; Ha, S.; Joseph-McCarthy, D.; Kuchnir, L.; Kuczera, K.; Lau, F. T.; Mattos, C.; Michnick, S.; Ngo, T.; Nguyen, D. T.; Prodhom, B.; Reiher, W. E.; Roux, B.; Schlenkrich, M.; Smith, J. C.; Stote, R.; Straub, J.; Watanabe, M.; Wiórkiewicz-

- Kuczera, J.; Yin, D.; Karplus, M. All-Atom Empirical Potential for Molecular Modeling and Dynamics Studies of Proteins. *J. Phys. Chem. B* **1998**, *102* (18), 3586–3616.
- (114) Piana, S.; Lindorff-Larsen, K.; Shaw, D. E. How Robust Are Protein Folding Simulations with Respect to Force Field Parameterization? *Biophys. J.* **2011**, *100* (9), L47–L49.
- (115) Jorgensen, W. L.; Chandrasekhar, J.; Madura, J. D.; Impey, R. W.; Klein, M. L. Comparison of Simple Potential Functions for Simulating Liquid Water. *J. Chem. Phys.* **1983**, *79* (2), 926–935.
- (116) Terakawa, T.; Kameda, T.; Takada, S. On Easy Implementation of a Variant of the Replica Exchange with Solute Tempering in GROMACS. *J. Comput. Chem.* **2011**, *32* (7), 1228–1234.
- (117) Daura, X.; Gademann, K.; Jaun, B.; Seebach, D.; van Gunsteren, W. F.; Mark, A. E. Peptide Folding: When Simulation Meets Experiment. *Angew. Chem., Int. Ed.* **1999**, *38* (1–2), 236–240.
- (118) Jin, R.; Walsh, T. R. Modeling-Led Materials-Binding Peptide Design for Hexagonal Boron Nitride Interfaces. *Adv. Mater. Interfaces* **2022**, *9* (15), 2102397.
- (119) Hub, J. S.; de Groot, B. L.; van der Spoel, D. G_wham—A Free Weighted Histogram Analysis Implementation Including Robust Error and Autocorrelation Estimates. *J. Chem. Theory Comput.* **2010**, *6* (12), 3713–3720.
- (120) Baldwin, R. L.; Rose, G. D. Is Protein Folding Hierarchic? I. Local Structure and Peptide Folding. *Trends Biochem. Sci.* **1999**, *24* (1), 26–33.
- (121) Daggett, V.; Fersht, A. R. Is There a Unifying Mechanism for Protein Folding? *Trends Biochem. Sci.* **2003**, *28* (1), 18–25.
- (122) Zhang, S. Emerging Biological Materials through Molecular Self-Assembly. *Biotechnol. Adv.* **2002**, *20* (5), 321–339.
- (123) Santis, E. D.; G. Ryadnov, M. Peptide Self-Assembly for Nanomaterials: The Old New Kid on the Block. *Chem. Soc. Rev.* **2015**, *44* (22), 8288–8300.
- (124) Stendahl, J. C.; Rao, M. S.; Guler, M. O.; Stupp, S. I. Intermolecular Forces in the Self-Assembly of Peptide Amphiphile Nanofibers. *Adv. Funct. Mater.* **2006**, *16* (4), 499–508.
- (125) Versluis, F.; Robson Marsden, H.; Kros, A. Power Struggles in Peptide-Amphiphile Nanostructures. *Chem. Soc. Rev.* **2010**, *39* (9), 3434–3444.
- (126) Zhao, X.; Pan, F.; Xu, H.; Yaseen, M.; Shan, H.; Hauser, C. A. E.; Zhang, S.; Lu, J. R. Molecular Self-Assembly and Applications of Designer Peptide Amphiphiles. *Chem. Soc. Rev.* **2010**, *39* (9), 3480–3498.

- (127) Branco, M. C.; Sigano, D. M.; Schneider, J. P. Materials from Peptide Assembly: Towards the Treatment of Cancer and Transmittable Disease. *Curr. Opin. Chem. Biol.* **2011**, *15* (3), 427–434.
- (128) Aili, D.; Stevens, M. Bioresponsive Peptide–Inorganic Hybrid Nanomaterials. *Chem. Soc. Rev.* **2010**, *39* (9), 3358–3370.
- (129) Wang, J.; Zhao, X.; Li, J.; Kuang, X.; Fan, Y.; Wei, G.; Su, Z. Electrostatic Assembly of Peptide Nanofiber–Biomimetic Silver Nanowires onto Graphene for Electrochemical Sensors. *ACS Macro Lett.* **2014**, *3* (6), 529–533.
- (130) Li, T.; Lu, X.-M.; Zhang, M.-R.; Hu, K.; Li, Z. Peptide-Based Nanomaterials: Self-Assembly, Properties and Applications. *Bioact. Mater.* **2022**, *11*, 268–282.
- (131) Tan, X.; Xu, Y.; Lin, S.; Dai, G.; Zhang, X.; Xia, F.; Dai, Y. Peptide-Anchored Gold Nanoparticles with Bimetallic Sites for Photo-Switchable Cascade Catalysis. *J. Catal.* **2021**, *402*, 125–129.
- (132) Tjernberg, L.; Hosia, W.; Bark, N.; Thyberg, J.; Johansson, J. Charge Attraction and β Propensity Are Necessary for Amyloid Fibril Formation from Tetrapeptides*. *J. Biol. Chem.* **2002**, *277* (45), 43243–43246.
- (133) Niece, K. L.; Hartgerink, J. D.; Donners, J. J. J. M.; Stupp, S. I. Self-Assembly Combining Two Bioactive Peptide-Amphiphile Molecules into Nanofibers by Electrostatic Attraction. *J. Am. Chem. Soc.* **2003**, *125* (24), 7146–7147.
- (134) Xue, C.; Lin, T. Y.; Chang, D.; Guo, Z. Thioflavin T as an Amyloid Dye: Fibril Quantification, Optimal Concentration and Effect on Aggregation. *R. Soc. Open Sci.* **2017**, *4* (1), 160696.
- (135) Wright, L. B.; Freeman, C. L.; Walsh, T. R. Benzene Adsorption at the Aqueous (0 1 1) α -Quartz Interface: Is Surface Flexibility Important? *Mol. Simul.* **2013**, *39* (13), 1093–1102.
- (136) Hoover, W. G. Canonical Dynamics: Equilibrium Phase-Space Distributions. *Phys. Rev. A* **1985**, *31* (3), 1695–1697.
- (137) Van Gunsteren, W. F.; Berendsen, H. J. C. A Leap-Frog Algorithm for Stochastic Dynamics. *Mol. Simul.* **1988**, *1* (3), 173–185.
- (138) Páll, S.; Hess, B. A Flexible Algorithm for Calculating Pair Interactions on SIMD Architectures. *Comput. Phys. Commun.* **2013**, *184* (12), 2641–2650.
- (139) Darden, T.; York, D.; Pedersen, L. Particle Mesh Ewald: An $N \cdot \log(N)$ Method for Ewald Sums in Large Systems. *J. Chem. Phys.* **1993**, *98* (12), 10089–10092.

- (140) Wright, L. B.; Rodger, P. M.; Corni, S.; Walsh, T. R. GoIP-CHARMM: First-Principles Based Force Fields for the Interaction of Proteins with Au(111) and Au(100). *J. Chem. Theory Comput.* **2013**, *9* (3), 1616–1630.
- (141) Wright, L. B.; Walsh, T. R. Efficient Conformational Sampling of Peptides Adsorbed onto Inorganic Surfaces: Insights from a Quartz Binding Peptide. *Phys. Chem. Chem. Phys.* **2013**, *15* (13), 4715–4726.